Atmospheric and Topographic Correction

(ATCOR Theoretical Background Document)

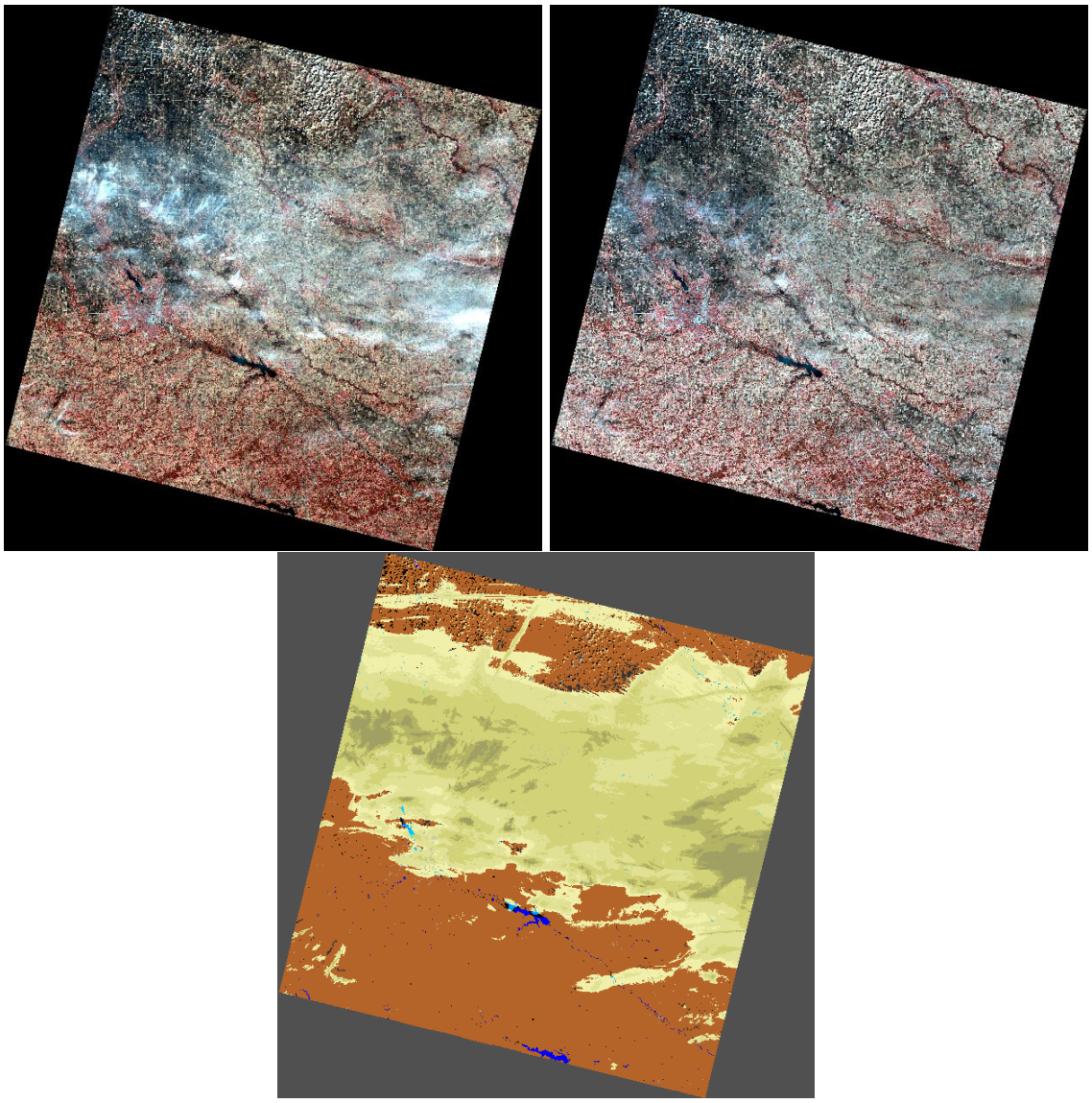

R. Richter[1] and D. Schläpfer[2]
[1] DLR - German Aerospace Center, D - 82234 Wessling, Germany
[2]ReSe Applications LLC , Langeggweg 3, CH-9500 Wil SG, Switzerland
DLR-IB 564-03/2023

The cover page shows a Landsat-8 scene of Iowa (lat 41.8°N, lon. 93.0°W) acquired April 5, 2014. The solar zenith and azimuth angles are 39.7° and 147.4°, respectively. Top left: original scene (RGB = 865, 665, 560 nm), right: surface reflectance product including cirrus correction. The scene is contaminated by cirrus clouds (bottom map) shown in different shades of yellow. Brown indicates clear areas, dark blue is for clear water, light blue for cirrus cloud over water, and black for cloud shadow.

ATCOR Theoretical background, Version 1.3, March 2023

Authors:
R. Richter[1] and D. Schläpfer[2]
[1] DLR - German Aerospace Center, D - 82234 Wessling, Germany
[2] ReSe Applications LLC, Langeggweg 3, CH-9500 Wil SG, Switzerland

Distribution:
ReSe Applications Schläpfer
Langeggweg 3, CH-9500 Wil, Switzerland

Updates: see ReSe download page: www.rese-apps.com/software/download

Contents

List of Figures

List of Tables

Chapter 1

Introduction

This document presents the theoretical background of the satellite and airborne ATCOR models. Unlike the multi-temporal approach of atmospheric compensation [44] it is restricted to the processing of mono-temporal imagery. In addition, the main objective is the atmospheric correction of land scenes, although water bodies are also treated with simplifying assumptions.
Fig.1 shows the main processing steps needed to compensate atmospheric and topographic effects. Input data are the recorded scene plus a meta file containing the acquisition date, time, solar and sensor view geometry etc. Input data is usually in the TIF or JP2 format, a single file, or a separate file for each band. In most cases it represents scaled radiance, named Digital Number (DN), where the radiance L can be obtained with the radiometric offset c_0 and gain c_1:

$$L = c_0 \ + \ c_1 \ DN \tag{1.1}$$

For some instruments the data is delivered as top-of-atmosphere (TOA) reflectance ρ_{TOA}

$$\rho_{TOA} = \frac{\pi \ L \ d^2}{E_s \ cos\theta_s} \tag{1.2}$$

where d is the Earth-Sun distance (astronomical units), E_s the extraterrestrial solar irradiance, and θ_s the solar zenith angle. ATCOR converts TOA reflectance into TOA radiance before starting the atmospheric correction.

Fig. 1.1 presents the main processing steps of atmospheric correction. The input image scene is converted into the ENVI band-sequential format, the necessary parameters are extracted from the image meta file and stored in file *scene.inn*, and the radiometric calibration (c_0, c_1) per band is stored in *scene.cal*.

For a mountainous scene the DEM (Digital Elevtion Model) has to be provided by the user. Dashed lines indicate optional processing steps, e.g. the haze/cirrus removal. For the standard sensors (e.g., Landsat, Sentinel-2, Worldview, etc.) the atmospheric LUTs are already available. For user-defined (hyperspectral) sensors the sensor-specific LUTs have to be calculated with an available tool (see chapter 3.
The main block consists of the preclassification, followed by atmospheric / topographic correction. In certain cases a post-processing is required.

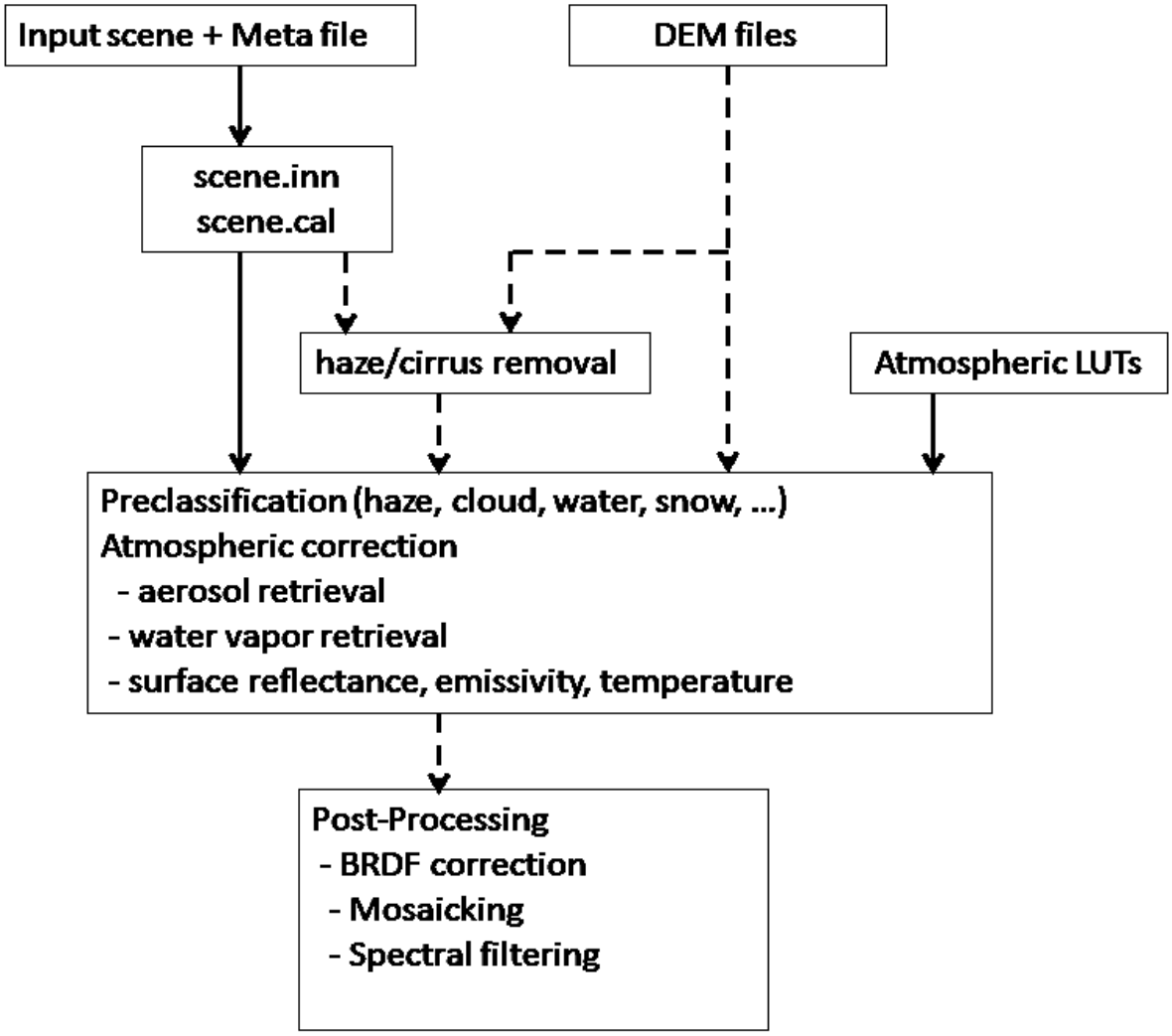

Figure 1.1: *Main steps of atmospheric correction.*

1.1 Basic Concepts in the Solar Region

Standard books on optical remote sensing contain an extensive presentation on sensors, spectral signatures, and atmospheric effects (compare [127, 5, 124]).
This chapter describes the basic concept of atmospheric correction. Only a few simple equations (1.3-1.18) are required to understand the key issues. We start with the radiation components and the relationship between the at-sensor radiance and the digital number or grey level of a pixel. Then we are already able to draw some important conclusions about the radiometric calibration. We continue with some remarks on how to select atmospheric parameters. Next is a short discussion about the thermal spectral region. The remaining sections present the topics of BRDF correction, spectral / radiometric calibration, and de-shadowing. For a discussion of the haze removal method the reader is referred to chapter 12.

Two often used parameters for the description of the atmosphere are 'visibility' and 'optical thick-

ness'.

Visibility and optical thickness

The visibility (horizontal meteorological range) is approximately the maximum horizontal distance a human eye can recognize a dark object against a bright sky. The exact definition is given by the Koschmieder equation:

$$VIS = \frac{1}{\beta}\, ln\frac{1}{0.02} = \frac{3.912}{\beta} \tag{1.3}$$

where β is the extinction coefficient (unit km^{-1}) at 550 nm. The term 0.02 in this equation is an arbitrarily defined contrast threshold. Another often used concept is the optical thickness of the atmosphere (δ) which is the product of the extinction coefficient and the path length x (e.g., from sea level to space in a vertical path) :

$$\delta = \beta\, x \tag{1.4}$$

The optical thickness is a pure number. In most cases, it is evaluated for the wavelength 550 nm. Generally, there is no unique relationship between the (horizontal) visibility and the (vertical) total optical thickness of the atmosphere. However, with the MODTRAN® radiative transfer code a certain relationship has been defined between these two quantities for clear sky conditions as shown in Fig. 1.2 (left) for a path from sea level to space. The optical thickness can be defined separately for the different atmospheric constituents (molecules, aerosols), so there is an optical thickness due to molecular (Rayleigh) and aerosol scattering, and due to molecular absorption (e.g., water water, ozone etc.). The total optical thickness is the sum of the thicknesses of all individual contributors :

$$\delta = \delta(molecular\ scattering)\ +\ \delta(aerosol)\ +\ \delta(molecular\ absorption) \tag{1.5}$$

The MODTRAN® visibility parameter scales the aerosol content in the boundary layer (0 - 2 km altitude). For visibilities greater than 100 km the total optical thickness asymptotically approaches a value of about 0.17 which (at 550 nm) is the sum of the molecular thickness ($\delta = 0.0973$) plus ozone thickness ($\delta = 0.03$) plus a very small amount due to trace gases, plus the contribution of residual aerosols in the higher atmosphere (2 - 100 km) with $\delta = 0.04$. The minimum optical thickness or maximum visibility is reached if the air does not contain aerosol particles (so called "Rayleigh limit") which corresponds to a visibility of 336 km at sea level and no aerosols in the boundary layer and higher atmosphere. In this case the total optical thickness (molecular and ozone) is about $\delta = 0.13$. Since the optical thickness due to molecular scattering (nitrogen and oxygen) only depends on pressure level it can be calculated accurately for a known ground elevation. The ozone contribution to the optical thickness usually is small at 550 nm and a climatologic/geographic average (331 DU) can be taken. Nevertheless, if scene information on ozone is available, it can be specified as an input parameter. This leaves the aerosol contribution as the most important component which varies strongly in space and time. Therefore, the aerosol optical thickness (AOT) at 550 nm is often used to characterize the atmosphere instead of the visibility.
The atmospheric (direct or beam) transmittance for a vertical path through the atmosphere can be calculated as :

$$\tau = e^{-\delta} \tag{1.6}$$

Fig. 1.2 (right) shows an example of the atmospheric transmittance from 0.4 to 2.5 μm. The spectral regions with relatively high transmittance are called "atmospheric window" regions. In

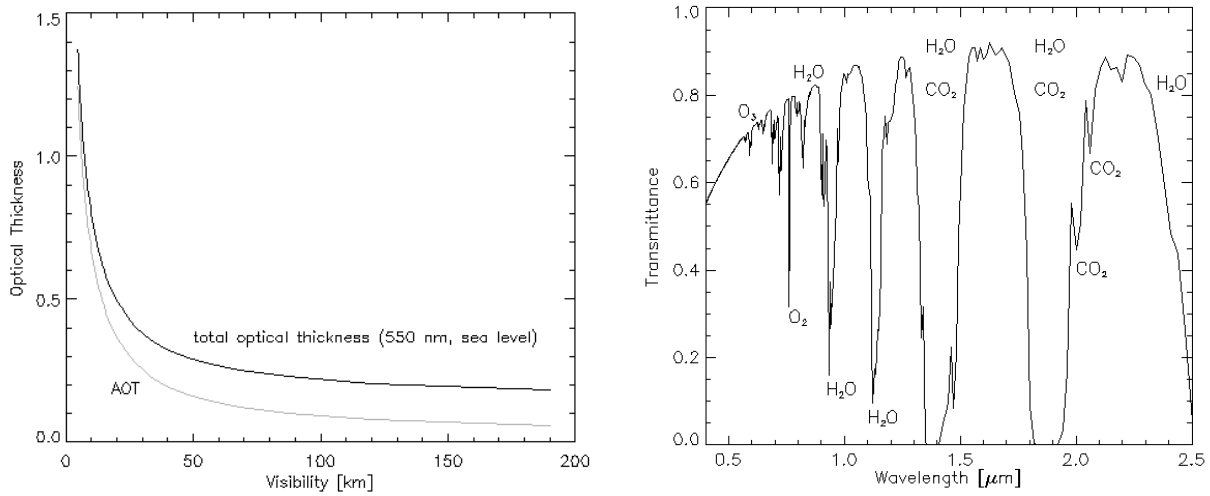

Figure 1.2: *Visibility, AOT, and total optical thickness, atmospheric transmittance.*

absorbing regions the name of the molecule responsible for the attenuation of radiation is included.

Apparent reflectance

The apparent reflectance describes the combined earth/atmosphere behavior with respect to the reflected solar radiation:

$$\rho(apparent) = \frac{\pi \ d^2 \ L}{E \ cos\theta_s} \tag{1.7}$$

where d is the earth-sun distance in astronomical units, $L = c_0 + c1 \ DN$ is the at-sensor radiance, c_0, c_1, DN, are the radiometric calibration offset, gain, and digital number, respectively. E and θ_s are the extraterrestrial solar irradiance and solar zenith angle, respectively. For imagery of satellite sensors the apparent reflectance is also named top-of-atmosphere (TOA) reflectance.

1.1.1 Radiation components

We start with a discussion of the radiation components in the solar region, i.e., the wavelength spectrum from 0.35 - 2.5 μm. Figure 1.3 shows a schematic sketch of the total radiation signal at the sensor. It consists of three components:

1. path radiance (L_1), i.e., photons scattered into the sensor's instantaneous field-of-view, without having ground contact.

2. reflected radiation (L_2) from a certain pixel: the direct and diffuse solar radiation incident on the pixel is reflected from the surface. A certain fraction is transmitted to the sensor. The sum of direct and diffuse flux on the ground is called global flux.

3. reflected radiation from the neighborhood (L_3), scattered by the air volume into the current instantaneous direction, the adjacency radiance. As detailed in [98] the adjacency radiation L_3 consists of two components (atmospheric backscattering and volume scattering) which are combined into one component in Fig. 1.3 to obtain a compact description.

Only radiation component 2 contains information from the currently viewed pixel. The task of atmospheric correction is the calculation and removal of components 1 and 3, and the retrieval of the ground reflectance from component 2.

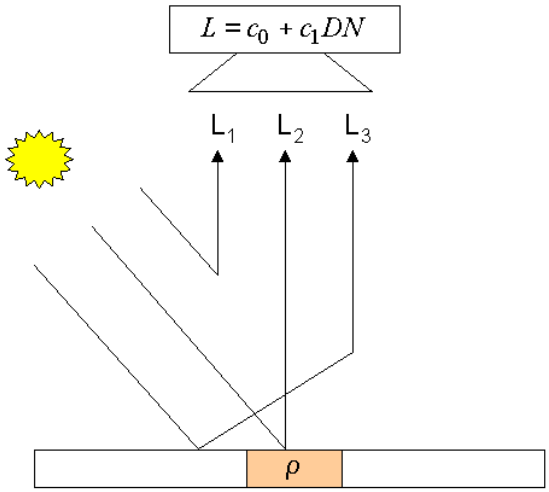

Figure 1.3: *Schematic sketch of solar radiation components in flat terrain.*
L_1 : path radiance, L_2 : reflected radiance, L_3 : adjacency radiation.

So the total radiance signal L can be written as :

$$L = L_{path} + L_{reflected} + L_{adj} (= L_1 + L_2 + L_3) \tag{1.8}$$

The path radiance decreases with wavelength. It is usually very small for wavelengths greater than 800 nm. The adjacency radiation depends on the reflectance or brightness difference between the currently considered pixel and the large-scale (0.5-1 km) neighborhood. The influence of the adjacency effect also decreases with wavelength and is very small for spectral bands beyond 1.5 μm [98].

For each spectral band of a sensor a linear equation describes the relationship between the recorded brightness or digital number DN and the at-sensor radiance (Fig. 1.3) :

$$L = c_0 + c_1 * DN \tag{1.9}$$

The c_0 and c_1 are called radiometric calibration coefficients. The radiance unit in ATCOR is $mW cm^{-2} sr^{-1} \mu m^{-1}$. For instruments with an adjustable gain setting g the corresponding equation is :

$$L = c_0 + \frac{c_1}{g} * DN \tag{1.10}$$

During the following discussion we will always use eq. (1.9). Disregarding the adjacency component we can simplify eq. (1.8)

$$L = L_{path} + L_{reflected} = L_{path} + \tau \rho E_g / \pi = c_0 + c_1 DN \tag{1.11}$$

where τ, ρ, and E_g are the ground-to-sensor atmospheric transmittance, surface reflectance, and global flux on the ground, respectively. Solving for the surface reflectance we obtain :

$$\rho = \frac{\pi \{d^2 (c_0 + c_1 DN) - L_{path}\}}{\tau E_g} \tag{1.12}$$

The factor d^2 takes into account the sun-to-earth distance (d is in astronomical units), because the LUT's for path radiance and global flux are calculated for d=1 in ATCOR. Equation (1.11) is a key formula to atmospheric correction. A number of important conclusions can now be drawn:

- An accurate radiometric calibration is required, i.e., a knowledge of c_0 , c_1 in each spectral band.
- An accurate estimate of the main atmospheric parameters (aerosol type, visibility or optical thickness, and water vapor) is necessary, because these influence the values of path radiance, transmittance, and global flux.
- If the visibility is assumed too low (optical thickness too high) the path radiance becomes high, and this may cause a physically unreasonable negative surface reflectance. Therefore, dark surfaces of low reflectance, and correspondingly low radiance $c_0 + c_1 DN$, are especially sensitive in this respect. They can be used to estimate the visibility or at least a lower bound. If the reflectance of dark areas is known the visibility can actually be calculated (compare chapter 4).
- If the main atmospheric parameters (aerosol type or scattering behavior, visibility or optical thickness, and water vapor column) and the reflectance of two reference surfaces are measured, the quantities L_{path}, τ, ρ, and E_g are known. So, an "inflight calibration" can be performed to determine or update the knowledge of the two unknown calibration coefficients $c_0(k)$, $c_1(k)$ for each spectral band k, see section 1.1.3.

Selection of atmospheric parameters

The optical properties of some air constituents are accurately known, e.g., the molecular or Rayleigh scattering caused by nitrogen and oxygen molecules. Since the mixing ratio of nitrogen and oxygen is constant the contribution can be calculated as soon as the pressure level (or ground elevation) is specified. Other constituents vary slowly in time, e.g., the CO_2 concentration. ATCOR calculations are performed for a CO_2 concentration of 400 ppmv (2015 release). Later releases might update the concentration if necessary. Ozone may also vary in space and time. Since ozone usually has only a small influence, ATCOR employs a fixed value of 331 DU (Dobson units, corresponding to the former unit 0.331 atm-cm, for a ground at sea level) representing average conditions. However, if ozone information is available from other sources and if it deviates more than 10 DU from the reference level (331 DU) then it can be specified as an additional input parameter [103]. The three most important atmospheric parameters that vary in space and time are the aerosol type, the visibility or optical thickness, and the water vapor. We will mainly work with the term *visibility* (or meteorological range), because the radiative transfer calculations were performed with the Modtran®5 code (Berk et al., 1998, 2008), and visibility is an intuitive input parameter in MODTRAN®, although the aerosol optical thickness can be used as well. ATCOR employs a database of LUTs calculated with Modtran®5.

Aerosol type

The aerosol type includes the absorption and scattering properties of the particles, and the wavelength dependence of the optical properties. ATCOR supports four basic aerosol types: rural, urban, maritime, and desert. The aerosol type can be calculated from the image data provided that the scene contains vegetated areas. Alternatively, the user can make a decision, usually based on the geographic location. As an example, in areas close to the sea the maritime aerosol would be a logical choice if the wind was coming from the sea. If the wind direction was toward the sea and

the air mass is of continental origin the rural, urban, or desert aerosol would make sense, depending on the geographical location. If in doubt, the rural (continental) aerosol is generally a good choice. The aerosol type also determines the wavelength behavior of the path radiance. Of course, nature can produce any transitions or mixtures of these basic four types. However, ATCOR is able to adapt the wavelength course of the path radiance to the current situation provided spectral bands exist in the blue-to-red region and the scene contains reference areas of known reflectance behavior (compare chapter 4 for details).

Visibility estimation
Two options for aerosol amount retrieval are available in ATCOR:

- An interactive estimation in the SPECTRA module (compare ATCOR user manual). The spectra of different targets in the scene can be displayed as a function of visibility. A comparison with reference spectra from libraries determines the visibility. In addition, dark targets like vegetation in the blue-to-red spectrum or water in the red-to-NIR can be used to estimate the visibility.
- An automatic calculation of the visibility can be performed if the scene contains dark reference pixels or shadow pixels (see chapter 4 for details).

Water vapor column
The water vapor content can be automatically computed if the sensor has spectral bands in water vapor regions (e.g., 920-960 nm). The approach is based on the differential absorption method and employs bands in absorption regions and window regions to measure the absorption depth, see chapter 5. Otherwise, if a sensor does not possess spectral bands in water vapor regions, e.g. Landsat TM or SPOT, an estimate of the water vapor column based on the season (summer / winter) is usually sufficient. Typical ranges of water vapor columns are (sea-level-to space):

tropical conditions:	wv=3-5 cm (or g cm^{-2})
midlatitude summer:	wv= 2-3 cm
dry summer, spring, fall:	wv=1-1.5 cm
dry desert or winter:	wv=0.3-0.8 cm

1.1.2 Spectral calibration

This section can be skipped if data processing is only performed for imagery of broad-band sensors. Sensor calibration problems may pertain to spectral properties, i.e., the channel center positions and / or bandwidths might have changed compared to laboratory measurements, or the radiometric properties, i.e., the offset (c_o) and slope (c_1) coefficients, relating the digital number (DN) to the at-sensor radiance $L = c_0 + c_1 * DN$. Any spectral mis-calibration can usually only be detected from narrow-band hyperspectral imagery as discussed in this section. For multispectral imagery, spectral calibration problems are difficult or impossible to detect, and an update is generally only performed with respect to the radiometric calibration coefficients, see section 1.1.3.

Surface reflectance spectra retrieved from narrow-band hyperspectral imagery often contain spikes and dips in spectral absorption regions of atmospheric gases (e.g., oxygen absorption around 760 nm, water vapor absorption around 940 nm). These effects are most likely caused by a spectral mis-calibration. In this case, an appropiate shift of the center wavelengths of the channels will

remove the spikes. This is performed by an optimization procedure that minimizes the deviation between the surface reflectance spectrum and the corresponding smoothed spectrum. The merit function to be minimized is

$$\chi^2(\delta) = \sum_{i=1}^{n} \{\rho_i^{surf}(\delta) - \rho_i^{smooth}\}^2 \tag{1.13}$$

where $\rho_i^{surf}(\delta)$ is the surface reflectance in channel i calculated for a spectral shift δ, ρ_i^{smooth} is the smoothed (low pass filtered) reflectance, and n is the number of bands in each spectrometer of a hyperspectral instrument. So the spectral shift is calculated independently for each spectrometer. In the currently implemented version, the channel bandwidth is not changed and the laboratory values are assumed valid. More details of the method are described in [42]. A spectral re-calibration should precede any re-calibration of the radiometric calibration coefficients; see section 6.4.1 and 14.1 for details about this process.

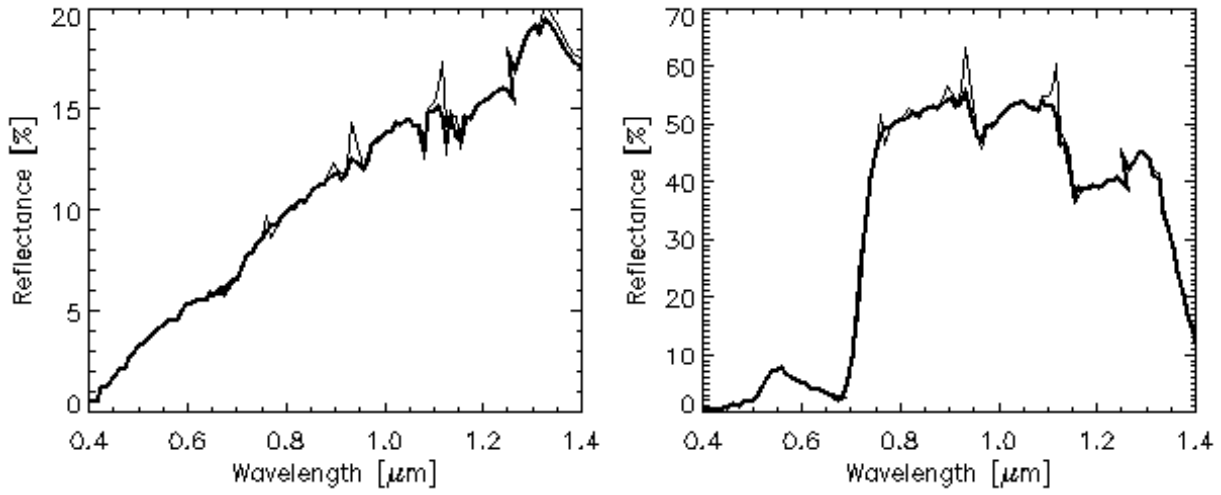

Figure 1.4: *Wavelength shifts for an AVIRIS scene.*

Figure 1.4 shows a comparison of the results of the spectral re-calibration for a soil and a vegetation target retrieved from an AVIRIS scene (16 Sept. 2000, Los Angeles area). The flight altitude was 20 km above sea level (asl), heading west, ground elevation 0.1 km asl, the solar zenith and azimuth angles were 41.2°and 135.8°. Only part of the spectrum is shown for a better visual comparison of the results based on the original spectral calibration (thin line) and the new calibration (thick line). The spectral shift values calculated for the 4 individual spectrometers of AVIRIS are 0.1, -1.11, -0.88, and -0.21 nm, respectively.

1.1.3 Inflight radiometric calibration

Inflight radiometric calibration experiments are performed to check the validity of the laboratory calibration. For spaceborne instruments processes like aging of optical components or outgassing during the initial few weeks or months after launch often necessitate an updated calibration. This approach is also employed for airborne sensors because the aircraft environment is different from the laboratory and this may have an impact on the sensor performance. The following presentation only discusses the radiometric calibration and assumes that the spectral calibration does not

change, i.e., the center wavelength and spectral response curve of each channel are valid as obtained in the laboratory, or it was already updated as discussed in chapter 1.1.2. Please refer to chapter 14 and the description in the ATCOR user manual for further detail about how to perform an inflight calibration.

The radiometric calibration uses measured atmospheric parameters (visibility or optical thickness from sun photometer, water vapor content from sun photometer or radiosonde) and ground reflectance measurements to calculate the calibration coefficients c_0 , c_1 of equation (1.9) for each band. For details, the interested reader is referred to the literature ([129, 111, 91]). Depending of the number of ground targets we distinguish three cases: a single target, two targets, and more than two targets.

Calibration with a single target
In the simplest case, when the offset is zero ($c_0 = 0$), a single target is sufficient to determine the calibration coefficient c_1:

$$L_1 = c_1 DN_1^* = L_{path} + \tau\rho_1 E_g/\pi \tag{1.14}$$

L_{path} , τ, and E_g are taken from the appropriate LUT's of the atmospheric database, ρ_1 is the measured ground reflectance of target 1, and the channel or band index is omitted for brevity. DN_1^* is the digital number of the target, averaged over the target area and already corrected for the adjacency effect. Solving for c_1 yields:

$$c_1 = \frac{L_1}{DN_1^*} = \frac{L_{path} + \tau\rho_1 E_g/\pi}{DN_1^*} \tag{1.15}$$

Remark: a bright target should be used here, because for a dark target any error in the ground reflectance data will have a large impact on the accuracy of c_1.

Calibration with two targets

In case of two targets a bright and a dark one should be selected to get a reliable calibration. Using the indices 1 and 2 for the two targets we have to solve the equations:

$$L_1 = c_0 + c_1 * DN_1^* \qquad\qquad L_2 = c_0 + c_1 * DN_2^* \tag{1.16}$$

This can be performed with the $c_0\&c_1$ *option* of ATCOR's calibration module. The result is:

$$c_1 = \frac{L_1 - L_2}{DN_1^* - DN_2^*} \tag{1.17}$$

$$c_0 = L_1 - c_1 * DN_1^* \tag{1.18}$$

Equation (1.17) shows that DN_1^* must be different from DN_2^* to get a valid solution, i.e., the two targets must have different surface reflectances in each band. If the denominator of eq. (1.17) is zero ATCOR will put in a 1 and continue. In that case the calibration is not valid for this band. The requirement of a dark and a bright target in all channels cannot always be met.

Calibration with $n > 2$ targets

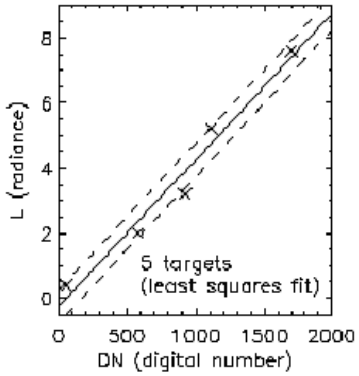

Figure 1.5: *Radiometric calibration with multiple targets using linear regression.*

In cases where n > 2 targets are available the calibration coefficients can be calculated with a least squares fit applied to a linear regression equation, see figure 1.5. This is done by the "cal_regress" program of ATCOR. It employs the "*.rdn" files obtained during the single-target calibration (the "c1 option" of ATCOR's calibration module.
Note: If several calibration targets are employed, care should be taken to select targets without spectral intersections, since calibration values at intersection bands are not reliable. If intersections of spectra cannot be avoided, a larger number of spectra should be used, if possible, to increase the reliability of the calibration.

1.1.4 De-shadowing

Remotely sensed optical imagery of the Earth's surface is often contaminated with cloud and cloud shadow areas. Surface information under cloud covered regions cannot be retrieved with optical sensors, because the signal contains no radiation component being reflected from the ground. In shadow areas, however, the ground-reflected solar radiance is always a small non-zero signal, because the total radiation signal at the sensor contains a direct (beam) and a diffuse (reflected skylight) component. Even if the direct solar beam is completely blocked in shadow regions, the reflected diffuse flux will remain, see Fig. 1.6. Therefore, an estimate of the fraction of direct solar irradiance for a fully or partially shadowed pixel can be the basis of a compensation process called de-shadowing or shadow removal. The method can be applied to shadow areas cast by clouds or buildings.

Figure 1.7 shows an example of removing building shadows. The scene covers part of the central area of Munich. It was recorded by the Ikonos-2 sensor (17 Sept. 2003). The solar zenith and azimuth angles are 46.3°and 167.3°, respectively. After shadow removal the scene displays a much lower contrast, of course, but many details can be seen that are hidden in the uncorrected scene, see the zoom images of figure 1.8. The central zoom image represents the shadow map, scaled between 0 and 1000. The darker the area the lower the fractional direct solar illumination, i.e. the higher the amount of shadow. Some artifacts can also be observed in Figure 1.7, e.g., the Isar river at the bottom right escaped the water mask, entered the shadow mask, and is therefore overcorrected.

The proposed de-shadowing technique works for multispectral and hyperspectral imagery over land acquired by satellite / airborne sensors. The method requires a channel in the visible and at least

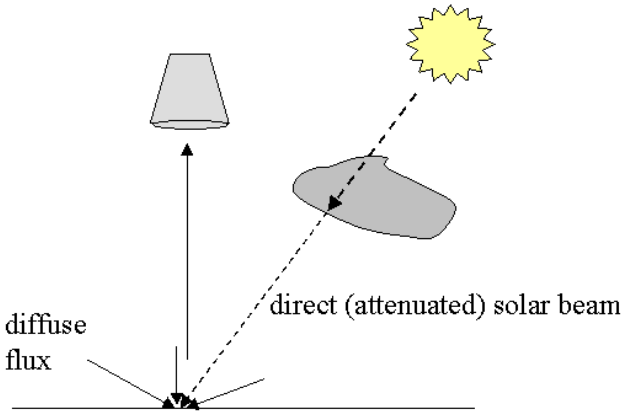

Figure 1.6: *Sketch of a cloud shadow geometry.*

one spectral band in the near-infrared (0.8-1 μm) region, but performs much better if bands in the short-wave infrared region (around 1.6 and 2.2 μm) are available as well. A fully automatic shadow removal algorithm has been implemented. However, the method involves some scene-dependent thresholds that might be optimized during an interactive session. In addition, if shadow areas are concentrated in a certain part of the scene, say in the lower right quarter, the performance of the algorithm improves by working on the subset only.

The de-shadowing method employs masks for cloud and water. These areas are identified with spectral criteria and thresholds. Default values are included in a file in the ATCOR path, called "preferences/preference_parameters.dat". As an example, it includes a threshold for the reflectance of water in the NIR region, ρ=5% . So, a reduction of this threshold will reduce the number of pixels in the water mask. A difficult problem is the distinction of water and shadow areas. If water bodies are erroneously included in the shadow mask, the resulting surface reflectance values will be too high.

Details about the processing can be found in chapter 13.

1.1.5 BRDF correction

The reflectance of many surface covers depends on the viewing and solar illumination geometry. This behavior is described by the bidirectional reflectance distribution function (BRDF). It can clearly be observed in scenes where the view and / or sun angles vary over a large angular range.

Since most sensors of the satellite version of ATCOR have a small field-of-view, these effects play a role in rugged terrain, for the wide FOV sensors such as IRS-1D WiFS or MERIS, and if mosaics of images registered with variable observation angles are to be produced.

For flat terrain scenes across-track brightness gradients that appear after atmospheric correction are caused by BRDF effects, because the sensor's view angle varies over a large range. In extreme cases when scanning in the solar principal plane, the brightness is particularly high in the hot spot angular region where retroreflection occurs, see Figure 1.9, left image, left part. The opposite scan

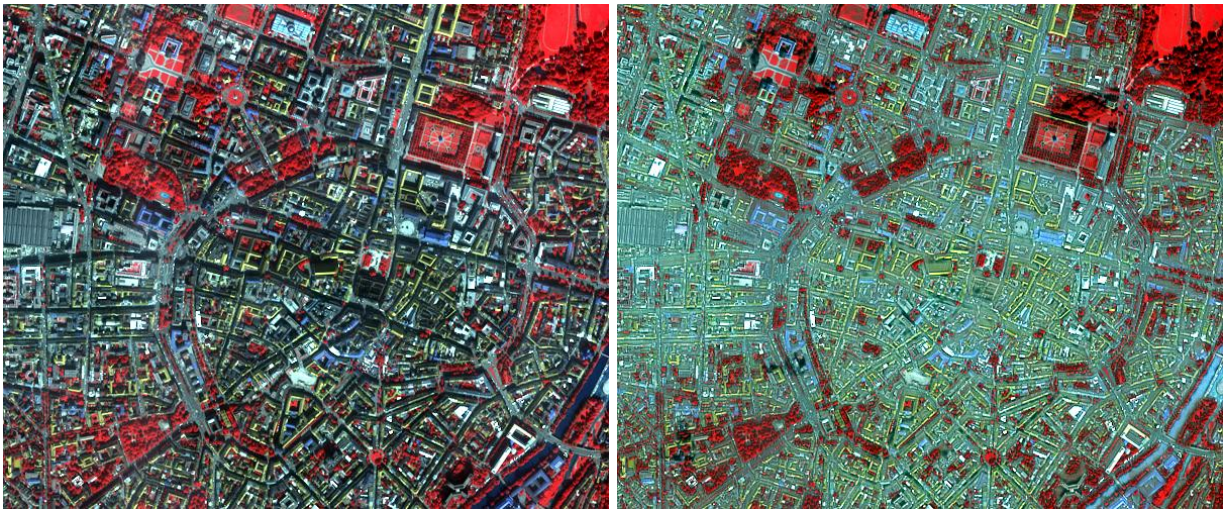

Figure 1.7: *De-shadowing of an Ikonos image of Munich.*
©European Space Imaging GmbH 2003. Color coding: RGB = bands 4/3/2 (800/660/550 nm).
Left: original, right: de-shadowed image.

angles (with respect to the central nadir region) show lower brightness values.

A simple method, called nadir normalization or across-track illumination correction, calculates the brightness as a function of scan angle, and multiplies each pixel with the reciprocal function (compare Section 8.1).
The BRDF effect can be especially strong in rugged terrain with slopes facing the sun and others oriented away from the sun. In areas with steep slopes the local solar zenith angle β may vary from 0° to 90°, representing geometries with maximum solar irradiance to zero direct irradiance, i.e., shadow. The angle β is the angle between the surface normal of a DEM pixel and the solar zenith angle of the scene. In mountainous terrain there is no simple method to eliminate BRDF effects. The usual assumption of an isotropic (Lambertian) reflectance behavior often causes an overcorrection of faintly illuminated areas where local solar zenith angles β range from 60°- 90°. These areas appear very bright, see Figure 1.10, left part.

To avoid a misclassification of these bright areas the reflectance values have to be reduced (Fig. 1.10, center part). In ATCOR empirical geometry-dependent functions are used for this purpose. In the simplest cases, the empirical BRDF correction employs only the local solar zenith angle β and a threshold β_T to reduce the overcorrected surface reflectance ρ_L with a factor, depending on the incidence angle. For details the interested reader is referred to Chapter 7.

The third method available in ATCOR is the BRDF effects correction (BREFCOR) method, which uses both the scene illumination and per-pixel observation angle. It may also be used if a number of satellite scenes are to be mosaicked. It follows a novel scheme based on a fuzzy surface classification and uses BRDF models for the correction. The process follows the below steps:

1. perform a fuzzy BRDF-Class-Index (BCI) image classification
2. calibrate the BRDF-model using a number of scenes, e.g. meant for mosaicing

Figure 1.8: *Zoomed view of central part of Figure 1.7.*
Courtesy of European Space Imaging, Color coding: RGB = bands 4/3/2.
Left: original, center: shadow map, right: de-shadowed image.

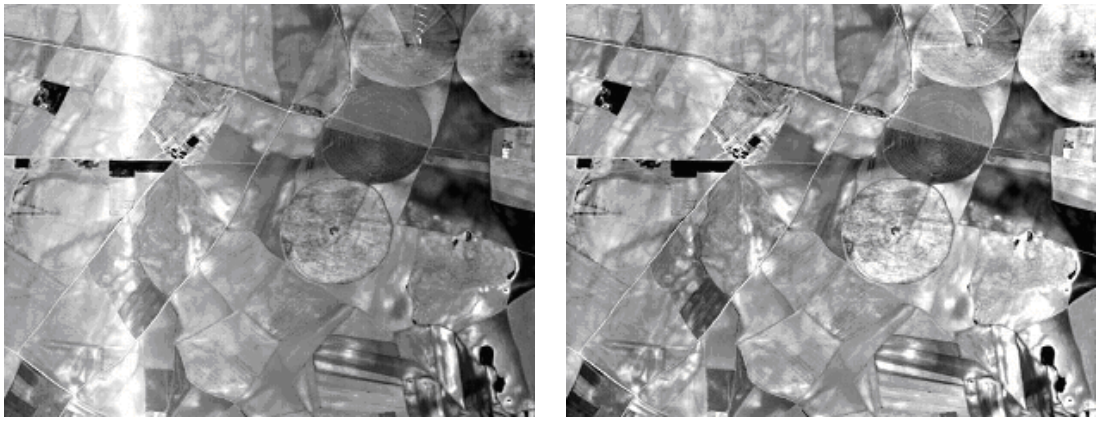

Figure 1.9: *Nadir normalization of an image with hot-spot geometry. Left: reflectance image without BRDF correction. Right: after empirical BRDF correction.*

3. calculate the anisotropy index for each spectral band using the calibrated model and the BCI
4. correct the image using the anisotropy index

Further details about this methods can be found in section 8.2.

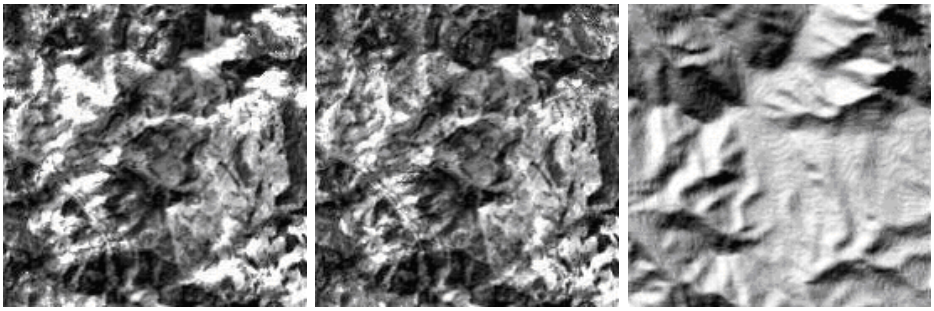

Figure 1.10: *BRDF correction in rugged terrain imagery. Left: image without BRDF correction. Center: after incidence BRDF correction with threshold angle $\beta_T = 65°$. Right: illumination map = $cos\beta$.*

Figure 1.11: *Effect of BRDF correction on mosaic (RapidEye image, ©DLR)*

1.2 Basic Concepts in the Thermal Region

Fig. 1.12 (left) presents an overview of the atmospheric transmittance in the 2.5 - 14 μm region. The main absorbers are water vapor and CO_2 which totally absorb in some parts of the spectrum. In the thermal region (8 - 14 μm) the atmospheric transmittance is mainly influenced by the water vapor column, ozone (around 9.6 μm) and CO_2 (at 14 μm). Fig. 1.12 (right) shows the transmittance for three levels of water vapor columns w=0.4, 1.0, 2.9 cm, representing dry, medium, and humid conditions. The aerosol influence still exists, but is strongly reduced compared to the solar spectral region because of the much longer wavelength. So an accurate estimate of the water vapor column is required in this part of the spectrum to be able to retrieve the surface properties, i.e., spectral emissivity and surface temperature.
Similar to the solar region, there are three radiation components: thermal path radiance (L_1), i.e., photons emitted by the atmospheric layers, emitted surface radiance (L_2), and reflected radiance (L_3).
In the thermal spectral region from 8 - 14 μm the radiance signal can be written as

$$L = L_{path} + \tau\epsilon L_{BB}(T) + \tau(1-\epsilon)F/\pi \tag{1.19}$$

where L_{path} is the thermal path radiance, i.e., emitted and scattered radiance of different layers of the air volume between ground and sensor, τ is the atmospheric ground-to-sensor transmittance, ϵ is the surface emissivity ranging between 0 and 1, $L_{BB}(T)$ is Planck's blackbody radiance of a surface at temperature T, and F is the thermal downwelling flux of the atmosphere, see Fig. 1.13. So the total signal consists of path radiance, emitted surface radiance, and reflected atmospheric

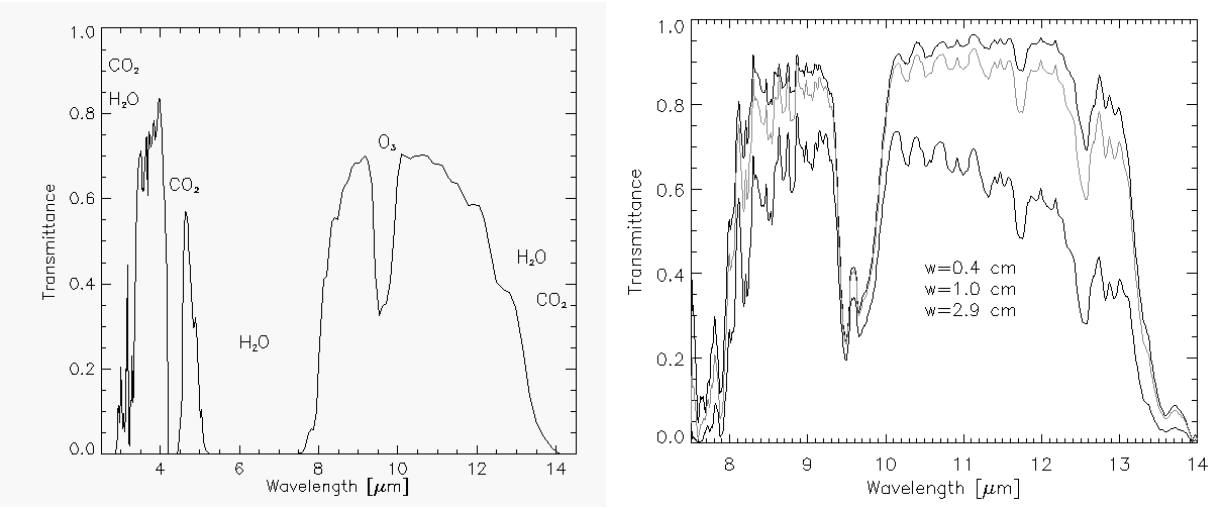

Figure 1.12: *Atmospheric transmittance in the thermal region.*

radiation. The adjacency radiation, i.e., scattered radiation from the neighborhood of a pixel, can be neglected because the scattering efficiency decreases strongly with wavelength.

For most natural surfaces the emissivity in the 8-12 μm spectral region ranges between 0.95 and 0.99. Therefore, the reflected downwelling atmospheric flux contributes only a small fraction to the signal. Neglecting this component for the simplified discussion of this chapter we can write

$$L_{BB}(T) = \frac{L - L_{path}}{\tau\epsilon} = \frac{c_0 + c_1 DN - L_{path}}{\tau\epsilon} \tag{1.20}$$

In the thermal region the aerosol type plays a negligible role because of the long wavelength, and atmospheric water vapor is the dominating parameter. So the water vapor, and to a smaller degree the visibility, determine the values of L_{path} and τ. In case of coregistered bands in the solar and thermal spectrum the water vapor and visibility calculation may be performed with the solar channels. In addition, if the surface emissivity is known, the temperature T can be computed from eq. (1.20) using Planck's law.

For simplicity a constant emissivity $\epsilon = 1.0$ or $\epsilon = 0.98$ is often used and the corresponding temperature is called brightness temperature. The kinetic surface temperature differs from the brightness temperature if the surface emissivity does not match the assumed emissivity. With the assumption $\epsilon = 1.0$ the kinetic temperature is always higher than the brightness temperature. As a rule of thumb an emissivity error of 0.01 (one per cent) yields a surface temperature error of 0.5K.

For rugged terrain imagery no slope/aspect correction is performed for thermal bands, only the elevation-dependence of the atmospheric parameters is taken into account.

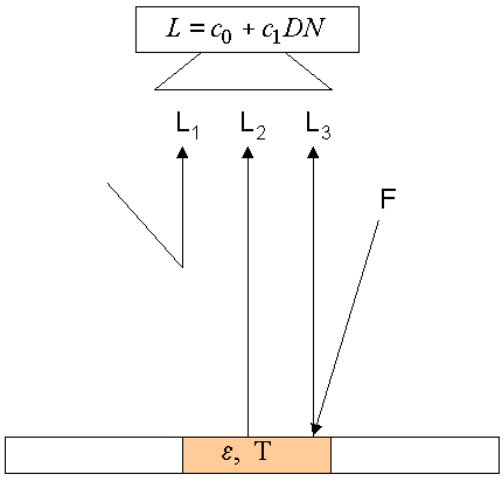

Figure 1.13: *Radiation components in the thermal region.*
$L_1 = L_P$, $L_2 = \tau\ \epsilon\ L_{BB}(T)$, $L_3 = \tau\ (1-\epsilon)\ F/\pi$.

Chapter 2

Preclassification

The preclassification employs spectral channels in the visible/near infrared (VNIR) and short-wave infrared (SWIR) together with empirical thresholds on the top-of-atmosphere (TOA) reflectance to assign a certain label ('class') to each pixel. It is an important first step, because subsequent modules (e.g. aerosol and water vapor retrieval) use this information. The approach is similar to the ACCA ([52] and Fmask [148] strategies for Landsat images, but a compromise was made with respect to execution time and complexity. In addition, the classification rules had to be modified for sensors with less spectral bands than Landsat, e.g. only VNIR bands. Basic classes are:

- land
- water
- snow/ice
- cloud (non-cirrus)
- cirrus cloud (also see chapter 11)
- haze (see chapter 12 for a detailed description)
- shadow and topographic shadow. Shadow is calculated with spectral and geometric criteria, topographic shadow is derived from the DEM and the solar geometry.

Since water and shadow are often difficult to distinguish with spectral thresholds, ATCOR uses an iterative approach to achieve improved results, see Figure 2.1. The steps 3 and 4 need a water vapor map, so these steps cannot be conducted for Landsat-8 data, only for Sentinel-2 data. These steps are very efficient to reduce cloud commission errors due to bright surfaces (e.g. desert sand, buildings), because clouds have a much lower water vapor column than the clear part of the scene.

This feature is not included in the Fmask algorithm of 2015 (reference [148]) for Sentinel-2 (S2) images. However, the improved Fmask reduces the cloud commission errors by exploiting the S2 parallax effects (reference [31]). Our approach does not use parallax effects, and is generally applicable for sensors with water vapor bands.

2.1 Spectral masking criteria

Several masking functions are available, depending on whether a complete set of classes is necessary or only a subset of classes. In this document the symbol ρ^* represents TOA (or at-sensor)

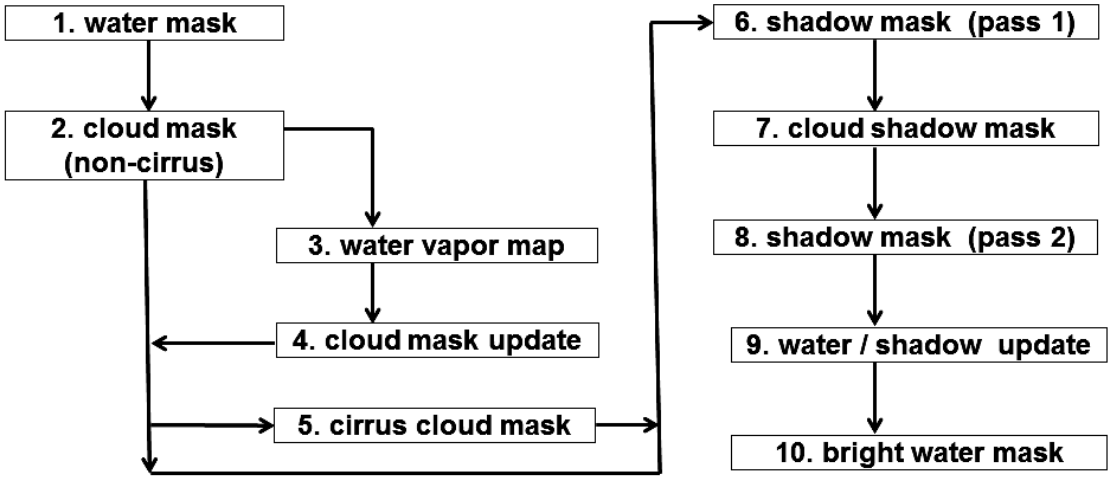

Figure 2.1: *Flow chart of iterated masking.*

reflectance.

The band assignments, like red band, also apply to hyperspectral sensors, with the definitions: red: center wavelength closest to 0.660 μm; green: closest to 0.550 μm; NIR: closest to 0.850 μm; SWIR1: closest to 1.650 μm; and SWIR2: closest to 2.200 μm.

The following masks use empirical thresholds similar to the ones proposed for Landsat-7 [52]. No spectral masking is performed for panchromatic imagery.

The TOA reflectance of band 'k' is calculated as:

$$\rho_k^* = \frac{\pi \; d^2 \; L_k}{E_k \; cos\theta_s} \tag{2.1}$$

where d is the earth-sun distance in Astronomical Units, E_k is the extraterrestrial solar irradiance for band 'k', L_k the measured radiance, and θ_s is the solar zenith angle at the acquisition time.

2.1.1 Water mask

If only VNIR bands are available, then water pixels are masked with the criterion:

$$water \;:\; \rho_{red}^* < 0.20 \;\wedge\; \rho_{green}^* > \rho_{red}^* \;\wedge\; \rho_{NIR}^* < \rho_{red}^* + 0.02 \;\wedge\; NDVI < 0.10 \tag{2.2}$$

NDVI is the normalized vegetation index:

$$NDVI = \frac{\rho_{NIR}^* - \rho_{red}^*}{\rho_{NIR}^* + \rho_{red}^*} \tag{2.3}$$

If the SWIR1 band ($1.6 \mu m$, index SW1) is available, then the first step defines water pixels as:

$$water \;:\; \rho_{red}^* < 0.20 \;\wedge\; \rho_{NIR}^* < \rho_{red}^* + 0.02 \;\wedge\; \rho_{SW1}^* < 0.03 \;\wedge\; NDVI < 0.10 \tag{2.4}$$

If a DEM file is available, then pixels with slope $> 3°$ are excluded from the water map.

2.1.2 Water cloud mask

Define band $blu = min(0.42,\ 0.44,\ 0.49\ \mu m)$, i.e. this is band 1 for Landsat-8 and Sentinel-2. Then non-cirrus or water cloud is defined by the following spectral reflectance thresholds:

$$\begin{aligned} cloud\ :\ \rho^*_{blu} > 0.25\ \wedge\ \rho^*_{red} > 0.15\ \wedge\ \rho^*_{NIR}/\rho^*_{red} < 2\ \wedge\ \rho^*_{NIR} < 1.7\rho^*_{blu} \\ \wedge\ \rho^*_{NIR} > 0.8\rho^*_{red}\ \wedge\ \rho^*_{red} < 1.4\rho^*_{blu}\ \wedge\ NDSI < 0.7\ \vee\ DN(blu) saturated \end{aligned} \tag{2.5}$$

If a blue band is not available, then the green band is employed. If the SWIR1 band (1.6 μm) is not available, then the NDSI criterion cannot be applied.

If a thermal band exists (e.g. the Landsat instruments), the next criterion is applied in addition to the previous spectral thresholds [52] :

$$cloud\ :\ (1 - \rho^*_{SW1})\ T_{bb} < 225\ K \tag{2.6}$$

This threshold works well because water clouds typically have high reflectance values in the 1.6 μm channel ($\rho^*_{SW1} = 0.4 - 0.8$) and brightness temperatures of $T_{bb} = 270 - 295$ K. However, if $T_{bb} > 300$ K then this pixel is removed from the cloud mask.

2.1.3 Cloud and water vapor

If a water vapor map $W(x, y)$ exists (steps 3, 4 of Fig. 2.1) then the cloud mask can be improved. The water vapor map W is calculated separately using the APDA algorithm [115]. Then the scene-average value $\bar{W}(clear)$ for the clear part of the scene (i.e. without clouds, without water) is computed. If $W(x, y) > 0.8\ \bar{W}(clear)$ for a cloud pixel, then this pixel is removed from the cloud class, because cloudy pixels have a low water vapor column. In case of a rugged terrain with a DEM, this criterion is only applied if the standard deviation of the elevation is less than 300 m, because large elevation differences cause large variations in the water vapor column.
This step reduces false cloud classifications caused by bright buildings, sand etc.

2.1.4 Cirrus mask

Cirrus pixels are masked with the TOA reflectance of the narrow 1.38μm band. There are 3 cirrus classes (thin, medium, thick) separately for land and water, and two additional classes (cirrus cloud, thick cirrus cloud) according to the following set of relationships:

$$0.01 < \rho^*(1.38\mu m) < 0.015 \qquad thin \tag{2.7}$$

$$0.015 \leq \rho^*(1.38\mu m) < 0.025 \qquad medium \tag{2.8}$$

$$0.025 \leq \rho^*(1.38\mu m) < 0.040 \qquad thick \tag{2.9}$$

$$0.040 \leq \rho^*(1.38\mu m) < 0.050 \qquad cirrus\ cloud \tag{2.10}$$

$$\rho^*(1.38\mu m) \geq 0.050 \qquad thick\ cirrus\ cloud \tag{2.11}$$

These cirrus classes are only used in the visual display of the masking (file *'*_out_hcw.bsq'*), otherwise cirrus is in not treated in discrete steps. The cirrus assignment will fail for very low water vapor conditions and bright surfaces, e.g. desert and high mountain regions, because then the 1.38μm channel becomes partially transparent. However, the elevation influence is approximately taken into account, see chapter 11.2 and reference [123].
The dehaze / decirrus algorithms are usually successful for the cirrus optical thickness $t_{cir} < 0.04$, the performance is degraded for $t_{cir} > 0.04$.

2.1.5 Haze

The haze removal algorithm of reference [72] is used to obtain a haze mask, also the combined haze/cirrus removal of reference [73]. See chapter 12 for details. The former HOT (Haze Optimized Transform) method (chapter 12.1) is not recommended, but kept for backward compatibility.

2.1.6 Snow/ice mask

If no $2.2\mu m$ band and no thermal band exists, but a $1.6\mu m$ band, then snow/ice pixels are masked with:

$$snow \ : \ NDSI > 0.40 \ \wedge \ \rho^*_{green} \geq 0.22 \tag{2.12}$$

If no green band is available, then the red band is used. If no SWIR1 band is available, then snow masking is not applied. If a $2.2\mu m$ band exists (index 'SW2') then the criteria 2.13 are applied:

$$\begin{aligned} snow \ : \ & (\ NDSI > 0.40 \ \wedge \ \rho^*_{green} \geq 0.22 \ ) \vee \\ & (NDSI > 0.25 \ \wedge \ \rho^*_{green} \geq 0.22 \ \wedge \rho^*_{SW2}/\rho^*_{green} < 0.5) \end{aligned} \tag{2.13}$$

If a thermal band exists, then the TOA blackbody temperature T_{bb} threshold 8° Celsius is additionally used for the snow mask. If no $2.2\mu m$ band exists we employ:

$$snow \ : \ NDSI > 0.40 \ \wedge \ \rho^*_{green} \geq 0.22 \ \wedge \ T_{bb} < 8 \tag{2.14}$$

If a SWIR2 band exists the counterpart of the criteria 2.13 is:

$$\begin{aligned} snow \ : \ & (\ NDSI > 0.40 \ \wedge \ \rho^*_{green} \geq 0.22 \ \wedge \ T_{bb} < 3.8) \vee \\ & (NDSI > 0.25 \ \wedge \ \rho^*_{green} \geq 0.22 \ \wedge \ \rho^*_{SW2}/\rho^*_{green} < 0.5 \ \wedge \ T_{bb} < 8) \end{aligned} \tag{2.15}$$

The relatively high temperature thresholds (3.8 and 8° Celsius) are justified because of the high NDSI thresholds. In addition, they allow some margins for the calibration accuracy and for cases of partial snow covering (mixed pixels).

2.2 Shadow mask (pass 1)

We define a reference shadow mask, where potential shadow pixels are marked, independent of their origin. So the origin can be caused by buildings, trees, or clouds. We define a generous shadow mask in pass 1, because the cloud mask will be shifted locally to check if it covers parts of the shadow mask. The shadow mask of pass 1 may also include water pixels. The shadow reference map uses the statistics (mean and standard deviation) of the red and NIR band TOA reflectance ($\bar{\rho}(TOA, red)$, σ_{red} and $\bar{\rho}(TOA, NIR)$, σ_{NIR}), and defines red and NIR band thresholds. The statistics excludes cloud (cirrus and non-cirrus), and snow/ice. We define the red and NIR band thresholds:

$$t_{red} = \bar{\rho}(TOA, red) + 0.1 \ \sigma_{red} \tag{2.16}$$

$$t_{NIR} = \bar{\rho}(TOA, NIR) - \ \sigma_{NIR} \tag{2.17}$$

We distinguish two cases of shadow scenes, typically representative of vegetated and arid scenes, respectively:

- If $\bar{\rho}^*_{red} \leq 0.15$ then

$$shadow: \ \rho^*_{red} < t_{red} \ \wedge \ \rho^*_{NIR} < t_{NIR} \ \wedge \ not\ cloud \tag{2.18}$$

  else

- If $t_{NIR} < t_{red}$ then $t_{NIR} = t_{red}$

$$shadow: \ \rho^*_{red} < t_{red} \ \wedge \ \rho^*_{NIR} < t_{NIR} \ \wedge \ not\ cloud \tag{2.19}$$

2.3 Cloud shadow mask

The geometric cloud shadow mask relies on the reference shadow mask of pass 1, where potential shadow pixels are marked, independent of their origin. So the origin can be caused by buildings, trees, or clouds. The existing cloud mask (or a part of it) is shifted according to the solar azimuth angle, and the shift vector depends on the solar zenith and azimuth angles and the cloud height.

Since the cloud height is not known, the method iterates the height from 300 m above ground to 6 km, in steps of 100 m for the non-cirrus cloud. The height interval up to 6 km is sufficient for non-cirrus clouds, and for cirrus clouds the interval is 6 - 20 km, again with an increment of 100 m.

Whenever a shifted cloud patch for a certain height matches the corresponding patch of the reference shadow mask, this patch is labeled as cloud shadow and is removed from the list of cloud pixels to be processed during the cloud shadow detection. This approach can handle different cloud heights in the various parts of a scene.

The critical issues are the cloud mask itself and the definition of the reference shadow mask. Even if both masks are correct, the proposed method will fail if a scene contains bright pixels with $\rho(TOA, NIR) > t_{NIR}$ in the shadow region.

2.4 Shadow mask (pass 2)

The purpose of this step is to remove bright pixels from the shadow mask. Since 'bright' is a relative term, the labeling is scene-dependent. First we use the shadow mask of pass 1 and exclude cloud shadow pixels calculated in the previous step. To adequately handle the concept 'bright' we use the red band reflectance as a criterion. We distinguish between desert and non-desert-scenes employing the red band threshold $t_{red,desert} = 0.28$ for the scene-average reflectance $\bar{\rho}^*_{red}$ of the clear part of the scene.
So if $\bar{\rho}^*_{red} > t_{red,desert}$ then it is treated as a desert scene else not. In addition, we use another threshold $t_{NIR,s} = 0.10$ for non-desert scenes to exclude pixels with $\rho^*_{NIR} > t_{NIR,s}$, because these are likely too bright for a shadow region. For a desert scene we employ the higher threshold $t_{NIR,s} = 0.15$ to exclude bright pixels from the shadow mask.

2.5 Water / shadow discrimination

This is step 9 of the iterative algorithm, compare Fig 2.1. If a pixel is classified as water and shadow then it is labeled as water. In most cases this decision improves the land / water mask.

2.6 Bright water mask

Bright water bodies contain a large amount of sediment or can consist of clear shallow water over bright sand. The corresponding TOA reflectance spectra are not accounted for in the standard water classification and have to be treated separately. The reflectance thresholds for bright water are:

$$bright\ water: \ \rho^*_{green} < 0.25 \ \wedge \ \rho^*_{NIR} < 0.12 \ \wedge \ ND2 < -0.20 \tag{2.20}$$

where $ND2$ is the normalized difference band index ($SW1 = 1.6\ \mu m$ channel)

$$ND2 = \frac{\rho^*_{SW1} - \rho^*_{red}}{\rho^*_{SW1} + \rho^*_{red}} \tag{2.21}$$

If only VNIR bands are available, then the criteria are employed:

$$bright\ water: \ \rho^*_{green} < 0.25 \ \wedge \ \rho^*_{green} > \rho^*_{red} \ \wedge \ \rho^*_{red} > \rho^*_{NIR} - 0.007 \tag{2.22}$$

If a DEM is available, then the slope is calculated and pixels with $slope > 3°$ are excluded from the water mask. Bright water pixels are included in the water mask.

2.7 Topographic shadow

If a digital elevation model (DEM) is available, the topographic shadow can be calculated from the DEM and solar geometry. If $\theta_s, \theta_n, \phi_s, \phi_n$ denote solar zenith angle, terrain slope, solar azimuth and topographic azimuth, respectively, the local solar illumination angle β can be obtained from the DEM slope and aspect angles and the solar geometry:

$$cos\beta(x,y) = cos\theta_s \ cos\theta_n(x,y) + sin\theta_s \ sin\theta_n(x,y) \ cos\{\phi_s - \phi_n(x,y)\} \tag{2.23}$$

Topographic shadow occurs if $\beta \geq 90°$. However, to be on the safe side and tolerate some DEM errors we define topograhic shadow if $\beta \geq 89°$. If a pixel is classified as topographic shadow and cloud, then then cloud label prevails.

ATCOR delivers three classification maps:

- the standard preclassification (file *'*_out_hcw.bsq'*) containing 22 classes, see Table 2.1.
- a compact classification map with 7 classes *'*_out_csw.bsq'*), see Table 2.2.
- a DDV map (Dense Dark Vegetation, reference pixels for the aerosol retrieval, see chapter 4), also including water (file *'*_atm_ddv.bsq'*).

In addition, the 'dehaze' module (if run before atcor) provides a haze classification map (file *'*_haze_map.bsq'*).
Figure 2.2 presents some of the classification results for a subset of a Landsat-8 scene. The scene contains many smaller non-cirrus clouds and a large cirrus cloud. The left part shows the original data (color infrared rendition, RGB = 865, 655, 560 nm), the right the *'hcw'* classification (brown: land, dark black: shadow, lighter black: cloud shadow, blue: water, different shades of yellow: thin to thick cirrus clouds).
Fig. 2.3 presents another Landsat-8 subset containing non-cirrus clouds (coded grey in the classified scene), cloud shadow, and water. The *'hcw'* classification correctly identifies water and cloud

label	definition	color coding
0	geocoded background	grey
1	shadow	dark black
2	thin cirrus (water)	light blue
3	medium cirrus (water)	medium blue
4	thick cirrus (water)	darker blue
5	land	brown
6	saturated	red
7	snow/ice	white
8	thin cirrus (land)	light yellow
9	medium cirrus (land)	medium yellow
10	thick cirrus (land)	darker yellow
11	thin haze (land)	yellow
12	medium haze (land)	darker yellow
13	thin haze/glint (water)	blue/yellow
14	med. haze/glint (water)	dark blue/yellow
15	cloud/land	bright grey
16	cloud/water	blue/grey
17	water	dark blue
18	cirrus cloud	green/yellow
19	cirrus cloud thick	dark green/yellow
20	bright surface	bright grey
21	topographic shadow	grey/black
22	cloud shadow	black

Table 2.1: *Class label definition of "hcw" file.*

shadow areas, which are often difficult to distinguish.

Lastly, Fig. 2.4 presents an example of visible/ near_infrared (VNIR) imagery (Worldview-2, true color rendition). Since no cirrus band is available, haze detection has to be performed solely with VNIR bands. The yellow color in the classified scene represents haze. The haze area is larger than estimated visually, because very thin (sub-visual) haze is also detected and included. The grey regions correspond to bright objects where the haze thickness map is interpolated.

2.8 Cloud, water, snow probability

In the previous sections spectral criteria were employed to classify cloud, water, and snow/ice. In reality the decision is typically not unique and a class assignment has only a certain probability. As the absolute probability is very difficult to assess, we use a simple 1-parameter equation to estimate a relative probability, which is scaled from 0 to 100 to use maps with integer (actually byte) data.

Cloud probability:
If a pixel belongs to the cloud class then the TOA reflectance of the red band is used together with a linear scaling between the two reflectance thresholds $T_{c1} = 0.15$, $T_{c2} = 0.35$ and the corresponding

label	definition	color coding
0	geocoded background	grey
1	clear	brown
2	semi-transparent cloud	yellow
3	cloud	bright grey
4	shadow	black
5	water	dark blue
6	snow/ice	white
7	topographic shadow	grey/black

Table 2.2: *Class label definition of "csw" file.*

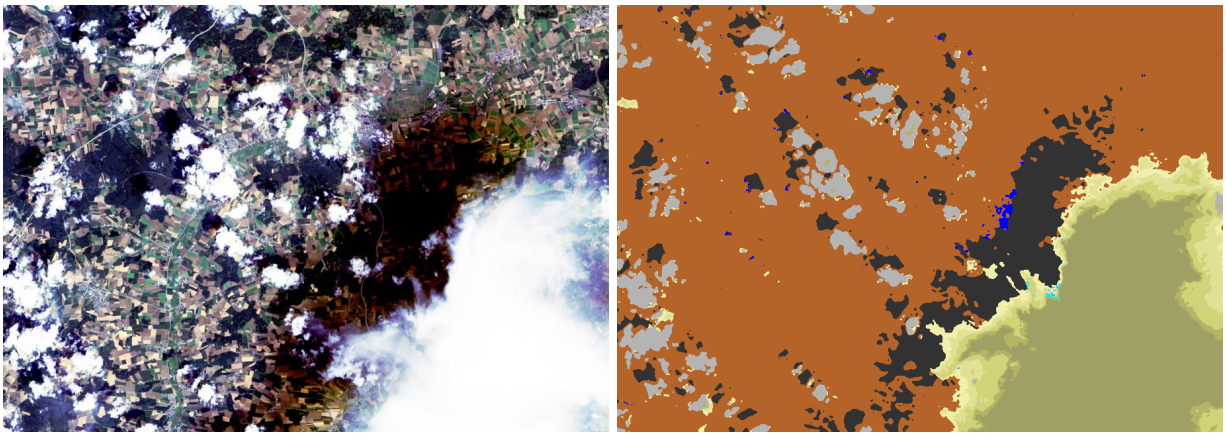

Figure 2.2: *Landsat-8 preclassification (example 1).*

probabilities p1=60% and p2=100%:

$$p(cloud) = p1 + (p2 - p1) * \frac{\rho^*(red) - T_{c1}}{T_{c2} - T_{c1}} \tag{2.24}$$

Probabilities higher than 100 are truncated to 100, values lower than 30 are reset to 30.

Water probability:
If a pixel belongs to the water class then the NDVI is used together with a linear scaling between the two NDVI thresholds $T_{w1} = -0.30$, $T_{w2} = 0.10$ and the corresponding probabilities p1=60% and p2=100%:

$$p(water) = p1 + (p2 - p1) * \frac{NDVI - T_{w1}}{T_{w2} - T_{w1}} \tag{2.25}$$

Probabilities higher than 100 are truncated to 100, values lower than 30 are reset to 30.

Snow /ice probability:
If a pixel belongs to the snow/ice class then the NDSI is used together with a linear scaling between the two NDSI thresholds $T_{s1} = 0.70$, $T_{s2} = 0.25$ and the corresponding probabilities p1=60% and p2=100%:

$$p(snow) = p1 + (p2 - p1) * \frac{NDSI - T_{s1}}{T_{s2} - T_{s1}} \tag{2.26}$$

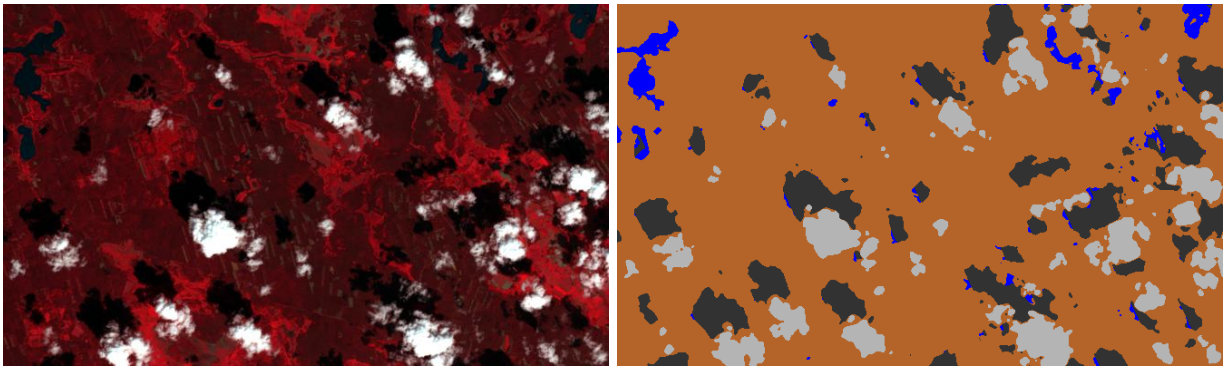

Figure 2.3: *Landsat-8 preclassification (example 2).*

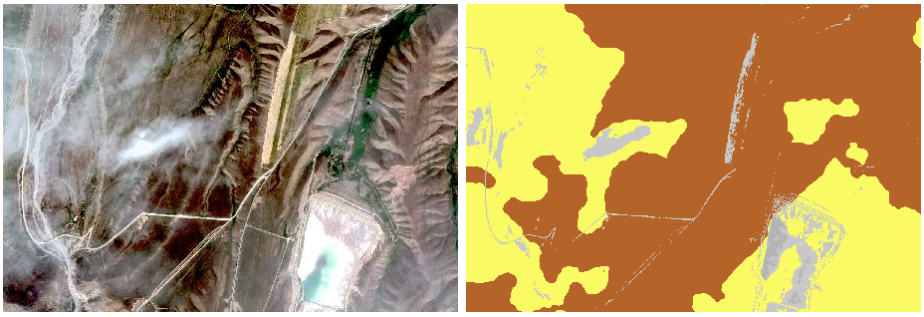

Figure 2.4: *Worldview2 preclassification (example 3).*

Probabilities higher than 100 are truncated to 100, values lower than 30 are reset to 30.

The data is stored as a 3-channel file *'scene_quality.bsq'* if a 1.6 μm band exists, else as a 2-channel file.

2.9 Surface reflectance quality

A scene quality confidence layer map ('scene_atm_qcl.bsq') for a file 'scene.bsq' is available indicating the overall relative quality of the surface reflectance product. The values range from 0 - 100, with 100 the best quality. Among other factors, the overall quality depends on the aerosol optical thickness at 550 nm (AOT550) and the solar zenith angle (SZA). In mountainous terrain, the local SZA is used, and the critical DEM region is defined for areas where the local SZA exceeds 70°. Shadow pixels are assigned the quality value Q=20, cloud pixels Q=10. Figure 2.5 presents the functions Q(SZA) and Q(AOT550). The final quality confidence value is the product Q = Q(SZA) * Q(AOT550), while also considering the shadow, cloud classification. No quality confidence file is written for a flat terrain scene with constant visibility, because SZA and AOT550 do not vary (at least for small FOV imagery).
A future enhancement might account for the quality of the DDV (Dense Dark Vegetation) reference mask, i.e. the higher the SWIR channel (1.6, 2.2 μm) DDV reflectance, the lower the accuracy of the aerosol and surface reflectance products.

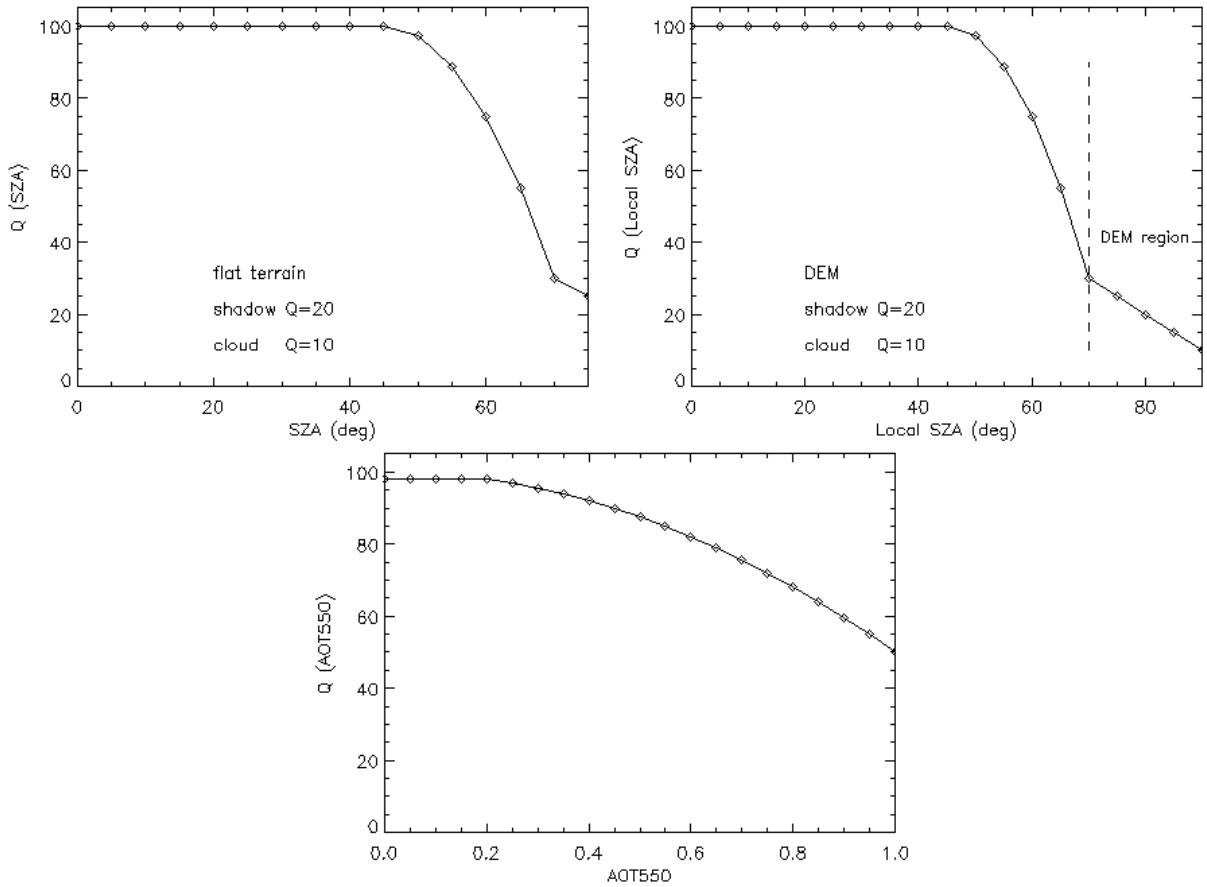

Figure 2.5: *Quality confidence Q(SZA) and Q(AOT550).*

Chapter 3

Atmospheric Look-Up Tables (LUTs)

The atmospheric correction is based on an inversion of the radiative transfer (RT) equation. An efficient approach is the use of LUTs calculated off-line to avoid the execution of an RT code per scene or even per pixel. Therefore, atmospheric LUTs are calculated for a wide range of atmospheric conditions, solar and view geometries, and ground elevations, employing the MODTRAN5.4.0 radiative transfer (RT), and LUT interpolation is performed if necessary. Separate LUTs are calculated for the solar reflective spectrum 0.34 - 2.55 μm and the thermal spectrum 7 - 14.9 μm.

3.1 Extraterrestrial solar irradiance

Although the solar constant (wavelength-integrated extraterrestiral spectral solar irradiance for the earth-sun distance of 1 Astronomical Unit) is known with an accuracy of 0.5%, the spectral irradiance accuracy is much less. It depends on the spectral region and bandwidth. Larger differences up to 5% or 10% exist especially in the 400 - 530 nm region, if the bandwidth is 10 nm or about 3 nm, respectively. As an example, Figure 3.1 in Appendix B contains a comparison of the Fontenla-2011 and Kurucz-1997 spectra for bandwidths FWHM (Full Width at Half Maximum) of 0.4 nm, 2.8 nm, and 10 nm.

Different irradiance sources are offered with the MODTRAN distribution, and we select as standard the Fontenla 'medium2 activity sun' [30], i.e. the MODTRAN files "SUN*med2irradwnNormt.dat" [10], which contain solar spectra for resolutions of 15, 5, 1, and 0.1 cm^{-1}.
We use all four files in ATCOR to achieve a spectral sampling distance (SSD) of about 0.4 nm in the 0.34 - 2.55 μm spectral region. If a customer wants to use another solar irradiance spectrum, the following alternatives are offered: the Kurucz 1997 and New Kurucz 2005 models [10], and the Thuillier 2003 model [137]. In MODTRAN the Thuillier spectrum is padded with the Kurucz 1997 spectrum beyond wavelength 2.4 μm, because the original Thuillier spectrum terminates at this wavelength. The Thuillier spectrum is used for the Sentinel-2 LUTs as requested by ESA.

A tool is available in ATCOR to convert from one irradiance model to another one. The solar irradiance models are stored in ATCOR's folder *'sun_irradiance'*. The high-resolution LUTs are stored in ATCOR's folder *'atm_database'*, and the sensor-specific LUTs in a sub-directory of *'atm_lut'* together with a file *'irrad_source.txt '* documenting the employed solar irradiance.

3.2 LUTs for the solar spectrum 0.34 - 2.55 μm

The off-line part of ATCOR consists of a program ATLUT to compile a high spectral resolution (0.4 nm) database (termed 'monochromatic' here) of MODTRAN runs covering the solar spectrum 0.34 - 2.55 μm. The MODTRAN runs are performed with the scaled DISORT algorithm using 8 streams and the correlated k option, see [43] for details. ATLUT runs the MODTRAN code multiple times to generate the LUTs for a wide range of atmospheric and geometric conditions and to extract the required functions needed for atmospheric correction. The second part (program MLUT) merges the output files of ATLUT into the final database structure and calculates the radiative transfer functions in the spectrum 0.34 - 2.55 μm for an equidistant 0.4 nm wavelength grid convolved with 0.4 nm Gaussian spectral response functions. Currently, this database has 5520 spectral grid points.

The monochromatic files for the solar reflective spectrum are calculated for 4 aerosol types (rural, urban, maritime, desert) and 6 water vapor columns (at sea level: 0.4, 1.0, 2.0, 2.9, 4.0, 5.0 cm). The water vapor content and aerosol type are included in the LUT file name, an example is 'h99_wv20_rura.bp7', where the '.bp7' indicates the monochromatic LUTs.

The monochromatic LUTs are stored in a folder '../atcor/atm_database/', while the sensor-resampled files are in a folder '../atcor/atm_lib/sensor_xxx/', with 'sensor_xxx' representing the sensor name, and an example of a sensor-resampled LUT file name is 'h99_wv20_rura.atm'.

For satellite sensors, the orbit height is assigned the symbolic 99 km height. Each file contains RT functions for the different sets of solar zenith angle, visibility (or aerosol optical thickness) and ground elevation. The corresponding file names include the platform height, sea-level water vapor column, and aerosol type, e.g. 'h99_wv04_rura.bp7'.

Table 3.1 shows the corresponding 6-D parameter space for the monochromatic LUTs. The choice of the grid points is a compromise: a higher number of grid points enables a higher accuracy, but increases the size of the database and the interpolation time. This table represents the current state of the parameter space as defined in ATCOR.

For airborne applications LUTs are provided for the following set of flight altitudes: 0.1, 1, 2, 3, 4, 5, 10, and 20 km. Flight altitude interpolation of the LUTs is performed if necessary. The airborne database is evaluated for the nadir view, and the off-nadir view and relative azimuth angle effects are treated with an approximation (see chapter 3.7). The reason is to keep the database size and interpolation requirements within reasonable limits.

Parameter	Range / Grid points
Visibility	7, 10, 15, 23, 40, 80, 120 km
Solar zenith angle	0 - 70°, incr. 10°
Relative azimuth	0 - 180°, incr. 30°
Sensor earth incidence angle	0 - 40°, incr. 10°
Water vapor column	0.4, 1.0, 2.0, 2.9, 4.0, 5.0 cm
Ground elevation	0, 0.7, 1.5, 2.5, 4.0 km

Table 3.1: *Solar region: 6-D parameter space for the monochromatic spaceborne database.*

Seven radiative transfer terms are stored in the database: path radiance, diffuse solar flux (at sensor), direct (beam) irradiance (at sensor), direct and diffuse ground-to-sensor transmittance, spherical albedo, and direct sun-to-ground transmittance. These functions are needed for the atmospheric correction in the solar region, see chapters 3.7, 6, and 6.2.

LUTs with different water vapor columns are required to retrieve the pixel-dependent water vapor column from imagery if the proper spectral bands exist (see chapter 6). In addition, the RT functions in spectral regions affected by water vapor absorption, depend on the water vapor column, and so does the surface reflectance retrieval. We provide LUTs for summer conditions (dry to humid) and winter conditions.

The LUTs for summer conditions cover the water vapor range 0.4 - 5.0 cm, they are based on MODTRAN's mid-latitude summer profiles of air temperature and humidity. They also cover humid tropical conditions. But for dry winter conditions, a separate database is computed with the mid-latitude winter atmosphere, where four water vapor grid points (0.2, 0.4, 0.8, 1.1 cm) are employed (currently only for the EnMAP mission). The decision on the use of the summer or winter LUTs is based on the global land surface temperature maps from MODIS: if the mean value of the temperature map (for an EnMAP scene) is less than 5° the winter LUTs are taken.

The monochromatic LUTs are generated with the program ATLUT executing multiple MODTRAN runs for a fixed view geometry. Program MLUT combines all view geometries (e.g. nadir, 10°, 20°, 30°, 40° off-nadir) into a single file. Program RESLUT then performs the spectral resampling for the channels of the selected sensor.

The LUTs are compiled for a sun-earth distance *d=1 (Astronomical Units)*. When processing a scene, the recorded at-sensor radiance for a specific date is converted into the corresponding radiance for *d=1* before retrieving the surface reflectance. Using the excentricity (*'ec'*) of the earth orbit and the day of the year (*'doy'*) of the acquisition date, the distance *'d'* is calculated as

$$d(doy) = 1 + ec * sin(2\pi(doy - 93.5)/365) \tag{3.1}$$

Slightly different equations also exist for this purpose, they usually agree within 0.3% with equation 3.1.

3.3 LUTs for the thermal spectrum 7.0 - 14.9 μm

For the thermal region the corresponding high-resolution database is also calculated for 6 water vapor columns (at sea level: 0.4, 1.0, 2.0, 2.9, 4.0, 5.0 cm), but with a fixed aerosol type (rural). The aerosol type has a minor influence, because of the much longer wavelength compared to the solar reflective spectrum. Therefore, only the water vapor content is included in the LUT file name, but not the aerosol type. An example file name is 'h99_wv20_bt7', where the '.bt7' indicates the monochromatic thermal LUTs.

In ATCOR we employ a spectral sampling distance of SSD=0.4 cm^{-1} for the wavelength region 7 - 10 μm, i.e. corresponding to a wavelength SSD=2 - 4 nm, and SSD=0.3 cm^{-1} for the wavelength region 10 - 14.9 μm, i.e. corresponding to a wavelength SSD=3 - 5.5 nm. A triangular weight function is used with a spectral bandwidth of twice the SSD. In addition, the Isaacs's 2-stream

method is employed including the correlated k algorithm. The Isaacs's algorithm is much faster than DISORT, and yields the same results for our cases in the thermal region. All files ("*.bt7") are calculated for view or scan angles from 0° (nadir) to 40° off-nadir with a 5° increment to enable an accurate interpolation.

In the thermal region, three radiative transfer quantities are required for the atmospheric correction: emitted and scattered path radiance L_p, ground-to-sensor-transmittance τ, and downwelling thermal flux F, see chapter 10. Table 3.2 contains the parameter space for the thermal spaceborne database. Compared to the solar case, the solar zenith and relative azimuth parameters are omitted, but the 5 km visibility is included and the ground elevation increment is narrower (0.5 km). For the airborne case, LUTs are provided for the flight altitudes 0.1, 1, 2, 3, 4, 5, 10, and 20 km. Flight altitude interpolation of the LUTs is performed if necessary.

Parameter	Range / Grid points
Visibility	5, 7, 10, 15, 23, 40, 80, 120 km
Sensor earth incidence angle	0 - 40°, incr. 10°
Water vapor column	0.4, 1.0, 2.0, 2.9, 4.0, 5.0 cm
Ground elevation	0 - 4.0 km , incr. 0.5 km

Table 3.2: *Thermal region: 4-D parameter space for the monochromatic spaceborne database.*

3.4 Set of RT functions (solar and thermal)

The following seven radiative transfer (RT) functions are stored in the solar reflective atmospheric database:

- path radiance L_p $[mWcm^{-2}sr^{-1}\mu m^{-1}]$
- direct (beam) transmittance (ground-to-sensor) τ_{dir} [0 - 1]
- diffuse transmittance (ground-to-sensor) τ_{dif} [0 - 1]
- direct sun-to-ground transmittance τ_{sun} [0 - 1]
- direct (beam) solar irradiance at sensor (sun-to-ground-to-sensor) $[mWcm^{-2}\mu m^{-1}]$
  $E^s_{dir} = (\tau_{dir} + \tau_{dif}) \cdot \tau_{sun} \cdot E_0$, where E_0 is the extraterrestrial solar irradiance
- diffuse solar flux at sensor $E^s_{dif} = (\tau_{dir} + \tau_{dif}) \cdot E_{dif}$, where E_{dif} is the diffuse solar flux on the ground $[mWcm^{-2}\mu m^{-1}]$
- spherical albedo (atmospheric backscatter) s [0 - 1]

The reason for storing the product terms is the resampling with the channel spectral response function $R(\lambda)$ and the fact that the integral of two or three product functions is not equal to the product of the corresponding integrals (unless for the trivial case where the functions are constant), e.g. for functions $f_1(\lambda)$, $f_2(\lambda)$:

$$\int_{\lambda_1}^{\lambda_2} f_1(\lambda)\ f_2(\lambda)\ R(\lambda)\ d\lambda \neq \int_{\lambda_1}^{\lambda_2} f_1(\lambda) R(\lambda)\ d\lambda \cdot \int_{\lambda_1}^{\lambda_2} f_2(\lambda) R(\lambda)\ d\lambda \tag{3.2}$$

Therefore, the atmospheric database stores the integral of the product terms. However, the following chapters formulate the channel-integrated equations with the individual terms to emphasize the physical background. The papers [93, 94] illustrate the error if the bandpass-resampling effect is neglected.

For the thermal region there are three RT functions, see chapter 10:

- path radiance L_p $[mWcm^{-2}sr^{-1}\mu m^{-1}]$
- ground to sensor transmittance τ [0 - 1]
- thermal flux on the ground $F[mWcm^{-2}\mu m^{-1}]$

3.5 Ozone LUTs

For satellite sensors the influence of ozone can also be included. This information usually has to be taken from an external source (ozone-measuring instruments or ozone forecast models). The default ozone column in the LUTs is 330 DU (Dobson Units) for sea level, and because ozone can be decoupled from the other atmospheric parameters, a separate ozone LUT can be compiled [103]. In ATCOR it covers the ozone concentrations 200 - 500 DU with extrapolation to 100 - 600 DU.

The LUTs are calulated for the wavelength range 450 - 800 nm, on a 10 nm grid, and a 10 nm spectral averaging, which is sufficient because the ozone spectral transmittance does not vary rapidly.

The supported range of satellite view zenith angles is 0°- 40°, increment 10°, and the supported solar zenith angle range is 0°- 70°. increment 10°, see Table 3.3. Due to the small spatial variation of ozone, the ozone value can be considered as constant per scene (for high and medium spatial resolution sensors). The ozone value is specified in the input parameter file (".inn"), see the ATCOR manual. Since the ozone content peaks in the 20 - 40 km altitude region, the variation of ground elevation can be neglected for elevations 0 - 4 km (the influence is smaller than about 3%).

Parameter	Range / Grid points
Spectral range	450 - 800 nm, incr. 10 nm
Solar zenith angle	0 - 70°, incr. 10°
View zenith angle	0 - 40°, incr. 10°

Table 3.3: *Parameter space for ozone LUTs.*

3.6 Resampling of atmospheric database

For each supported sensor the spectral channel response functions are needed. In order to support analytical and non-analytical functions it was decided to use tables of these functions. Therefore, in the 'sensor' folder there is a sub-folder for each supported instrument containing ASCII files of tables of the response functions. Each table contains two numbers per line (wavelength in μm, response between 0 and 1). The file names are arbitrary, but should contain the band number and the extension '.rsp', e.g. 'band01.rsp' to 'band99.rsp' or 'band001.rsp' to 'band450.rsp'.

Program RESLUT uses the monochromatic database files and convolves them with the sensor-specific response functions to obtain the sensor-specific RT functions. Additionally, the above set of ground elevations is interpolated to a 0.5 km grid, and for the solar spectrum the visibility grid point 5 km is included with extrapolation. The file names correspond to the monochromatic parent names, but the extension is '.atm' and these files are stored in the 'atm_lib' folder.

Directory structure (example with DESIS and ENMAP sensors):
- sensor
  - ENMAP
  - DESIS
- atm_database
  - h99_wv04_rura.bp7
  - ...
  - h99_wv50_rura.bp7
- atm_lib
  - ENMAP
    - h99_wv04_rura.atm
    - ...
    - h99_wv50_rura.atm
  - DESIS
    - h99_wv04_rura.atm
    - ...
    - h99_wv50_rura.atm

3.7 Off-nadir approximation of the airborne database

Since the size of the monochromatic database is very large and the airborne case requires height-dependent RT functions, it was decided to calculate the airborne database only for the nadir view and use some approximations for the off-nadir geometries.

The path radiance correction factor with respect to nadir is calculated for three solar zenith angles (20, 35, 45°), four relative azimuth angles (30, 60, 85, 179°), four aerosol types (rural, urban, maritime, desert), 10 wavelengths from 0.4 to 2.2 μm, and flight altitude 4 km. Since these are relative factors the dependence on flight altitude is small. If necessary, linear angular interpolation / extrapolation is performed.

The view angle-dependence of the direct and diffuse solar flux (E) at the sensor is computed as:

$$E(\theta_v) = E(nadir)\ \frac{\tau_{dir}(\theta_v) + \tau_{dif}(nadir)}{\tau_{dir}(nadir) + \tau_{dif}(nadir)} \tag{3.3}$$

where θ_v is the off-nadir view angle, and $\tau_{dir}(\theta_v)$ the direct transmittance (ground-to-sensor), compare chapter 3.4.

$$\tau_{dir}(\theta_v) = exp\ \{ln(\tau_{dir}(0))\ /\ cos(\theta_v)\} \tag{3.4}$$

The view angle dependence of the diffuse transmittance is small for off-nadir view angles smaller than 40° and it is neglected here.

3.8 Airborne LUTs and refractive index

As the wavelength of electromagnetic radiation depends on the refractive index of the medium, this effect has to be calculated for airborne sensors if a high accuracy is needed, especially for hyperspectral instruments. The spectral channel filter functions are usually measured in the laboratory. So the measured wavelength depends on the refractive index n_{lab} or pressure p_{lab} at the elevation h_{lab}, during lab measurement. If λ_0 denotes the wavelength in vacuum, i.e. $n_{vac} = 1$, the sensor wavelength during a lab measurement is:

$$\lambda_{sen}(p_{lab}, h_{lab}) = \frac{\lambda_0}{n_{lab}} \tag{3.5}$$

We assume a typical scale height H = 8 km for the height dependence of pressure and air density, i.e.

$$p(h) = p(h = 0)\ exp\ (-h/H) \tag{3.6}$$

For a standard atmosphere (mid-latitude summer) we have $p_0 = p(h = 0) = 1013$ mbar (hPa).

For a spaceborne sensor the lab measurement is performed in a vacuum chamber, therefore n_{lab} is close to 1 and $\lambda_{sen} = \lambda_0$. The MODTRAN radiative transfer calculations employed for the current look-up tables (LUTs) are performed on the basis of wavenumber w (cm^{-1}) which is converted into wavelength λ (μm) using

$$\lambda = \frac{10000}{w\ n(h)} \tag{3.7}$$

For a spaceborne sensor we have n=1, but for airborne sensors we have to account for the refractive index n(h) in two respects:

- The MODTRAN wavenumber has to be converted into a wavelength λ using eq. (3.7) taking care of the refractive index for the corresponding flight altitude h (or pressure level p). Eq. (3.6) is used to convert the flight altitude into the corresponding pressure. Switching to wavelength is required, because the high-resolution spectral database of atmospheric LUTs has to be convolved with the channel filter functions delivered as wavelength data.
- The instrument channel filter functions (spectral response files) are usually measured in the laboratory. If the lab measurements are not conducted in a vaccuum chamber, but for a certain pressure level p_{lab} and the corresponding height h_{lab} (see eq. 3.6), then these functions also have to be adapted to the refractive index at the flight altitude as described in the next equations (3.8 to 3.11).

We use the equation:

$$n(h) = 1\ +\ 0.000293\ exp\ (-h/H) \tag{3.8}$$

Therefore, the MODTRAN wavelength conversion is

$$\lambda_{MOD} = \frac{10000}{w\ n(h)} = \frac{\lambda_0}{n(h)} \tag{3.9}$$

The lab wavelength conversion for pressure p_{lab} and height h_{lab} is

$$\lambda_{sen}(h_{lab}) = \frac{\lambda_0}{n(h_{lab})} \tag{3.10}$$

Eq. (3.6) is used to calculate the pressure p for a given flight altitude h and vice versa. Using the parameter h to indicate the pressure-dependence of the refractive index n(h) we get

$$\lambda_{sen}(h) = \frac{\lambda_0}{n(h)} = \frac{\lambda_{sen}(h_{lab})\ n(h_{lab})}{n(h)} \tag{3.11}$$

The wavelength change or shift is calculated as :

$$\Delta_{MOD} = \lambda_{MOD}(h)\ -\ \lambda_0 \tag{3.12}$$

$$\Delta_{sen} = \lambda_{sen}(h)\ -\ \lambda_{sen}(h_{lab}) \tag{3.13}$$

Figure 3.1 (top) shows the calculated wavelength shifts for MODTRAN required for 3 flight altitudes (1, 4.2, 100 km). The 4.2 km corresponds to a pressure level of 600 (hPa, mbar). Note:
If the sensor is contained in a pressurized chamber at p=600 hPa, this pressure level has to be used for the calculation of the sensor wavelength shift independent of the actual flight altitude. This means the MODTRAN wavelength shift also has to be adapted to this pressure level, i.e. using the corresponding virtual flight altitude of 4.2 km.

Figure 3.1 (middle, left and right) show the lab wavelength shifts for the 2 cases of p_{lab} = 1013 hPa and p_{lab} = 940 hPa to study the influence of lab measurements at sea level (1013 hPa) and at a higher elevation (598 m above sea level).

The new MODTRAN wavelengths have a negative shift, indicating they are smaller than the original λ_0 (shifted left to shorter wavelengths), whereas the lab wavelengths have a positive shift, i.e. they are shifted to the right to longer wavelengths. Therefore, the combined shift (MODTRAN and lab) is not the sum but the difference of these shifts.

The combined total shift is shown in the bottom two plots: the left one represents the case with p_{lab} = 1013 hPa, the right one with p_{lab} = 940 hPa. Both cases are very similar with a slightly higher shift for the 1013 hPa case.

The total shift plots show that some compensation effects exist, e.g. for h=100 km the MODTRAN wavelength shift is 0 and the lab shift is largest. The opposite trend is observed for h=1 km, where the MODTRAN shift is largest and the lab wavelength shift is small. Therefore, the three altitude cases coincide on one line. The total shift increases with wavelength and is largest in the thermal spectral region.

There is a slight dependence of the results on the assumed scale height H=8 km and the sea level pressure p0=1013 hPa. The scale height actually depends on the temperature and humidity profile, the average mass of atmospheric particles, and location (because of the acceleration of gravity). It can be approximately calculated with the equation of hydrostatic equilibrium using the ideal gas law, see any textbook on atmospheric physics.

As ATCOR may be used by customers all over the world and the specific atmospheric state is usually not known, a typical “standard” scale height of H=8 km is taken. For typical summer and winter conditions, the scale height varies between 8.0 and 8.5 km. The wavelength difference due to the air refractive index for H=8.0 km versus H=8.5 km is smaller than 0.06 nm in the wavelength region 0.4 to 10 μm. Therefore, the use of H= 8.0 km is sufficient for practical purposes.
Some examples:

- The AVIRIS NG (Next Generation) spectrometer is operated under near vacuum (10 Torr, 13.3 mbar) conditions.
- The APEX spectrometer has a pressure regulation unit keeping the optical subunit at 200 mbar above ambient flight altitude pressure [50].
- Most airborne spectrometers operate under ambient flight altitude pressure.

The next table shows the default contents of file "pressure.dat". The file is created for each sensor in the sensor-specific folder during the first run of the RESLUT (resampling) module if no "pressure.dat" exists. The user should edit the first line of the file if necessary, to specify the appropriate lab pressure, and the relative or absolute instrument pressure during flight operation.

1013.0	R0.0	lab pressure, instrument pressure (mbar, hPa) instrument pressure is relative or absolute R=r=relative pressure above ambient flight altitude A=a=absolute pressure

Table 3.4: *Default file "pressure.dat".*

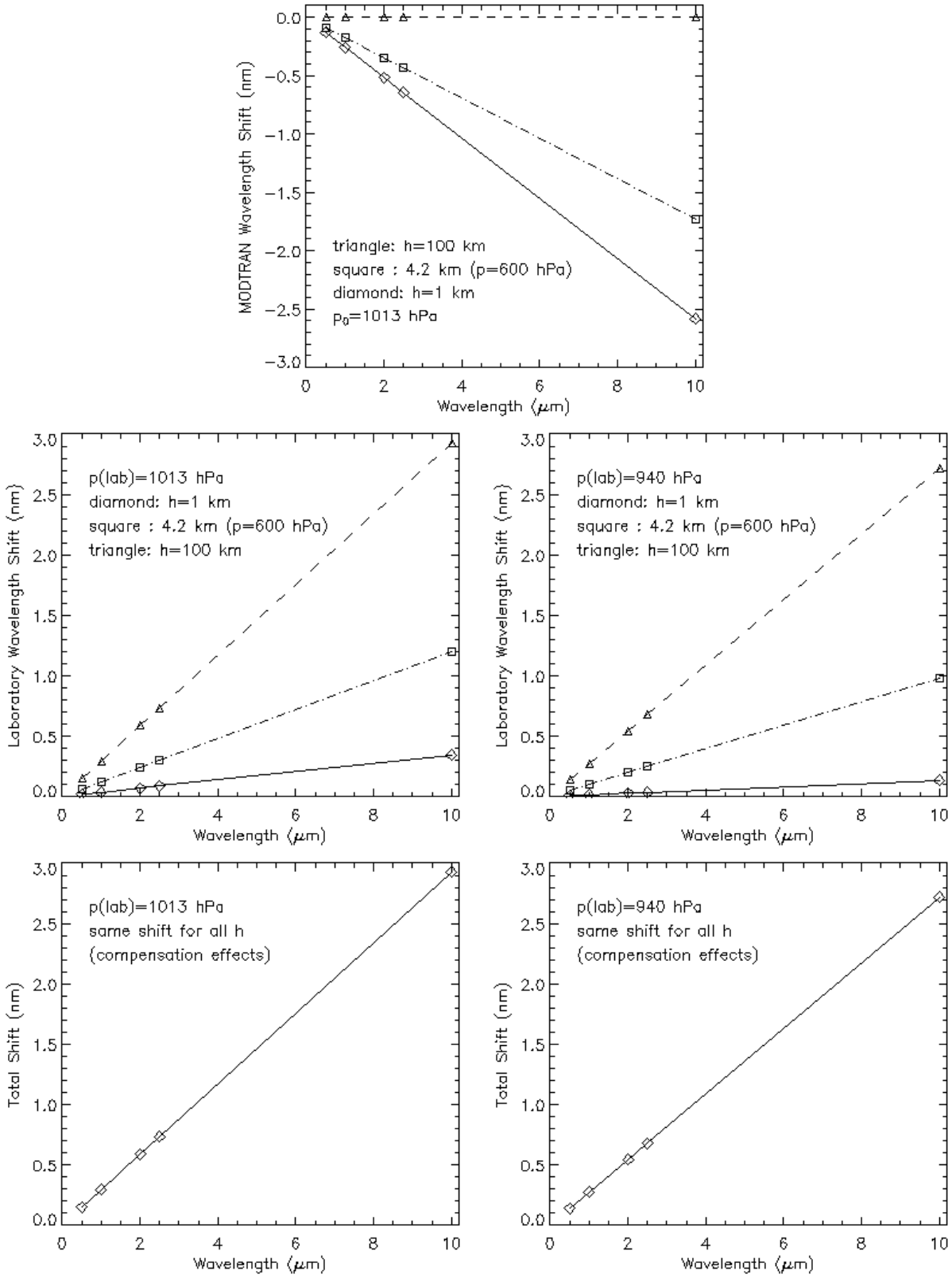

Figure 3.1: *MODTRAN and lab wavelength shifts (see discussion in the text).*

Chapter 4

Aerosol Retrieval

The standard aerosol retrieval over land uses reference pixels (DDV = dense dark vegetation, and dark soil) to determine the aerosol optical thickness at 550 nm (AOT550) or the corresponding visibility. The known spectral correlation of surface reflectance between certain bands is then exploited to calculate the aerosol properties [61, 67].
The principal idea is to detect dark reference pixels in a channel without much influence by the atmosphere (e.g. around 2.2 μm). This is a close representation of the surface reflectance in this channel. Then the spectral correlation with visible bands (400 - 680 nm) is used to obtain the surface reflectance in the visible bands that are strongly influenced by the atmosphere. The next step calculates a set of simulated TOA radiance values as a function of AOT550 or visibility for the selected visible bands. The actual AOT/visibility is then obtained as the intersection of the simulated TOA radiance curve and the measured TOA radiance value, see chapter 4.3.
The molecular (Rayleigh) scattering contribution is known analytically and taken into account separately. The retrieval algorithm depends on the available spectral bands:

- bands in the visible (blue, red), NIR, and SWIR1 (1.6 μm) or SWIR2 (2.2 μm)
- only bands in the visible (blue, red), NIR
- only bands (green, red, and NIR) or (red, NIR)

The highest accuracy can be expected for the first algorithm with the SWIR bands.. The default aerosol type is rural (continental). There is an option to estimate the aerosol type from the scene provided the scene contains enough reference pixels (minimum 2%). Currently four aerosol MODTRAN types are implemented: rural, urban, maritime, desert.

IF not enough DDV pixels are available, i.e. for arid or desert scenes, then the DDVS (DDV Substitute) algorithm is performed, as presented in chapter 4.4.

4.1 DDV reference pixels

A general prerequisite for reference pixels is a certain minimum distance to cloud pixels and we select a distance of 500 m. Additionally, cloud shadow pixels and cirrus/haze affected pixels are not included as reference. In rugged terrain, pixels with a local solar zenith angle $> 70°$ are also excluded.

The search for dense dark (DDV) reference pixels can be best conducted with SWIR bands. The search could be conducted with the TOA reflectance, but we use a slightly better approach and select a visibility of 23 km and perform an atmospheric correction for the selected band. A question is whether this DDV start visibility should be iterated after the calculation of the final visibility / aerosol optical thickness map at 550 nm (AOT550). To answer the question, ten scenes of sensors with a SWIR2 band (Landsat-5, Landsat-8, Sentinel-2) were evaluated by varying the DDV start visibility between VIS=10 km and VIS=120 km. The difference of AOT550(VIS) - AOT550(23km) was less than 0.012, demonstrating that an iteration is not necessary. Nevertheless, this approach is better than the use of the TOA reflectance. Then reference pixels are determined with:

$$0.01 < \rho(\lambda) < T_1 \quad and \quad NDVI > 0.1 \tag{4.1}$$

For a SWIR2 band ($\lambda = 2.2\mu m$) the start value is a threshold $T_1 = 0.05$. If less than 2% reference pixels are found, then T_1 is iteratively increased to 0.10, then 0.12. For a SWIR1 band ($\lambda = 1.6\mu m$) the sequence of T_1 iterations is 0.10, 0.15, 0.24.
The higher the T_1 value, the less accurate are the standard spectral band correlation factors of the SWIR-to-red or NIR-to-red channels (see chapters 4.3.1, 4.3.2, equations 4.4, 4.5, 4.9).

If only VNIR bands are available, then the dark reference pixels are determined with the red and NIR channels, performing atmospheric correction for these channels using a set of three visibilities (10, 23, 60 km), see [98]. Reference pixels are masked with four criteria:

$$\rho(NIR) \geq 0.10 \quad and \quad \rho(NIR) \leq 0.20 \quad and \quad RVI \geq 3 \quad and \quad 0.006 < \rho(red) \geq 0.04 \tag{4.2}$$

RVI is the ratio vegetation index, i.e., $RVI = \rho(NIR)\ /\rho(red)$. If a very large percentage of reference pixels (> 45%) is found for $\rho(red) \geq 0.04$, then the threshold 0.04 is decreased to 0.03. If the percentage is still larger than 22%, then the threshold is decreased to 0.025. If the last iteration yields less than 5% reference pixels, the previous iteration is used. This search is conducted iteratively for the above three visibilities and terminates at once if successful for any of these visibilities. If not successful, the default visibility of 23 km in the input parameter file is used.

4.2 Aerosol type estimation for DDV

After estimating the surface reflectance values in the red ($0.66\mu m$) and blue band ($0.48\mu m$) (see chapter 4.3) the scene-derived path radiances $L_p(scene, red)$ and $L_p(scene, blue)$ can be calculated by subtracting the surface reflected radiance $L_r(\rho_i)$ (i=red, blue) from the total radiance $L(i)$

$$L_p(scene, i) = L(i) \ - \ L_r(\rho_i) \tag{4.3}$$

where ρ_i is the known reflectance of the DDV reference pixel. Then the average of the path radiances is calculated for all reference pixels and the ratio $L_p(scene, blue)/L_p(scene, red)$, which depends on the aerosol type, is compared to the corresponding path radiance ratio for the four MODTRAN aerosol types (rural, urban, maritime, desert). The aerosol type with the closest match is selected. The MODTRAN types represent climatologic averages of aerosol conditions.

4.3 Aerosol optical thickness / visibility

The next sections describe the DDV aerosol algorithms for SWIR and VNIR bands. The aerosol retrieval is performed for the DDV reference areas. The first step detects the reference pixels,

the second step calculates the visibility / AOT550 map based on spectral correlations of surface reflectance and a comparison of measured at-sensor radiance with simulated radiances.
The default option for the calculation of the AOT(550nm) map assigns the average AOT of the DDV areas to the non-DDV pixels. Starting in 2021 an optional inverse distance weighting (IDW) can be used to obtain the AOT550 for the non-reference pixels. The IDW algorithm replaces the former spatial triangulation, which could only be employed for small scenes due to its huge memory requirements. If the scene contains water bodies, the AOT550 of these pixels is also used as input to the IDW algorithm. Finally, a low pass filter with a moving window of 3 km × 3 km is applied to smooth noise and small-scale AOT fluctuations.

4.3.1 DDV algorithm with SWIR bands

If the sensor has a SWIR band (at 1.6 μm or 2.2 μm), then the scene can be searched for dark pixels in this band and a correlation of the SWIR surface reflectance with the surface reflectance in the red and blue band can be employed to estimate the visibility automatically [61]. For this purpose, we use a modified version of the original idea for the following algorithm.

If a SWIR band exists the SWIR surface reflectance is calculated with the atmospheric LUTs assuming a visibility of 23 km (instead of the original version of TOA reflectance). Then, water pixels are excluded by employing only those pixels with SWIR reflectance values above 1% and an NDVI > 0.1. For the 2.2 μm band the upper threshold of the reflectance of the dark pixels is selected as 5%. If the number of reference pixels is less then 2% of the image pixels, then the upper threshold is increased to 10% or finally 12%. If a 1.6 μm band exists, but no 2.2 μm band, the corresponding upper thresholds are selected as 10% and 15%, or finally 18%, respectively. The surface reflectance ratio values for the red (near 0.66 μ) and blue (near 0.48 μm) band are then calculated as :

$$\rho_{red} = 0.5\ \rho_{2.2} \qquad and \qquad \rho_{0.48} = 0.5\ \rho_{0.66} + 0.005 \tag{4.4}$$

$$\rho_{red} = 0.25\ \rho_{1.6} \qquad and \qquad \rho_{0.48} = 0.5\ \rho_{0.66} + 0.005 \tag{4.5}$$

The offset 0.005 for the blue band yields a better correlation with ground measurements than a zero offset [67].

The visibility VIS (or aerosol optical thickness at 550 nm, AOT550) is obtained from an interpolation of the measured at-sensor radiance of each reference pixel $L_m(j) = c_0(j) + c_1(j) \cdot DN$ with the simulated radiance curve $L(VIS_k, j)$ where VIS_k is a set of visibilities (or AOT550 values) and 'j' is the selected band ('j' = red band). Actually, ATCOR uses a visibility range of 5 to 190 km, and this is converted into an integer range 0 to 182, called visibility index, to enable a direct vector / matrix indexing and avoid interpolation. The visibility index vi is closely related to the total optical thickness δ at 550 nm with an equidistant optical spacing of 0.006 for a ground at sea level, and smaller for increasing elevations.

$$\delta = 0.185 + 0.006 * vi \tag{4.6}$$

So a visibility index change of 1 corresponds to an AOT550 change of 0.006. It is easy to calculate the aerosol optical thickness (AOT550nm) from a known total optical thickness by subtracting the Rayleigh optical thickness and a very small trace gas optical thickness (mainly ozone).

Figure 4.1 illustrates the principle of the visibility computation: the dashed horizontal line marks the measured at-sensor radiance for a reference pixel and the solid curve represents the simulated radiance as a function of visibility. The diamond symbol marks the set of visibility simulations and the vertical dashed line indicates the calculated visibility obtained by interpolation. In practice, a large number of radiance simulations (183) is conducted on a dense visibility grid corresponding to a narrow equidistant AOT550 increment of 0.006, providing an accurate interpolation.

If the atmospheric LUTs are compiled with the MODTRAN code and the visibility parameter to quantify the aerosol content, then the AOT550 can be calculated for a given visibility VIS (km) as

$$AOT550 = exp\,(a(z) + b(z)\ ln(VIS)) \tag{4.7}$$

where z is the surface elevation, and a(z), b(z) are coefficients obtained from a linear regression of $ln(AOT)$ versus $ln(VIS)$.

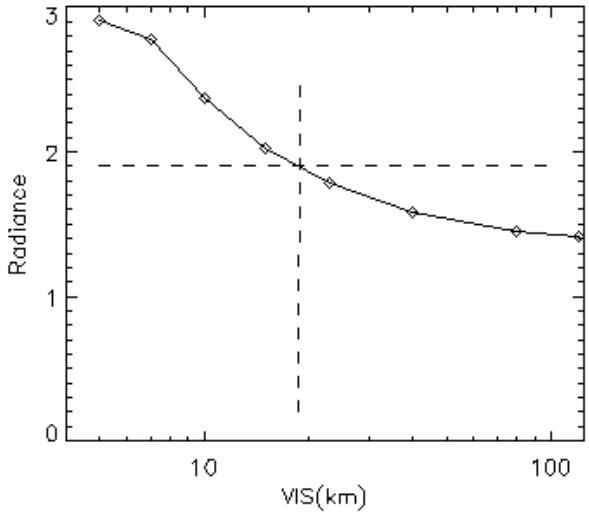

Figure 4.1: *Visibility calculation for reference pixels.*

The standard processing for the visibility/AOT550 retrieval employs the red band, because it is usually less noisy. In addition, eq. (4.5) is used to modify the input aerosol type path radiance in the shortest wavelength blue band 'b' by subtracting the surface reflected radiance from the total measured radiance:

$$L_p(b) = L_m(b) - \tau(b, VIS)\ E_g(b, VIS)\ \rho(b)\ /\ \pi \tag{4.8}$$

Here, τ is the total ground-to-sensor transmittance and E_g the global (i.e., direct plus diffuse) solar flux on the ground. Then the path radiance for channels between wavelength 'b' and red ($0.66\mu m$) is exponentially interpolated to get a better fit to the scene path radiance. The approach is similar to the Angstrom method of calculating the wavelength-dependence of the aerosol optical thickness, but implicitly accounts for the unknown aerosol phase functions.
The non-reference pixels are assigned the average visibility / AOT550 of the reference pixels (default) or a spatial interpolation (triangulation) can optionally be applied. The last step performs an averaging of the visibility/AOT550 map over a moving window of size 3 km × 3 km to reduce noise.

4.3.2 DDV algorithm with VNIR bands

If the sensor has only VNIR bands then the red and NIR band are used to estimate the aerosol content, see [98] for details. The first step searches for dark reference pixels using eq. 4.2. For these pixels the following spectral correlation of surface reflectance is used

$$\rho_{red} = a_1 \ \rho_{NIR} \tag{4.9}$$

where a_1 is specified in the input parameter file (default $a_1 = 0.10$). Similar to the SWIR algorithm, eq. 4.5 relates the blue band surface reflectance to the red band reflectance.

If the percentage of DDV reference pixels is less than 2% of the scene, then additional reference pixels are included based on the ARVI (atmospherically resistant vegetation index), see [112]. The ARVI is defined as:

$$ARVI = \frac{\rho^*_{NIR} - \rho^*_{rb}}{\rho^*_{NIR} + \rho^*_{rb}} \tag{4.10}$$

The asterisk in ρ^* indicates a TOA reflectance with the Rayleigh contribution already subtracted, and

$$\rho^*_{rb} = \rho^*_{red} + 1.3 \ (\rho^*_{red} - \rho^*_{blue}) \tag{4.11}$$

If A_1, A_2 are the lower and upper ARVI thresholds ($A_2 = 0.9$ is fixed) then additional dark reference pixels are searched which fulfill $A_1 < ARVI < A_2$. The inital value is $A_1 = 0.8$, and it is iteratively decreased to $A_1 = 0.64$ until at least 2% of these additional reference pixels are found or the iteration terminates. We use the following simple empirical equation for the surface reflectance in the red band:

$$\rho_{red} = 0.01 + 0.03 \ \frac{ARVI - A_2}{A_1 - A_2} \tag{4.12}$$

In reality, this relationship is dependent on biome, season, and geography [112]. Corresponding maps have been developed for the MERIS sensor, using a coarse reolution of about 3 km x 3 km, but these are not appropriate for high spatial resolution instruments.

If the percentage of DDV reference pixels (including ARVI pixels) is less than 2% of the scene, then the input visibility is used, but it will be updated iteratively if it causes negative reflectance values for dark surfaces in the NIR (e.g., for water bodies).

Finally, the dark reference pixels from both VNIR approaches (eq. 4.9 and 4.12) are combined, and similar to chapter 4.3.1 the visibility VIS (or aerosol optical thickness at 550 nm, AOT550) is obtained from an interpolation of the measured at-sensor radiance of each reference pixel $L_m(j) = c_0(j) + c_1(j) \cdot DN$ with the function $L(VIS_k, j)$ where VIS_k is the set of LUT visibilities (or AOT550 values).

4.3.3 Deep blue bands

For most multispectral sensors a blue channel in the 470 - 490 nm region was the shortest wavelength channel in the past. However, with the availability of Worldview-2 and Landsat-8 OLI and hyperspectral data there is often a need to adjust the path radiance in the deep blue region

< 470 nm, because the limited set of discrete aerosol models might not be adequate. Therefore, an empirical approach is taken: the DDV surface reflectance at 400 nm is set to 0.6 times the reflectance of the standard blue (480 nm) channel and the reflectance for channels in between is linearly interpolated:

$$\rho^{ddv}_{0.400} = 0.6\ \rho^{ddv}_{0.480} \tag{4.13}$$

$$\rho^{ddv}(\lambda) = \rho^{ddv}_{0.400} + \frac{\rho^{ddv}_{0.480} - \rho^{ddv}_{0.400}}{0.480 - 0.400}\ (\lambda - 0.400) \tag{4.14}$$

Multispectral sensors usually have only one or two channels in the 400 - 470 nm region. In case of hyperspectral instruments, the channels closest to 410 nm and 440 nm are selected as tie channels to calculate the corresponding path radiance, and exponential interpolation is used to obtain the path radiances for the remaining bands in the 400 - 480 nm region.

4.4 DDVS reference pixels

If a scene does not contain enough DDV pixels, i.e. for an arid or desert scene, then the DDVS (DDV Substitute) algorithm is employed (only satellite versions of ATCOR). It still searches for vegetation pixels, but relaxes the requirements imposed on DDV. The following conditions are applied:

$$\rho(TOA, NIR) > 0.35 \quad and \quad NDVI > 0.50 \quad and \quad \rho(TOA, red) > 0.01 \tag{4.15}$$

So the top-of-atmosphere (TOA) reflectance in the NIR band (around 850 nm) must be greater than 0.35, the NDVI greater than 0.5 and the TOA reflectance in the red band (around 650 nm) must be greater than 0.01. The NIR threshold value of 0.35 is selected, because the DDV requirement is $\rho(TOA, NIR) < 0.35$ and the DDV algorithm failed. This algorithm is only implemented for the satellite version of ATCOR. It was successfully tested with Sentinel-2 scenes and DESIS hyperspectral scenes of arid and desert regions. According to the above three criteria, visible/NIR bands are sufficient for the DDVS method.

No minimum percentage requirement is imposed on the DDVS, as such regions often contain only a few hundred or a few thousand DDVS pixels and it is better to use this information than the default visibility (23 km). The typical range of surface reflectance for DDV pixels in the red band (around 650 nm) is from 0.01 to 0.022. Since the above criteria also include brighter vegetation and we still want to select substitute dark pixels, the DDVS algorithm discards the brightest 90% of the above pixels. In addition, the surface reflectance in the red band for the remaining 10% of DDVS pixels is set at 0.027, i.e. slightly higher than the typical upper range value for DDV.

$$\rho(red, DDVS) = 0.027 \tag{4.16}$$

Using $\rho(red, DDVS) = 0.027$ the visibility / AOT(550nm) is calculated per pixel, optionally followed by an inverse distance weighting (IDW) for the AOT(550nm) map. If the scene also contains water bodies, the AOT over water is also calculated and included as input to the IDW algorithm. Finally, the AOT(550nm) map is low pass filtered (3 km $\times$ 3 km) to reduce noise and average small scale fluctuations.

4.5 Aerosol retrieval over water

Although the main objective is the aerosol retrieval over land, we also include an approximate aerosol estimate for water bodies. Water is masked during the preclassification (chapter 2) and a check of the water surface reflectance in the red and NIR bands is conducted to avoid negative reflectance values. The surface reflectance of water is assumed as 0.01 in the NIR to calculate the corresponding visibility / AOT(550nm). This is a typical value for non-turbid waters. In case of turbid waters, the AOT will be overcorrected. The AOT(water) and AOT(land) maps are then merged and optionally the inverse distance weighting algorithm is applied. Finally a low pass filter with a moving average (3 km × 3 km) is employed to smooth the land/water transitions.

4.6 Inverse Distance Weighting (IDW)

The inverse distance weighting algorithm is rather time consuming for large arrays. Therefore, the original visibility index / AOT file is reduced to a typical size of 260 × 260 pixels (for a square scene) containing 20 × 20 cells. Additionally, the original scene is split into the corresponding 20 × 20 cells. For each cell of the original scene the mean of the visibility index (water or DDV) is calculated and assigned to the corresponding cell of the reduced scene. Cells without information from water or DDV are empty and their values will be calculated with the IDW algorithm. Special care has to be taken for the background and background border cells. Finally, the reduced image map is resampled to the original size using bilinear interpolation.

4.7 Visibility iterations

Visibility iterations are performed to check whether the calculated visibility from the DDV reference pixels or the user-specified constant visibility leads to surface reflectance values < 0.01 in the red (660 nm, vegetation) and NIR band (850 nm, water) for other pixels. If this is the case, the visibility is iteratively increased (AOT550 decreased) according to Table 4.1 to reduce the percentage of very low surface reflectance pixels (with $\rho < 0.01$) below 1% of the scene pixels.

4.8 Range of adjacency effect

If adjacent fields have different surface reflecance the amount of reflected photons is different. Therefore, photons reflected from one field may be scattered by air molecules and particles into the sensor's line of sight of the other field. The range of the adjacency effect for satellite observations is typically between 1 km and 2 km [59, 5] (Kaufman in book of ref. [5] pp.336-428). The aerosol contribution depends on the aerosol scattering efficiency and the aerosol scale height (typically 1 - 3 km). Since detailed aerosol information is usually not available, ATCOR uses a simple method weighting the strength of the adjacency effect with the ratio of the diffuse τ_{dif} to direct ground-to-sensor transmittance τ_{dir} [87]. If ρ_1 denotes the pixel surface reflectance and $\bar{\rho}_1$ the large-area (range R = 1 - 2 km) average reflectance before treating the adjacency effect, then the corrected surface reflectance is ρ_2 :

$$\rho_2 = \rho_1 + q\ (\rho_1 - \bar{\rho}_1) \qquad with \qquad q = \frac{\tau_{dif}}{\tau_{dir}} \tag{4.17}$$

The wavelength index is omitted for brevity and this equation is used for satellite sensors. Since the air volume required for scattering is less for aircraft observations, the adjacency range R for airborne

visibility [km]	vis. increment [km]
5	3
8	3
11	3
14	3
17	3
20	3
23	3
26	4
30	5
35	5
40	5
50	10
60	10
70	10
80	20
100	20
120	10
130	max VIS=130 km

Table 4.1: *Visibility iterations (red, NIR bands).*

cases is approximated by the next two equations. The air density $D(z)$ decreases exponentially with height z $[km]$ and the average scale height is 8 km.

$$D(z) = D(z = 0)\ exp(-z/8) \tag{4.18}$$

The adjacency effect (scattering efficiency) is proportional to the air density. So using eq. 4.18 twice for the aircraft altitude z_1 and the ground elevation $z_2 < z_1$ we obtain the range $R = R(z_1, z_2)$ by considering the air volume between z_1 and z_2 :

$$\begin{aligned} R(z_1) = R_{satellite}\ \{1\ -\ D(z_1, 0)/D(0)\} &= R_{satellite}\ \{1\ -\ exp(-z_1/8)\} \\ R(z_2) = R_{satellite}\ \{1\ -\ D(z_2, 0)/D(0)\} &= R_{satellite}\ \{1\ -\ exp(-z_2/8)\} \\ R(z_1, z_2) &= R(z_1)\ -\ R(z_2) \end{aligned} \tag{4.19}$$

And $R_{satellite}$ is typically between 1 - 2 km.

Chapter 5

Water Vapor Retrieval

The water vapor retrieval over land is based on the atmospherically precorrected differential absorption (APDA) method [115]. It uses simplified radiative transfer equations and combines a partial atmospheric correction with a differential absorption technique. The atmospheric path radiance is iteratively calculated during the retrieval of water vapor, improving results over low albedo surfaces. The error of the derived water vapor column is typically in the range 5% to 10% [74].

The minimum requirement is one reference band in an atmospheric window region (not influenced by water vapor) and one measurement band in an absorption region. If more bands in window and absorption regions are available the retrieval accuracy is increased. For water bodies the average water vapor over land is taken, since the APDA method needs medium-to-high reflectance surfaces in the NIR.

Three absorption regions are supported: around 820 nm, 940 nm, and 1130 nm. Suitable window regions are:

- for 820 nm: left shoulder 780 - 800 nm, right shoulder 840 - 860 nm.
- for 940 nm: left shoulder 860 - 890 nm, right shoulder 1010 - 1040 nm.
- for 1130 nm: left shoulder 1060 - 1080 nm, right shoulder 1220 - 1250 nm.

In case of three water vapor channels (left shoulder, absorption, right shoulder) the APDA radiance ratio is:

$$R_{APDA}(\rho, u) = \frac{L_2(\rho_2, u) - L_{2,p}(u)}{w_1(L_1(\rho_1) - L_{1,p}) + w_3(L_3(\rho_3) - L_{3,p})} \tag{5.1}$$

where the index i=1 and i=3 indicates window channels (e.g. in the 850-890 nm region and 1010-1050 nm region), respectively. Index i=2 indicates a channel in the absorption region (e.g., 910-950 nm). L_i and $L_{i,p}$ are the total at-sensor radiance (corrected to earth-sun distance d=1 [Astronomical Unit]) and path radiance, respectively. The path radiance is taken from the LUT (calculated for d=1). For brevity, the dependence on solar zenith angle, view angle, and DEM height is not included in eq. 5.1. The symbol u indicates the water vapor column. The weight factors are determined from

$$w_1 = (\lambda_3 - \lambda_2)/(\lambda_3 - \lambda_1) \qquad and \qquad w_3 = (\lambda_2 - \lambda_1)/(\lambda_3 - \lambda_1) \tag{5.2}$$

In case of more than three channels, a linear regression equation is used.

The function R_{APDA} is sensitive for low reflectance areas (e.g. water, shadow), because then the numerator and denominator will be close to zero ($L_i \approx L_{i,p}$). The accuracy of the method is limited to about 5% - 10% by the assumption of a linear trend of the surface reflectance in the interval (λ_1, λ_3). Spectrum fitting techniques [33, 108, 136] can achieve better results at the expense of much higher execution times.

Eq. 5.1 can be accurately approximated by a 3-parameter function based on 4 - 6 water vapor grid points:

$$R_{APDA}(u) = a_0 \; exp \; (-a_1 \; u^{a_2}) \tag{5.3}$$

The fit coefficients are calculated iteratively starting with $a_0 = 1, a_1 = 0.01, a_2 = 0.5$. Solving for *'u'* yields:

$$u = \left(\frac{ln(R_{APDA}/a_0)}{-a_1} \right)^{1/a_2} \tag{5.4}$$

The equations (5.1, 5.3, 5.4) are iterated twice starting with u=1.0 cm, calculating R_{APDA}, and updating u, $L_{i,p}(u)$. A two-parameter function can also be used, if the keyword 'two' in the function wv_retrieval_apda2_constvis is set:

$$R_{APDA}(u) = a_0 \; exp \; (-a_1 \; u^{1/2}) \tag{5.5}$$

The default is the 3-parameter version.

5.1 APDA water vapor versions

Two different versions of the APDA method are implemented (parameter '*iwv_model*' in the input parameter file "*.inn") :

- A version restricted to one of the three absorption regions (820, 940, 1130 nm). This versíon is termed 'APDA with regression', because is can handle more than two window channels (on the left and right shoulder) and several absorption (measurement) bands. Then the term L_2 in eq. 5.1 is replaced by $\bar{L}_m$, the mean radiance of all measurement channels, and the denominator of eq. 5.1 is replaced by the linear regression line through the window (reference) channel radiances [115].

- Another version termed 'APDA without regression'. If several left shoulder window channels are specified, then the longest wavelength channel is selected. Similarly, if several right shoulder window channels are specified, then the shortest wavelength channel is taken. If the number 'n' of selected absorption bands is greater than one, then water vapor maps u_i for all 'n' absorption bands are calculated. Finally, the the water vapor map $u_j = min\,(STDDEV(u_i))$ with the smallest standard deviation is selected.
  Additionally, this version allows the joint evaluation of the 940 nm and 1130 nm absorption regions, both with the criterion of the smallest standard deviation. As the final step the average is taken, i.e., $u = 0.5 \; * \; (\; u(940) + u(1130) \;)$, where $u(940)$, $u(1130)$ are the maps with the minimum standard deviation in the 940 nm and 1130 nm spectrum.

  In this version the APDA ratio is calculated as

$$R_{APDA}(u) = exp \; (-a_0 + a_1 \; u^{1/2}) \tag{5.6}$$

where the parameters a_0, a_1 are computed with an exponential fit of eq. 5.1 using the available 4 to 6 water vapor grid points. The water vapor column is then obtained from:

$$u = \left(\frac{a_0 + lnR_{APDA}}{a_1} \right)^2 \tag{5.7}$$

The water vapor map calculated with regression is usually is more accurate, because the regression reduces sensor noise and may partially compensate calibration problems. However, the retrieved surface reflectance spectrum will still retain any channel calibration problems.

Chapter 6

Surface Reflectance Retrieval

Generally, a remotely measured surface signature depends on the illumination and observation geometry. The angular behavior of the surface reflectance is characterized by the BRDF (Bidirectional Reflectance Distribution Function). Integration over the corresponding small finite incidence and observation angles defines the biconical reflectance factor, an intrinsic surface property [82, 114].

Since remote measurements of the earth's surface are conducted under hemispherical illumination conditions (diffuse hemispherical radiation combined with a directional solar irradiance), the most appropriate definition for a retrieved reflectance quantity is the hemispherical directional reflectance factor (HDRF: hemispherical incident solar illumination, directional measurement of surface leaving radiation). Here, the nomenclature of [114] is employed, while [82] restricts the usage of HDRF to an isotropic hemispherical radiation field. Although the HDRF is theoretically defined for an infinitesimal solid angle, it can also be used as an accurate approximation for measurements with a finite angle (the HCRF, hemispherical conical reflectance factor), because of the very small instantaneous field-of-view (FOV) of the instrument.
For a perfectly isotropic (Lambertian) 100% reflecting surface, the terms HDRF, HCRF, and biconical reflectance factor (BCRF: directional conical incident light source, directional conical measurement) are equivalent, and $HDRF = HCRF = BCRF = BRDF \cdot \pi$, see reference [114] for a principal sketch of the different reflectance quantities.

The objective of atmospheric correction is to derive accurate surface reflectance spectra from the measured radiance spectra. Some application fields (e.g. spectral analysis and comparison with albedo library spectra, spectral unmixing methods, spectral indices) use this information without consideration of the observation angle. In these cases, the bi-hemispherical reflectance (or spectral albedo) would be the quantity of interest, as it is unbiased by illumination and observation angles.

For other applications (e.g. ground truth measurements, library spectra with field reflectance measurements, data analysis by model inversion) the directionality of the observation is included in the measurement (and should be retained for the comparison with the satellite retrieved reflectance), or it has to be taken into account in the model, and then the HDRF type of information is preferred.

Optical instruments for remote sensing provide accurate measurements of the the top-of-atmosphere (TOA) radiance (satellite platforms) or at-sensor radiance (airborne platforms). Using the inversion modeling technique and a radiative transfer code, this information is converted into HDRF, usually termed *"surface reflectance"* or *"BOA reflectance" (Bottom-of-Atmosphere).*

Before going into details, a brief overview of the main processing steps during atmospheric correction is described in the next two flow charts. Figure 6.1 contains a compact summary of the main processing elements: after reading the sensor-specific LUTs a masking and preclassification is conducted to obtain land, water, haze, cloud, and shadow areas. Then an optional haze or cirrus removal is conducted followed by an optional shadow removal. The next step calculates the visibility or aerosol optical thickness map using the dense dark vegetation (DDV) method. This is followed by an update of the aerosol model (path radiance behavior in the blue to red bands) if a blue band exists and the update option ($ratio\_blu\_red > 0$) is enabled. Otherwise the selected aerosol model is not changed. After calculation of the water vapor map the iterative surface reflectance retrieval is conducted accounting for adjacency and spherical albedo effects. After atmospheric correction, a spectral polishing (for hyperspectral instruments) and BRDF correction might be performed.

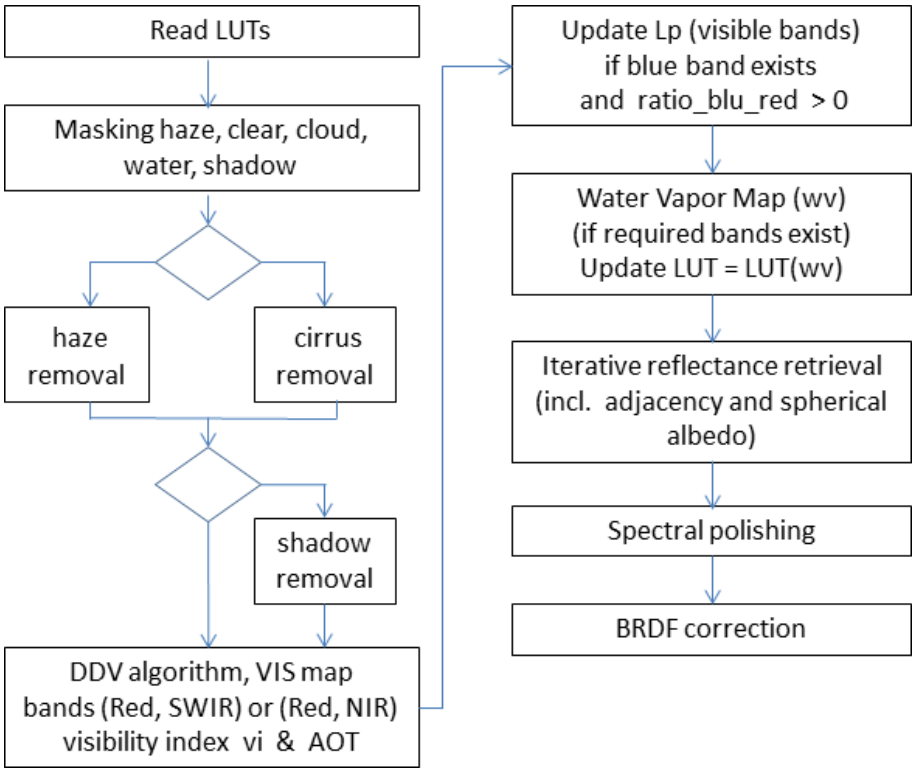

Figure 6.1: *Main processing steps during atmospheric correction.*

The visibility/ AOT(550 nm) retrieval flow chart describes the case with a SWIR band at 2.2 μm. It starts with a low reflectance threshold T1=0.05 and performs the masking in this SWIR band to obtain the darkest pixels, excluding water. If the number of reference pixels is less than 2% of the scene pixels then the threshold T1 is increased until threshold T2 = 0.12 is reached. If not enough reference pixels are found then a constant VIS=23 km is used otherwise the visibility for each reference pixel is determined as the intersection of modeled and measured radiance in the red channel.

Then the red and NIR channels are checked concerning very low surface reflectance (< 0.01) pixels (mainly water, shadow). If the percentage of these pixels is higher than 1% of the scene pixels, then the visibility is iteratively increased up to 120 km, and these 'very dark' areas are stored in a mask containing the respective visibility index.

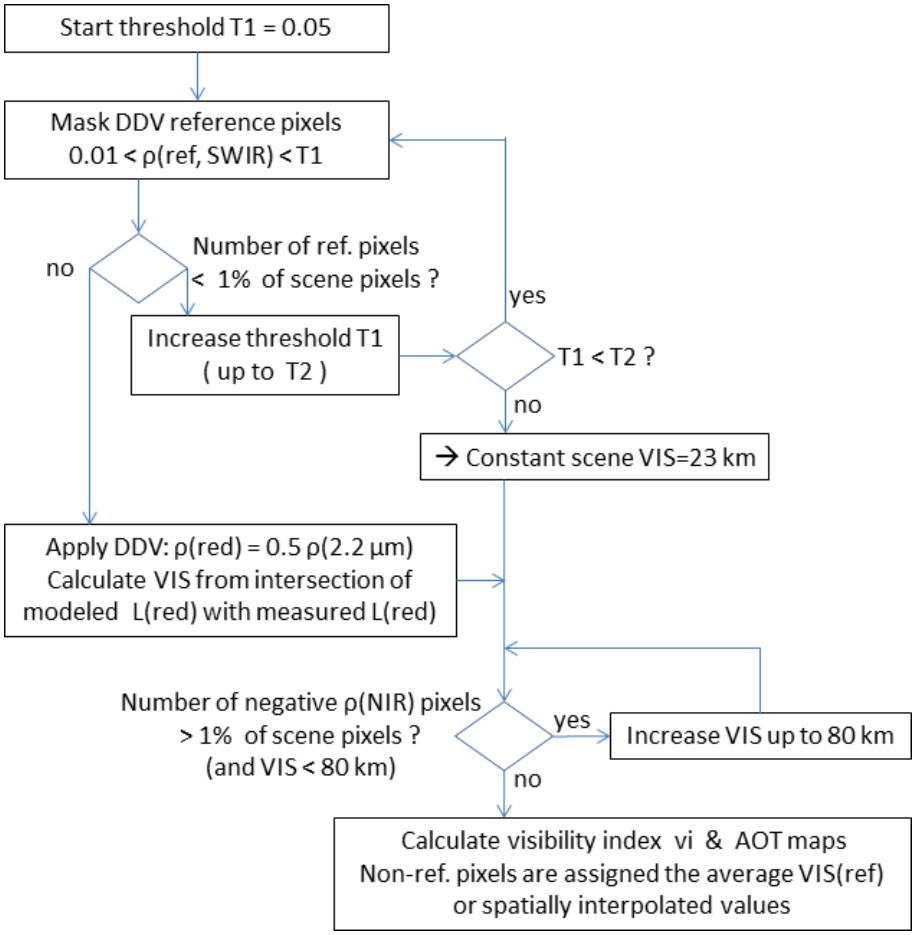

Figure 6.2: *Visibility / AOT retrieval using dark reference pixels.*

The visibility index 'vi' is closely related to the total optical thickness δ at 550 nm, $\delta = 0.185 + 0.006 * vi$. It is used for a fast indexing of arrays depending on visibility to avoid time-consuming interpolation.
Since reference pixels might be close to 'very dark' areas (in most cases from the NIR band), the visibility index of the reference pixels vi_{ref} is updated to obtain a smooth visibility/AOT transition

$$vi_{ref} = vi_{ref} + 0.5 \cdot (vi_{dark} - vi_{ref}) \tag{6.1}$$

where vi_{dark} is the average visibility index from the 'very dark' areas (red, NIR bands). Of course, equation 6.1 is only applied to reference pixels with $vi_{ref} > vi_{dark}$. A visibility index map is created inserting the visibility index of the reference pixels as well as the visibility index of the red and NIR band 'very dark' areas. The non-reference (and non 'very dark' area) pixels are assigned the average of the reference pixel visibility index. Alternatively, triangular interpolation can be applied. The final step is a spatial low pass filter (3 km × 3 km) of the visibility index and AOT(550nm) maps to smooth small-scale fluctuations and noise.

If the aerosol type (rural, urban, maritime, desert) is not fixed by the user, i.e., if the 'auto' aerosol is selected in the '*.inn' file, then the flow chart is executed for these four types, and the type

closest to the scene-estimated type is used.

We distinguish two cases for the surface reflectance retrieval: a flat terrain, specified by its average elevation, and a rugged terrain, where a DEM (Digital Elevation Model) is needed. Although the flat terrain could be handled as a special case of a DEM, we implemented separate modules, because the flat terrain case runs 3 to 4 times faster.

6.1 Flat terrain

Figure 6.3 contains a schematic sketch of the main radiation components in flat terrain.

- component 1: scattered radiance, path radiance,
- component 2: radiation reflected from pixel under consideration,
- component 3: radiation reflected from the neighborhood and scattered into the viewing direction ("adjacency" effect).

Only component 2 contains information on the surface properties of the pixel, the other components have to be removed during the atmospheric correction. As detailed in [98] the adjacency radiation L_3 consists of two components (atmospheric backscattering and volume scattering) which are combined into one component in Fig. 6.3.

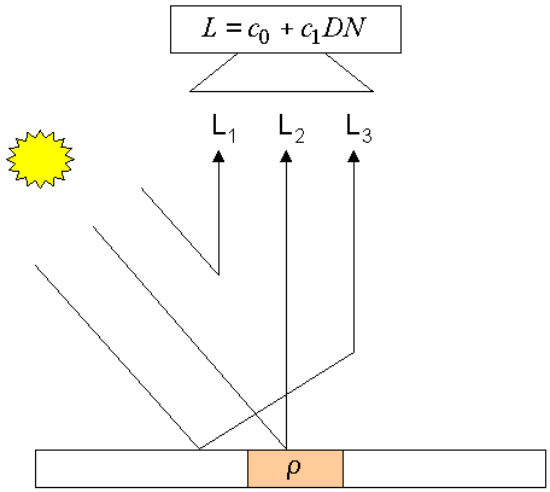

Figure 6.3: *Schematic sketch of solar radiation components in flat terrain.*

The radiometric calibration assigns to each digital number (DN) the corresponding at-sensor radiance L

$$L(k) = c_0(k) + c_1(k)DN(k) \tag{6.2}$$

where k indicates the channel number, and c_0 , c_1 are the calibration coefficients (offset and slope). For sensors with adjustable gain settings the equation is

$$L(k) = c_0(k) + c_1(k)DN(k)/g(k) \tag{6.3}$$

where $g(k)$ is the gain setting in channel k. The atmospheric correction has to be performed iteratively, since the surface reflectance and large-scale (1- 2 km neighborhood) background reflectance are not known. So three steps are employed in the ground reflectance calculation:

Step 1: The influence of the neighborhood (adjacency effect) is neglected and the surface reflectance is obtained from

$$\rho^{(1)} = \frac{\pi[d^2(c_0 + c_1 DN) - L_p]}{\tau_v E_g(\rho_r = 0.15)} \tag{6.4}$$

where the spectral band index is omitted for clarity. The path radiance L_p, transmittance τ_v, and global flux E_g depend on the view and solar geometry as well as on aerosol and water vapor content. These quantities were already provided during the visibility / water vapor retrievals. The factor d^2 takes into account the sun-to-earth distance (d is in astronomical units) since the LUTs with path radiance and global flux are calculated for d=1 in ATCOR.

Step 2: The second step calculates the average surface reflectance in a large neigborhood of each pixel (default range R = 1 km)

$$\bar{\rho} = \frac{1}{N^2} \sum_{i,j=1}^{N} \rho_{i,j}^{(1)} \tag{6.5}$$

where N corresponds to the number of pixels for the selected range R of the adjacency effect [98]. The exact choice of R is not critical since the adjacency influence is a second-order effect. Instead of the range-independent weighting in eq. (6.5), a range-dependent function can be selected with an exponential decrease of the weighting coefficients. The range-dependent case requires more execution time, of course. Except for special geometries, the difference between both approaches is small, because the average reflectance in a large neighborhood usually does not vary much and the influence is a second-order effect.

$$\rho^{(2)}(x,y) = \rho^{(1)}(x,y) + q\{\rho^{(1)} - \bar{\rho}(x,y)\} \tag{6.6}$$

The function q indicates the strength of the adjacency effect. It is the ratio of the diffuse to direct ground-to-sensor transmittance. The range-dependent version of eq. (6.6) is:

$$\rho^{(2)}(x,y) = \rho^{(1)}(x,y) + q\{\rho^{(1)}(x,y) - \int_0^R \rho^{(1)}(r) A(r) exp(-r/r_s) dr\} \tag{6.7}$$

Here, R is the range where the intensity of the adjacency effect has dropped to the 10% level (i.e. r=R=2.3x r_s, where r_s is a scale range, typically r_s=0.5 km, R=1 km), ρ(r) is the reflectance at range r from the (x,y) position and A(r) is the area of a circular zone from r to r+dr. Now we approximate the circular regions by square regions to obtain the discrete version of eq. (6.7) with exponentially decreasing weighting coefficients w_i [92]:

$$\rho^{(2)}(x,y) = \rho^{(1)}(x,y) + q\{\rho^{(1)}(x,y) - \sum_{i=1}^{n_R} \bar{\rho}_i w_i\} \tag{6.8}$$

$$w_i = \frac{1}{\sum_{i=1}^{n_R} W_i} W_i \qquad and \qquad W_i = \int_{r_{i-1}}^{r_i} A(r) exp(-r) dr \approx \int_{r_{i-1}}^{r_i} (2r)^2 exp(-r) dr \tag{6.9}$$

ATCOR supports up to n_R=5 regions. Since the sequence of moving digital low pass filters works with square filters of size $2r_i$ * $2r_i$, the area A(r) is approximated as the corresponding square region $A(r) = (2r)^2$.

Step 3: it includes the spherical albedo effect on the global flux that was initially calculated with the reference background reflectance $\rho_r = 0.15$ and is finally adapted to the scene-dependent value $\bar{\rho}$ by correcting with the difference $\bar{\rho} - \rho_r$:

$$\rho^{(3)}(x, y) = \rho^{(2)}(x, y)[1 - (\bar{\rho}(x, y) - \rho_r)s] \tag{6.10}$$

6.2 Rugged terrain

This section presents the equations for the retrieval of surface reflectance in rugged terrain, using a the digital elevation model (DEM) to specify the pixel-dependent elevation. The flat terrain case, where the DEM has the same elevation everywhere, is more efficiently handled in the 'flat terrain' module, but can also be treated here. For a flat terrain (and clear sky conditions) the hemispherical radiation field is nearly constant. However, in mountainous terrain, the incident radiation strongly varies depending on topography.
This chapter describes the radiative transfer equations assuming a Lambertian (isotropic) reflectance law. However, there are large variations of the local solar incidence angle in rugged terrain and bidirectional reflectance effects are much stronger than in a flat terrain and have to be taken into account. Since the BRDF is not known for high spatial resolution imagery, we have to use empirical methods to correct for these effects. The topographic correction methods available in ATCOR are described in chapter 7 and the selected topographic compensation method is always combined with the atmospheric correction.
For narrow field-of-view (FOV) instruments the solar and view geometry can be treated as constant. Typical representatives are Landsat, Rapid Eye, SPOT, and Worldview. For medium and wide FOV instruments the variation of the view and solar geometry within a scene have to be taken into account. Typical representatives are Sentinel-2, and Sentinel-3. For Sentinel-2 imagery, the scene is automatically partitioned into small cells corresponding to view/sun angles changes smaller than 2°.

Figure 6.4 shows a sketch of the four radiation components in a rugged terrain.

- path radiance L_p, scattered radiation without ground contact,
- ground reflected radiance L_g (direct irradiance and diffuse solar flux),
- adjacency radiance L_a, scattered from the large-scale neighborhood,
- reflected terrain radiance L_t from opposite mountains. This component needs the terrain view factor $V_t = 1 - V_{sky}$, where the sky view factor V_{sky} is either calculated with a prior run of a ray tracing program [23] or a simpler approximation (see equation 6.14). The sky view factor for a flat infinite surface is normalized to 1.

The first processing step is the conversion of the digital number (DN) image into TOA radiance, using the meta data (radiometric calibration offset $c_0(i)$ and gain $c_1(i)$, channel i, acquisition date, solar and view geometry) provided with each scene.

$$L_{TOA}(i) = c_0(i) \; + \; c_1(i) \; DN(i) \tag{6.11}$$

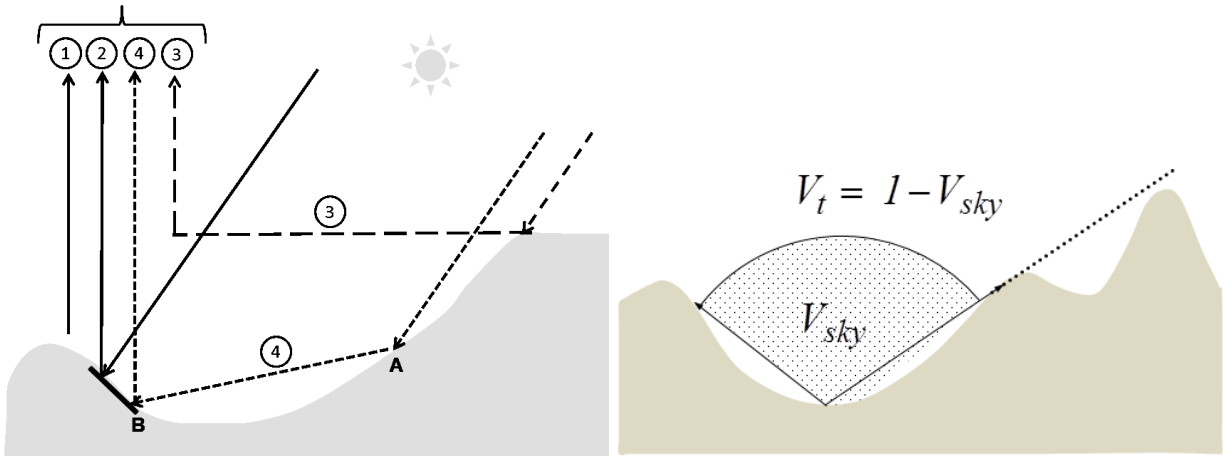

Figure 6.4: *Radiation components in rugged terrain, sky view factor.*

In case of Sentinel-2 scenes, the level-1 data is provided as scaled TOA reflectance, which is also converted into TOA radiance. The second step is the retrieval of atmospheric parameters (aerosol optical thickness at 550nm, water vapor column) using a radiative transfer model. The last step is the iterative retrieval of the surface reflectance from the TOA (or at-sensor) radiance.

Atmospheric / topographic correction consists of two algorithms: a physical algorithm to treat the radiative transfer in rugged terrain with the simplifying assumption of a Lambertian reflectance law, and an empirical algorithm to handle BRDF effects. Since there are several options for the empirical method, these are presented in a separate chapter (chapter 7).

The measured at-sensor radiance consists of the four components sketched in Figure 6.4, i.e.,

$$L_{TOA}(x, y, z, \lambda) = L_p(x, y, z, \lambda) + L_g(x, y, z, \lambda) + L_a(x, y, z, \lambda) + L_t(x, y, z, \lambda) \tag{6.12}$$

Here, x, y, z denote the planar and height coordinates of the scene. Other dependencies (solar and sensor view geometry, atmospheric parameters, channel index) have been omitted for brevity. Omitting the wavelength and spatial coordinates for brevity the terrain radiance component is:

$$L_t = T\ E_t^{(1)}\ V_t\ \rho_t/\pi \tag{6.13}$$

where T is the total (direct plus diffuse) ground-to-sensor transmittance, $E_t^{(1)}$ the global terrain flux for a terrain reflectance $\rho_t = 0.1$, and V_t the terrain-view factor. The unknown ρ_t is initialized with 0.1, but will be iterated. To handle the difficult terrain influence, the terrain-view factor V_t has to be computed, which represents a map of all pixels that can contribute to the reflected terrain radiation on an individual pixel. It is the complement of the sky-view factor V_s, i.e., $V_t = 1 - V_s$ (if V_s for the hemisphere is normalized to 1), and V_s can be computed with the fast ray tracing of the Dozier algorithm [26].

If the sky-view file is not available, a simplified sky view factor is automatically computed during the reflectance retrieval, based on the local DEM slope angle θ_n (trigonometric approach):

$$V_{sky}(x, y) = cos^2(\theta_n(x, y)/2) = \frac{1\ +\ cos\theta_n(x, y)}{2} \tag{6.14}$$

If $\theta_s, \theta_n, \phi_s, \phi_n$ denote solar zenith angle, terrain slope, solar azimuth and topographic azimuth, respectively, the local solar illumination angle β can be obtained from the DEM slope and aspect angles and the solar geometry:

$$cos\beta(x,y) = cos\theta_s \; cos\theta_n(x,y) + sin\theta_s \; sin\theta_n(x,y) \; cos\{\phi_s - \phi_n(x,y)\} \tag{6.15}$$

The ground reflectance ρ_g corresponding to L_g is calculated depending on the direct and diffuse pixel irradiance, neglecting the neighborhood influence,

$$\rho_g = \frac{\pi \; [L_{TOA} - L_p]}{T \; \left[b \; E_s cos\beta + E_d^*\right]} \tag{6.16}$$

where $b = 0$ for a shadow pixel, else $b = 1$, E_s is the direct solar beam irradiance (at ground), and E_d^* the total diffuse flux on a sloped surface [45]:

$$E_d^* = E_d \; [b\tau_s \; cos\beta / cos\theta_s + \{1 - b\tau_s\} V_{sky}] \tag{6.17}$$

E_d is the diffuse solar flux on a horizontal plane, and τ_s the sun-to-ground beam (direct) transmittance. The first part of eq. 6.17 represents the anisotropic circumsolar (near solar direction) radiation, the second part the isotropic sky radiation.

Unlike the TOA radiance / reflectance equations (eq. 7.1, 7.2) for the cosine and Minnaert cases, the ground reflectance of this equation does not tend to infinity as $cos\beta$ tends to zero, because the diffuse flux E_d^* is always greater than zero. So this is an advantage, but does not imply that the results are always physically correct, because of the difficulty of calculating the diffuse and terrain flux in a complex environment.
Equation (6.16) is then iterated to include the first-order correction with the terrain influence (and index 'g' is dropped)

$$\rho^{(1)} = \frac{\pi \; [L_{TOA} - L_p]}{T \; \left[b \; E_s cos\beta + E_d^* + E_t^{(1)}\right]} \tag{6.18}$$

Next the average reflectance $\bar{\rho}^{(1)}$ is calculated with a moving low-pass window of size $2 \cdot R_1 \times 2 \cdot R_1$, with the typical adjacency range $R_1 = 1$ - 2 km. Then the multiple terrain reflection effects can be corrected as proposed by reference [126] with an additional approximation, i.e., the neglect of the small transmission loss in the short line-of-sight distance from the slope pixel to the target pixel, see distance A-B in Fig. 6.4,

$$E_t^{(2)} = E_g \; \frac{\bar{\rho}^{(1)} \; V_t}{1 \; - \; \bar{\rho}^{(1)} \; < V_t >} \tag{6.19}$$

Here, E_g is the global (direct plus diffuse) flux on the ground. The term $< V_t >$ indicates the averaging of V_t with a moving low-pass window of size $2 \cdot R_1 \times 2 \cdot R_1$. Then equation (6.18) of the surface reflectance $\rho^{(1)}$ is iterated again with $E_t^{(2)}$ from eq. (6.19):

$$\rho^{(2)} = \frac{\pi \; [L_{TOA} - L_p]}{T \; \left[b \; E_s cos\beta + E_d^* + E_t^{(2)}\right]} \tag{6.20}$$

The adjacency effect is accounted for by computing the average reflectance $\bar{\rho}^{(2)}(x,y)$ with a moving low-pass window of size $2 \cdot R_1 \times 2 \cdot R_1$.

Then the ground reflectance $\rho^{(2)}$ is updated with the weighted difference of the area-average $\bar{\rho}^{(2)}$ and $\rho^{(2)}$ using the weight factor q = ratio of diffuse to direct ground-sensor transmittance [92],

$$\rho^{(3)}(x,y) = \rho^{(2)}(x,y) + q(x,y) \left[\rho^{(2)}(x,y) - \bar{\rho}^{(2)}(x,y)\right] \tag{6.21}$$

Instead of the range-independent q weighting, a range-dependent function can be selected with an exponential decrease of the weighting coefficients [92]. The range-dependent case requires more execution time, of course. Except for special geometries, the difference between both approaches is small, because the average reflectance in a large neighborhood usually does not vary much and the influence is a second-order effect.

The last step includes the spherical albedo effect on the global flux that was calculated with the reference reflectance $\rho_r = 0.15$ in the radiative transfer code. The spherical albedo describes the amount of atmospheric backscatter to the earth, and the corresponding function s is one of the radiative transfer functions stored in the atmospheric LUTs. The effect is included in the next equation:

$$\rho(x,y) = \rho^{(3)}(x,y) \; [1 - (\bar{\rho}^{(3)}(x,y) - \rho_r) \; s] \tag{6.22}$$

where the index 'p1' indicates the result of "Part 1" of the algorithm. This result is merged with the selected empirical topographic compensation method ("Part 2") of chapter 7.

The radiative transfer functions (path radiance, transmittance, fluxes, etc) depend on solar geometry, ground elevation, aerosol content, and water vapor column. This dependence is not included in the notation for brevity. However, an important topic is the accurate calculation of the RT functions from the available 4 - 6 water vapor grid points. The approach taken here is to approximate each RT function with a fit of 3 water vapor grid points covering the range of water vapor content of the scene. A fit with the appropriate water vapor sub-interval (e.g. 2 - 4 cm) is more accurate than a fit over the whole water vapor range (0.4 - 5 cm), see [99]. The fit function is

$$y = exp \; (a + b * u^{1/2} \;) \tag{6.23}$$

where y is the RT function, u is the water vapor content, and a, b are regression coefficients obtained for the respective sub-interval with three water vapor grid points.

6.3 Spectral solar flux, reflected surface radiance

For some applications the spectral solar fluxes on the ground are required. They can be obtained in ATCOR by setting the parameter *irrad0 = 1* in the '*.inn' file or using the graphical user interface. The fluxes depend on solar geometry, terrain elevation, topography, and atmospheric conditions. All fluxes and the surface reflected radiance of this section are evaluated for the current earth-sun distance. For a flat terrain, ATCOR provides spectra of the direct, diffuse, and global flux for the selected visibility / water vapor. In case of variable visibility / water vapor the spectra are calculated for the average scene visibility / water vapor. The direct flux is just the beam irradiance on the ground times the cosine of the local solar zenith angle. The diffuse flux spectrum E_{dif} is evaluated for a surface reflectance of $\rho = 0$, and the global flux for $\rho = 0.15$, i.e., $E_g = (E_{dir} + E_{dif}(0))/(1 - s \cdot 0.15)$, where s is the spherical albedo. The spectral band index is omitted for brevity. For a flat terrain these fluxes are provided in the directory of the input file (e.g. *'scene.bsq'*):

- the direct spectral flux on the ground: *'scene_edir.dat'*
- the diffuse spectral flux on the ground: *'scene_edif.dat'* for surface reflectance $\rho = 0$.
- the global spectral flux on the ground: *'scene_eglo.dat'* for a typical average surface reflectance $\rho = 0.15$.

These spectra will already give a realistic description for a flat terrain, but they lack the dependence on the spectral reflectance variations in the scene. Therefore, an image of the global flux is also provided that accounts for the spatial reflectance and visibility / water vapor patterns (VIS, named *'scene_eglobal.bsq'*:)

$$E_g(x,y) = \frac{E_{dir}(VIS(x,y)) + E_{dif}(\rho = 0, VIS(x,y))}{1 - s(x,y)\ \bar{\rho}(x,y)} \tag{6.24}$$

Here, $\bar{\rho}$ indicates a spatial averaging with a filter size corresponding to the specified adjacency range. The unit of the global flux is $mWcm^{-2}\mu m^{-1}$ and it is stored as float data (32 bits/pixel). Therefore, its file size will be twice or four times the size of the input scene if the scene is encoded as 16bit/pixel and 8bits/pixel, respectively.

For a rugged terrain, images of the direct and diffuse fluxes will be calculated using the available DEM information on height (z), slope and aspect (i.e. local solar illumination angle β), and atmospheric conditions (visibility / water vapor VIS). The direct flux on the ground is :

$$E_{dir}(x,y) = b(x,y)\ E_0\ T_{sun}(VIS(x,y,z))\ cos\beta(x,y) \tag{6.25}$$

where E_0, T_{sun} are extraterrestrial solar irradiance and sun-to-ground transmittance, respectively, and
b is the topographic shadow mask (0=shadow, 1=sunlit pixel).
The diffuse flux in mountainous terrain accounts for the adjacency effect and multiple reflection effects from the surrounding topography. Using the terrain view factor V_t from the last section and the effective terrain reflectance $\rho_t = V_t(x,y)\ \bar{\rho}(x,y)$ and $\bar{\rho}_t = \bar{V}_t(x,y)\ \bar{\rho}(x,y)$ the diffuse flux is approximated as:

$$\begin{aligned} E_{dif}(x,y) \quad = \quad & E_{dif,flat}\ \{b\ T_{sun}(x,y,z)\ cos\beta/cos\theta_s + \ [1 - b(x,y)\ T_{sun}(x,y,z)]\ V_{sky}(x,y)\} \\ & + \{E_{dir,flat}(x,y,z)\ +\ E_{dif,flat}(x,y,z)\}\ \rho_t(x,y)\ /\ (1 - \bar{\rho}_t(x,y)) \end{aligned} \tag{6.26}$$

The first line describes the anisotropic and isotropic components of the diffuse flux, the second line accounts for multiple terrain reflection effects.

Related quantities to the global spectral solar flux on the ground are the wavelength-integrated global flux and the absorbed solar flux (Wm^{-2}). These play a role in the surface energy balance and they are available as part of the value added channels, see chapter 14.3.

Surface reflected radiance

The ground reflected (or ground leaving) radiance per band can be obtained in addition to the spectral solar fluxes by setting the parameter irrad0=2 in the *'*.inn'* file. It is calculated corresponding to the surface reflectance cube $\rho(x,y)$, named *'scene_surfrad.bsq'*. For a flat terrain it is:

$$L(surf,x,y) = E(global)\ \rho(x,y)\ /\ \pi \tag{6.27}$$

In case of a mountainous terrrain the direct and diffuse reflected radiation maps from the equations 6.25 and 6.26 are used:

$$L(surf, dir, x, y) = (E_{dir} \ + \ E_{dif})\rho(x, y) \ / \ \pi \tag{6.28}$$

Again, the same output file name is used (*'scene_surfrad.bsq'*).

6.4 Spectral Smile

Imaging systems can employ different techniques to record a scene: the whiskbroom design uses a rotating or oscillating mirror to collect an image line in across-track direction (with one or a few detector elements per spectral band). The forward direction is provided by the motion of the platform. Secondly, a pushbroom linear array can perform the same task without moving optical elements, but the number of array lines (each recording a certain spectral channel) in the focal plane is limited. The third imaging technique employs an area detector array where one direction collects the spatial information (across-track) and the orthogonal direction covers the spectral dimension. The advantage of the last two techniques is a longer pixel dwell time and a potentially improved signal-to-noise ratio (SNR). The drawback is a substantial increase in the spectral and radiometric characterization, i.e., a change of the channel center wavelength across the columns of the array (spectral "smile"), spatial misregistration ("keystone"), and detector non-uniformity problems [78], [27], [101]. Typical representatives of the whiskbroom type are Landsat TM/ ETM, HyMap, AVIRIS, and Daedalus. These instruments almost show no spectral smile, i.e., the channel center position and bandwidth do not depend on column pixel location. Spaceborne hyperspectral instruments showing the "smile" effect are Hyperion and CHRIS/Proba, airborne instruments are for example CASI-1500 and APEX.

Compared to non-smile sensors the following additional information has to be provided to account for spectral smile:

- The sensor definition file, e.g., *"sensor_*.dat"*, needs one more line (see Table 6.2 containing the parameters *ismile* (=1 if smile sensor, otherwise 0) and *filter_type* (a number between 1 and 9 for the type of channel filter function) compare Table 6.1. The filter types 1 to 8 are analytical functions, filter type 9 is reserved for arbitrary user-defined channel filter functions (the *'band*.rsp'* files). Center wavelength and bandwidth for each channel are defined in the wavelength file (*'*.wvl'*) pertaining to the center pixel=column of the detector array. The Butterworth spectral channel response function of order m (Table 6.1) is defined as:

$$R(\lambda) = \frac{1}{1 + \left(\frac{\lambda - \lambda_c}{FWHM}\right)^{2m}} \tag{6.29}$$

  where λ_c is the channel center wavelength, and $FWHM$ is the bandwidth (full width at half max).

- For each spectral channel j the channel center wavelength $\lambda_c(j)$ depends on the image column or pixel position x. The absolute value of $\lambda_c(j)$ is specified in the wavelength file used to generate the spectral channel response functions, and it is also included in the sensor-specific solar irradiance file (e.g., *"e0_solar_enmap_mode3.spc"*). If n is the number of image columns,

the change $\Delta(x, j)$ of the center wavelength $\lambda_c(j)$ with the pixel position x can be described as a 4th order polynomial (using the nm unit):

$$\Delta(x, j)[nm] = a_0(j) + a_1(j) \cdot x + a_2(j) \cdot x^2 + a_3(j) \cdot x^3 + a_4(j) \cdot x^4 \tag{6.30}$$

$$\lambda_c(x, j) = \lambda_c(j) + \Delta(x, j) \tag{6.31}$$

The first left-hand image pixel is x=0, the last right-hand image pixel is x=(n-1). The coefficients $a_i(j)$ have to be stored in an ASCII file, corresponding to the band sequence. The first column must contain the wavelength or band number, followed by the five channel-dependent coefficients (beginning with a_0 and ending with a_4), one line per channel. The fixed file name is *smile_poly_ord4.dat* and it has to be located in the corresponding sensor sub-directory. In the ideal case these coefficients should be derived from laboratory measurements. Since an accurate description is only required for channels in atmospheric absorption regions, the 5 coefficients can be set to zero for the remaining regions, but they must be provided for each channel. If all 5 coefficients are set to zero for a certain channel, this channel is processed in the "non-smile" mode which will expedite the processing.

- Optionally, the spectral bandwidth (FWHM) might also depend on the image column. Again, a 4th-order polynomial is used to describe the bandwidth change depending on column position x and channel j :

$$\Delta_1(x, j)[nm] = b_0(j) + b_1(j) \cdot x + b_2(j) \cdot x^2 + b_3(j) \cdot x^3 + b_4(j) \cdot x^4 \tag{6.32}$$

$$FWHM(x, j) = FWHM(j) + \Delta_1(x, j) \tag{6.33}$$

The fixed file name is *smile_poly_ord4_fwhm.dat* and it has to be located in the corresponding sensor sub-directory. It is an ASCII file with 6 columns per channel, the first column is the channel number or wavelength, the remaining columns contain the polynomial coefficients starting with b_0.

function number	function type
1	Butterworth order 1 (slow drop-off)
2	Butterworth order 2 (close to Gauss)
3	Butterworth order 3 (between Gauss/rectangular))
4	Butterworth order 4 (close to rectangular)
5	Gaussian
6	Rectangular
7	Triangular
8	Rectangular (first bands) to triangular (last bands), due to binning
9	ASCII file (table wavelength vs normalized response), per band

Table 6.1: *Spectral response filter types.*

Imagery from smile sensors must be processed in the raw geometry (IGM Image Geometry Map) to preserve the original image columns. During the surface reflectance retrieval the atmospheric /

2.0	512	across-track FOV [degree], pixels per line
1	128	first, last reflective band (0.35-2.55 μm)
0	0	first, last mid IR band (2.6 -7.0 μm)
0	0	first, last thermal band (7.0 -14 μm)
0		no tilt in flight direction
0		required dummy
1	5	1=smile sensor, 5 = Gaussian spectral channel filter

Table 6.2: *Sensor definition file: smile sensor.*

topographic correction is performed on a per column basis, i.e., to each image column its appropriate center wavelength /bandwidth is associated.

The per-column processing typically implies a factor of 8 increase in processing time. The following steps are required for imagery affected by spectral smile:

1. Define the sensor (spectral response file per band *'*.rsp'*, radiometric calibration file *'*.cal'*), using the original set of wavelengths (pre-launch values specified by the data provider), calculate the sensor-specific atmospheric LUTs (using module RESLUT).

2. Specify the smile polynomial coefficients, file 'smile_poly_ord4.dat' from the laboratory, or run the smile detection tool (chapter 6.4.1) to derive the 'smile_poly_ord4.dat'. *Note:* if the instrument consists of two sensors (e.g. VNIR and SWIR) the smile detection tool should be applied separately for VNIR and SWIR, with option 'repeat values', resolution 0.02 nm. Afterwards the two files (VNIR, SWIR) have to be combined manually. Then copy the new file *'smile_poly_ord4.dat'* into the sensor definition directory

3. Run atmospheric correction with the smile option.

4. Run the spectral smile correction by interpolation (chapter 6.4.2).

5. Optionally run the spectral filtering / polishing (chapter 9).

6.4.1 Spectral smile detection

This method uses sharp atmospheric absorption features and Fraunhofer lines for inflight smile (i.e., spectral across-track non-uniformity) detection. The calculation is done by correlation analysis of a number of spectral bands in the vicinity of selected absorption features. The outputs may be used for smile-aware atmospheric correction.

Initially, the smile characterization for each spectrometer channel is derived from laboratory measurements. From such data, the wavelength shift with respect to the center pixel of the detector array can be parametrized using a 4th order polynomial fit. However, in case of instrument changes during the mission, a spectral re-calibration might be necessary from the image data or from onboard calibration facilities using well-defined absorption features. Onboard spectral calibration devices such as interference or rare earth filters would be well suited for this purpose. However, such devices are often not available in sensor systems. Therefore, atmospheric gas absorption features or solar Fraunhofer lines have to be taken as a reference from the imagery itself. The processing steps are:

1. A calibrated image is averaged in along track direction, leading to a signature image of the size of the detector array.
2. The surface reflectance is calculated (atmospheric correction) and smoothed.
3. The spectral bands within the spectral matching range are selected.
4. Spectral shifts with intervals between 0.01-0.05 nm are calculated and applied to the selected spectral band response functions.
5. An appropriate pre-calculated fine-spectral resolution atmospheric LUT is selected which serves for the calculation of at-sensor radiance values for the series of spectrally shifted response functions using the surface reflectance spectrum from step (2).
6. The derived spectral signatures are then correlated to the observed column-averaged signal in the image, such that the best fitting spectral shift $\Delta\lambda_j = \Delta_j$ can be found for each image column j, i.e., the Δ_j with the highest Pearson's correlation coefficient is selected. This is equivalent to minimizing the merit function

$$\chi^2(\Delta_j) = \sum_{\Delta_j=\lambda_k-5nm}^{\lambda_k+5nm} \left[L_I(j,k) - L_R(\lambda_k + \Delta_j, k)\right]^2 , \tag{6.34}$$

   where $L_I(j,k)$ is the average at-sensor radiance of the image for column j and channel k, and $L_R(\lambda_k + \Delta_j, k)$ is the corresponding reference radiance for a wavelength shift Δ_j within a 5 nm interval around λ_k. By using the continuum removed scaled radiances, the stability of the routine is enhanced.
7. A 4th order polynomial is fitted through the calculated spectral points and the respective polynomial parameters of eq. 6.30 are stored.
8. The polynomial parameters are interpolated and optionally extrapolated to all other bands within the same detector or spectrometer unit. Optionally, the polynomial coefficients can be set to zero in atmospheric absorption regions to expedite the processing.

The same approach is used for FWHM detection, with the difference that not the position of the spectral bands is varied, but the FWHM of the spectral bands is scaled in a systematic way. Once the coefficients have been determined, they are converted into the required file format and are placed in the respective sensor folder for a subsequent fully automatic radiometric and atmospheric processing. Fig. 6.5 shows the panel of the smile detection module.

Inputs:

Input file : calibrated ENVI image file. The file should be statistically as uniform as possible in order to get valid averages.

Atmospheric Database File: non-resampled atmospheric database file most appropriate for the selected image; take care of the flight altitude and aerosol model.

Sensor spectral response: First band of sensor spectral response file(s) $*$.rsp. The corresponding pressure definition file (pressure.dat) is selected automatically from the same directory as the $*$.rsp files, if available.

Output smile coefficients: file name of ASCII file which is written and contains the 4th order polynomial coefficients. This file may be copied to the sensor definition as 'smile_poly_ord4.dat' for use as smile definition with a sensor.

Detection resolution: finest spectral resolution used for correlation analysis - results will be resolved by this resolution.

Search range: maximum total spectral range used for smile detection (ie., 20 nm is +- 10 nm search distance). For FWHM detection, it is the maximum factor to be applied. A factor of 2, e.g. means to search between FWHM scaling from 0.5 to 2.

Band range: bands which shall be used for smile detection and for which the coefficients are written to the output file.

Split band: First band of second detector for sensor having more than one detector (starting numbering at 1). NOTE: for imagers with more than two detector it is recommended to derive the smile separately for each detector to avoid artefacts in the transition range.

Visibility: horizontal visibility as of modtran conventions [km]

Solar Zenith: angle measured from zenith to sun

Mean Ground Elevation: Ground altitude in km.

Flight Altitude: in km a.s.l.

Feature wavelength: 15 selectable features used for smile detection. the per-band smile is interpolated from these feature wavelengths.

Interpolation type: interpolation used to expand the feature wavelength results to all spectral bands

Extrapolation type: specifies how the bands outside of the selected features are treated. Repeat: repeats the last value toward the borders. 'to zero': gradually decrease to zero at border of detector.

Actions:

Detect Smile The module will perform the smile detection calculation.

Detect FWHM The FWHM variations are calculated instead of smile variations by the same technique.

Plot Smile Starts a plotting window to check the smile and lets you select suitable features for calibration.

Save Report Saves an informational report about the smile detection.

Outputs:

An ASCII-file which may be used as smile (or FWHM) description file in the respective sensor directory. Note that this file should be named *"smile_poly_ord4.dat"* or *"smile_poly_ord4_fwhm.dat"* in order to be automatically recognized by ATCOR.
As a side output, an IDL save dump (∗.sav) is written in parallel which contains all used parameters and the effectively calculated smile results in array "smileresult(4,ncols,12)". Here the first dimension (4) contains the center wavelength (nm), smile shift (nm), atmospheric transmittance, and correlation coefficient. The second dimension (ncols) refers to the number of image columns, and the last dimension (12) contains results for the 12 feature wavelengths. For example, the center wavelengths for all across-track pixels and the 760 nm feature are stored in smileresult[0,*,2], because this feature is the third one and IDL arrays start with index 0.

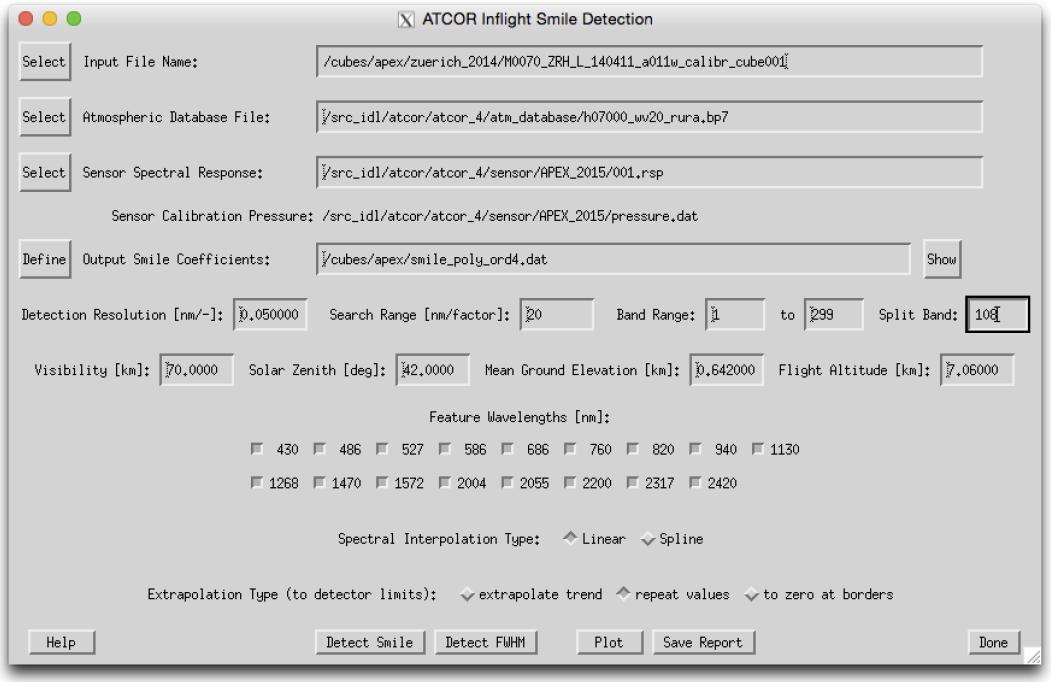

Figure 6.5: *Spectral smile detection*

6.4.2 Spectral smile correction

During atmospheric/topographic compensation the spectral smile is taken into account on a per-column basis, i.e. each image column has a slightly different different center wavelength. A smile correction procedure is needed to calculate the surface reflectance for a common center wavelength for each channel. Since the smile shift between adjacent bands does not vary significantly, a linear interpolation can be applied. If $\lambda_j(i)$ denotes the center wavelength of band i and column j, and $\rho_j(i)$ the surface reflectance of a column j pixel, then the new interpolated reflectance is

$$\rho_j^{(new)}(i, \lambda_{ref}(i)) = \rho_j(i) + \frac{(\lambda_{ref}(i) - \lambda_j(i))\ \ (\rho_j(i+1) - \rho_j(i-1))}{\lambda_j(i+1) - \lambda_j(i-1)} \tag{6.35}$$

where $\lambda_{ref}(i)$ is the user-defined reference center wavelength for band i. There are three options for the reference wavelength grid:

1. the wavelength corresponding to the center of the detector array,
2. the average wavelength over all detector columns (per band),
3. the nominal wavelength specified in the (ENVI) header of the reflectance cube.

This tool is available in the interactive mode (ATCOR's main menu, then "Filter", then *"Spectral Smile Interpolation (Image Cube)"* and in the batch mode (*"smile_interp3_batch"*).

Chapter 7

Topographic Correction

The compilation of methods as desribed in the subsequent section is mostly taken and further elaborated from our publication [139].
The influence of topographic effects on optical satellite imagery has been studied since the 1980's [130] - [84]. In the 1990's models for the combined atmospheric / topographic compensation based on radiative transfer codes were developed [22] - [95]. Since then different levels of topographic processing are available: top-of-atmosphere (TOA) products (either radiance or reflectance) and surface reflectance. Following reference [86] these methods can further be grouped into Lambertian and non-Lambertian, depending on the TOA radiance / reflectance being treated as independent of observer and solar geometry or not.
Topographic processing is based on a DEM (Digital Elevation Model) or DSM (Digital Surface Model). These can be calculated from Radar images, passive optical sensor data, or Laser data. Examples of free-of-charge medium resolution DEMs (30 - 90 m) are from NASA's SRTM mission and the US/Japan ASTER mission (https://earthexplorer.usgs.gov/).
For the compensation of topographic effects we also need the slope and aspect maps. Topographic slope and aspect are calculated with a default kernel size of 3×3 pixels. The slope map is a discrete approximation of the gradient of the DEM map, the aspect map specifies the direction of the gradient plane with respect to north (= 0°, east=90°)
For the correction of radiometric effects in steep terrain the sky view factor (fraction of the hemispherical sky dome per pixel) is also required. It is normalized to 1 for a flat terrain and can be calculated with the fast horizon algorithm [26] employing a ray tracing method. We use the IDL implementation provided by [23].
A similar ray tracing method can be used to obtain areas of topographic shadow, if the solar elevation and azimuth is specified.

If the DEM does not match the scene, a DEM preparation method is available in ATCOR, which resizes the DEM to the satellite / airborne scene, provided the DEM is larger and covers the complete scene.
In mountainous terrain there are strong bidirectional reflectance effects. Since the BRDF functions are not known for high spatial resolution imagery we have to use empirical methods to compensate topographic effects. The following sections describe the methods available in ATCOR. They are grouped into 'general' and 'special purpose' methods.

7.1 General purpose methods

The most widely used Lambertian method is the cosine method, which was proposed by reference [135]. If g_t denotes the TOA radiance or reflectance of a rugged terrain pixel, then the corrected value g_h corresponding to a horizontal plane is calculated as

$$g_h = g_t \frac{cos\theta_s}{cos\beta} \tag{7.1}$$

This equation already shows its principal limitation: as the local zenith angle β tends to 90°, $cos\beta$ tends to zero and g_h to infinity. The same limitation also pertains to the non-Lambertian Minnaert approach [77] and its variants, see reference [86]:

$$g_h(i) = g_t(i) \left(\frac{cos\theta_s}{cos\beta}\right)^{k_i} \tag{7.2}$$

where k_i is the Minnaert constant for channel i. The Minnaert version was designed to treat the problem of the Lambertian assumption of a perfectly diffuse reflector, because most natural surfaces show bidirectional reflectance properties [66] - [11]. The equations (7.1, 7.2) are based on the assumption that a single illumination source from the direction θ_s, ϕ_s impinges on the surface, while in reality the surface is illuminated by the direct solar beam and the diffuse solar flux from all directions.

7.1.1 C-correction

To compensate topographic effects Teillet [135] introduced a semi-empirical non-Lambertian algorithm to account for the diffuse solar illumination, the C-correction (CC) method,

$$g_h(i) = g_t(i) \frac{cos\theta_s + c_i}{cos\beta + c_i} \qquad (CC) \tag{7.3}$$

where i is the channel index, $c_i = b_i/m_i$, and b_i, m_i are offset and slope, respectively, obtained from a linear regression of g_t versus $cos\beta$.
A slight variation is the inclusion of the DEM slope (Soenen et al. [132]) :

$$g_h(i) = g_t(i) \frac{cos\theta_s \cdot cos\theta_n + c_i}{cos\beta + c_i} \qquad (CS) \tag{7.4}$$

where θ_n is the terrain slope angle (SCS + C model).

7.1.2 Statistical-Empirical correction (SE)

Teillet [135] also proposed the Statistical-Empirical (SE) correction to reduce topographic effects:

$$g_h(i) = g_t(i) - m_i\ cos\beta\ -\ b_i + \bar{g}_t(i) \qquad (SE) \tag{7.5}$$

where $\bar{g}_t(i)$ is the scene-average TOA radiance or reflectance.
A variant of this equation is

$$g_h(i) = g_t(i) + m_i\ (cos\theta_s\ -\ cos\beta) \qquad (SE\ variant) \tag{7.6}$$

where the topography correction depends only on the difference $(cos\theta_s\ -\ cos\beta)$ weighted with the slope m_i of the regression equation.

7.1.3 Lambert + C (LA+C), Lambert + SE (LA+SE)

These methods combine the physical algorithm of chapter 6.2 with an empirical approach (C or SE). The physical part of the method with the assumption of Lambertian reflectance works well in regions of moderate to high local solar elevation angles or low zenith angles β, i.e., $cos(\beta) \geq 0.5$ ($\beta \leq 60°$), and deteriorates as β tends to 90°. On the other hand, the empirical models (C, SE) usually perform well for $cos(\beta) \leq 0.5$. Therefore, a merged algorithm with the Lambertian (LA) assumption for pixels with $cos(\beta) \geq 0.5$ and the C or SE approach for $cos(\beta) \leq 0.5$ is an interesting alternative.

Since the threshold $T_\beta = 0.5$ can cause brightness steps in the scene, we use a smooth transition of the reflectance values of the merged (LA+C), (LA+SE) method for the $cos\beta = (0.45, 0.55)$ interval, (see equation 7.11), effectively eliminating brightness steps in the visual image display.

The C approach (eq. 7.3) or SE approach (eq. 7.5) is applied to the surface reflectance product based on the elevation information from the DEM, but uses flat (horizontal) surface elements, i.e. (omitting the x, y planar coordinates)

$$\rho^{(3)}(\lambda, z) = \frac{\pi \ [L_{TOA}(\lambda, z) - L_p(\lambda, z)]}{T(\lambda, z) \ [E_s(\lambda, z) + E_d(\lambda, z)]} \tag{7.7}$$

where E_d is the downwelling diffuse solar flux on a horizontal plane, i.e., the counterpart of E_d^* for an inclined plane. This means, the terrain slope and terrain reflected radiance L_t is not explicitly taken account, but the effects are implicitly included in the statistical regression of the (assumed flat) surface elements with the $cos\beta$, i.e., the parameter m_i of eq. (7.5) is calculated for each channel. Then the term g_t of eq. (7.5) is ρ of eq. (7.7), and the terrain corrected surface reflectance value is

$$\rho_{SE,i} = \rho_i^{(3)} + m_i \ (cos\theta_s - cos\beta) \tag{7.8}$$

And omitting the channel index for brevity, the last step is the adjacency correction (with index $p2$ for Algorithm "Part 2") which is conducted as for the Part 1 algorithm (eq. 6.22):

$$\rho_{p2}(x, y) = \rho_{SE}(x, y) + q(x, y) \ [\rho_{SE}(x, y) - \bar{\rho}_{SE}(x, y)] \tag{7.9}$$

We also tested a version, where the multiple terrain reflected effects (equations 6.19, 6.20) are included before running the SE compensation, but degraded results were obtained, i.e. it is better to let the SE algorithm handle these effects.
The the two products $\rho_{p1}(x, y)$ and $\rho_{p2}(x, y)$ are merged as follows: let L1 be the list of pixels with $cos\beta \geq 0.5$ and L2 the list with $cos\beta < 0.5$. Then the final product merges the L1 pixels from Algorithm 1 with the L2 pixels of Algorithm 2:

$$\begin{aligned} \rho_i(L1) &= \rho_{p1,i}(L1) \\ \rho_i(L2) &= \rho_{p2,i}(L2) \end{aligned} \tag{7.10}$$

Occasionally, the threshold $cos\beta \geq T_\beta = 0.5$ causes brightness steps in areas around this threshold. Therefore, the last step of the merging calculates the list L3 of pixels with $cos\beta$ in the interval (0.45,0.55) and weights the values of the L1, L2 pixels which are found in L3 by a linear transition between the two methods:

$$\rho_i(L3) = \rho_i(L3(L1))(0.55 - cos\beta)/0.1 + \rho_i(L3(L2))(cos\beta - 0.45)/0.1 \tag{7.11}$$

This removes visual brightness steps in the LA+SE product for all practical purposes

7.2 Special purpose methods

7.2.1 Modified Minnaert (MM)

The Modified Minnaert (MM) is an empirical approach to correct the impact of the variable incidence illumination in mountainous terrain [92, 100]. The local solar zenith angle β (incidence illumination) is usually the major factor in rugged terrain. The view / exitance angle part is not treated. First, a geometric function G is defined:

$$G = \{cos\beta / cos\beta_T\}^b \quad \geq g \tag{7.12}$$

The angle β_T is a threshold defined below. The exponent 'b' depends on the surface type. In this empirical model, a coarse surface type classification is used (vegetation, non-vegetation) with the criterion vegetation index $\rho_{850nm}/\rho_{660nm} > 3$ for vegetation. Obviously, water surfaces are not involved during topographic compensation.

The function G for 'non-vegetation' is applied with a wavelength - independent exponent b=1. After testing a large number of vegetated mountainous scenes the following wavelength-dependence of the 'b' exponent performed best in most cases:

- b=0.75 for channels with $\lambda < 720$ nm and b=0.33 for $\lambda > 720$ nm.

The threshold illumination angle β_T should have some margin to the solar zenith angle to retain the original natural variation of pixels with illumination angles close to the solar zenith angle. The threshold angle can be specified by the user and the following empirical rules are recommended:

- If $\theta_s < 35°$ then $\beta_T = \theta_s + 25°$
- If $\theta_s < 45°$ then $\beta_T = \theta_s + 20°$
- If $45 \leq \theta_s \leq 50°$ then $\beta_T = \theta_s + 15°$
- If $50 \leq \theta_s \leq 60°$ then $\beta_T = \theta_s + 10°$
- If $\theta_s > 60°$ then $\beta_T = max(70°, \theta_s + 5°)$

These rules are automatically applied if $\beta_T = 0$, e.g., during batch processing.

The geometric function G needs a lower bound g to prevent a too strong reduction of reflectance values. Values of G greater than 1 are set to 1, and values less than the boundary g are reset to g (default g=0.25). This means the processing works in the geometric regime from β_T to 90°and the updated reflectance is:

$$\rho_g = \rho_L G, \tag{7.13}$$

where ρ_L is the isotropic (Lambert) value.

The original Minnaert equation 7.2 tends to infinity as β tends to 90°. However, the modified Minnaert (eq. 7.13) does not tend to infinity, because ρ_L is based on eq. 6.16 with a non-zero denominator (because of the diffuse flux on the ground), and the final reflectance (eq. 6.22).

7.2.2 Integrated Radiometric Correction (IRC)

The IRC method was published by Kobayashi and Sanga-Ngoie [63, 64] to provide a combined atmospheric and topographic correction. The algorithm is briefly outlined here, more details can be found in the original papers.

The first step is the orthorectification of the scene using a digital elevation model (DEM). Then the slope and aspect maps are calculated. The next step is the calculation of the sky view factor. The original paper uses the simple equation based solely on the slope angle, but with ATCOR a more accurate calculation based on a ray tracing can also be used in case of a steep terrain. Then the following quantities are computed (keeping the original notation of Kobayashi in most cases):

$$h_0 = \frac{(\pi + 2\theta_s)}{2\pi} \tag{7.14}$$

Here θ_s is the solar zenith angle in radian. If s denotes the slope map (in radian) then the simple version of the skyview is obtained with

$$h = 1 - s/\pi \tag{7.15}$$

The cosine of the local solar zenith (illumination angle β) is given in eq. 6.15. Then the surface radiance for each channel L_s is calculated by subtracting the path radiance L_p from the at-sensor radiance L:

$$L_s(x, y) = L(x, y) - L_p(x, y, z) \tag{7.16}$$

In the ATCOR version of the IRC algorithm the path radiance varies spatially, particularly due to the DEM height variation, while a constant value (per channel) is used in the original IRC paper. Then a regression analysis (per channel) of L_s versus $cos\beta$ is applied to calculate the slope m and intercept b. After defining $C = m/b$ the topographic correction map A is calculated:

$$A(x, y) = \frac{cos\theta_s + C/h_0}{cos\beta(x, y) + C\ h(x, y)/h_0} \tag{7.17}$$

Finally, the surface reflectance ρ is computed according to:

$$\rho(x, y) = \frac{\pi\ L_s(x, y, z)\ A(x, y)}{T(x, y, z)\ \{E_{dir}(x, y, z)\ cos\theta_s + E_{dif}(x, y, z)\}} \tag{7.18}$$

where T is the total ground-to-sensor transmittance, and $E_{dir},\ E_{dif}$ are the direct irradiance and diffuse solar flux on the ground, respectively.

So the ATCOR version of IRC contains some improvements with respect to the original method: the path radiance varies spatially, mainly caused by terrain height variations, possibly also due to visibility variations, and the sky view factor can be provided from a ray tracing analysis instead of the local slope angle.

Note: unphysically large (> 1 reflectance unit) or small (< 0) surface reflectance values might happen in areas with topographic shadow or low local sun elevations.

7.3 Recommended Method

Results of this methods for satellite and airborne systems have been evaluated in alpine areas [139]. In most cases the method LA+SE performs best, while the modified Minnaert method has sometimes shown advantages for high resolution instruments.

Chapter 8

Correction of BRDF effects

The bottom of atmosphere reflectance as retrieved after standard ATCOR atmospheric compensation is highly variable due to the influence of the bidirectional reflectance distribution function (BRDF, [82]). The observed reflectance value may deviate from the average spectral albedo by up to 30%, specifically for vegetation and man made surfaces.

Although BRDF effects also play a role during topographic correction (chapter 7) we present this topic from a different perspective, because ATCOR offers three different methods of correcting BRDF effects:

- The empirical approaches for rugged terrain presented in chapter 7, mainly intended to correct for the incidence angle effects.
- An algorithm for flat terrain normalizing off-nadir reflectance values to the corresponding nadir value, mainly intended for wide field-of-view airborne imagery.
- The third method corrects the observation BRDF effects by fitting a physical BRDF model to a number of images and surface cover classes in order to obtain a generic BRDF correction function. This function is used to calculate a per-pixel anisotropy factor which corrects for the deviation from an averaged spectral albedo.

In some cases of rugged terrain imagery it is useful to apply both, incidence and observation angle correction methods of BRDF.

8.1 Nadir normalization

A simple algorithm was implemented as part of the ATCOR package to normalize the scan angle dependent brightness values to the nadir value. It is recommended to apply the method to imagery after atmospheric correction, i.e., to reflectance data. However, if only the across-track illumination gradients shall be removed without any further atmospheric correction, the algorithm can also be applied to radiance (DN) data. In this case, the brightness gradient may be caused by a combination of surface BRDF and atmospheric BRDF (left/right asymmetry in path radiance).

The algorithm is intended for large field-of view sensors (minimum FOV=20°). It computes the column means with a certain angular sampling interval (1° or 3°). The input image may be geocoded or not. If it is not geocoded the total field-of-view FOV corresponds to the number n of across-track image pixels per line. If geocoded, the scan angle for each pixel must be provided in a separate file ("_sca"). It contains the scan angle in degree scaled with a factor of 100, and coded

with 16 bits per pixel. This definition is taken from the airborne ATCOR/PARGE interface [95]. Scan angles on the right hand side with respect to flight heading are defined as negative, those on the left side as positive, e.g., a value of -2930 represents a scan angle of 29.3° on the right side.

The nadir region is defined here as the ±3° scan angle range. Usually, a 3° angular sampling interval, from +3° to +FOV/2 on the left side and -3° to -FOV/2 on the right side, is adequate, except for geometries close to the hot spot geometry. In the latter case, a 1^o sampling interval can be selected.

If $\bar{b}_{nadir}$ denotes the averaged brightness value for the nadir region, i.e., reflectance or radiance, then the nadir normalized brightness value of a pixel with column number j is calculated as:

$$b_{norm}(j) = b(j)\frac{\bar{b}_{nadir}}{f_2(j)} \tag{8.1}$$

where the function f_2 is obtained with three processing steps:

- The first step is the averaging over each interval (3° or 1°). It yields a function f_1 with m+1 grid points for the m off-nadir intervals plus the nadir interval.
- Two cases are distinguished now: if the image is not geocoded, an interpolation from function $f_1(m+1)$ to a function $f_2(ncols)$ is performed where ncols is the number of column pixels of the image. If the image is geocoded, an interpolation from the 3° grid to the 1° grid is performed (no hot spot case).
- The third step is a filter with a moving average window applied to the f_2 function. The following cases are distinguished: if the image is not geocoded the window is 9 pixels (without hot spot) and 3 pixels (with hot spot option). If the image is geocoded, the moving window extends over a 5° angular interval (no hot spot) and over a 3° interval (with hot spot option).

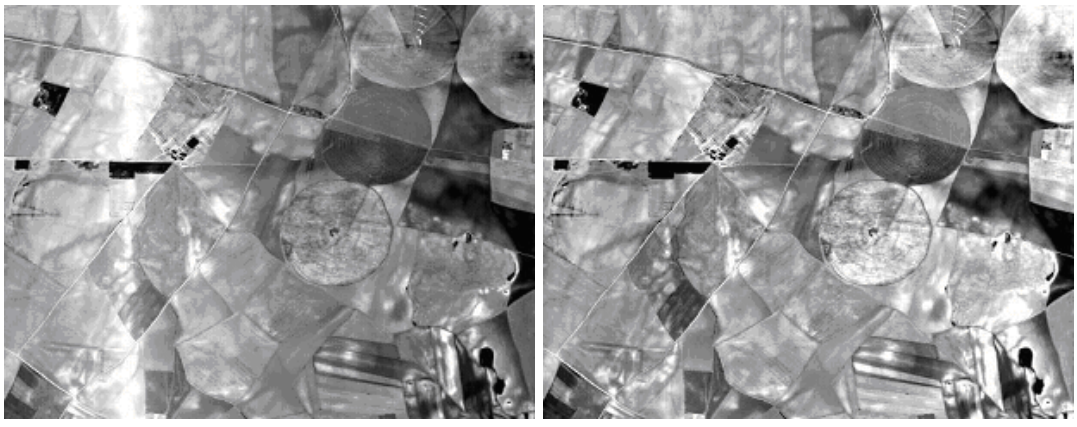

Figure 8.1: *Nadir normalization of an image with hot-spot geometry.*
Left: reflectance image without BRDF correction. Right: after empirical BRDF correction.

Figure 8.1 shows part of a HyMap image (acquired 3 June 1999, Barrax, Spain, 12:09 UTC) containing the hot spot geometry. The solar azimuth was 181° and the sensor scan line azimuth was 179°, almost exactly pointing into the solar azimuth. The left image shows HyMap band 30 at 868 nm after atmospheric correction. The right image is the result after nadir normalization with a

1° sampling interval. In this example, the column means were calculated globally, i.e. surface cover independent. The algorithm also contains an option to compute the column means separately for 4 surface covers. It can currently only be selected if the input imagery is reflectance data and not geocoded. The processing time is much larger than for the global, cover-independent method. The four surface classes are:

- bright vegetation (ratio vegetation index NIR/RED > 10);
- medium/dark vegetation (6 < ratio vegetation index < 10);
- dry vegetation or mixed vegetation/soil (3 < vegetation index < 6);
- soil (vegetation index < 3).

The reflectance of off-nadir water pixels (criterion: near infrared reflectance < 0.05) is not modified.

8.2 BREFCOR

A generic BRDF effects correction routine (BREFCOR, [119] has been included in ATCOR. The idea is to apply a scaling of the volume scattering and the geometric scattering component within a well accepted BRDF model. A fuzzy surface cover index of the complete image is used for this purpose, which covers all surface types from water to asphalt and concrete, soils, sparse vegetation and dense vegetation.

The Ross-Li-sparce reciprocal BRDF model has been selected as basis for the correction of reflectance anisotropy [48]. This model is mainly developed for vegetation, but we use it in a scaled way for all kind of surfaces. Literature mainly related to MODIS atmospheric correction routines showed the superior performance of this model if compared to others. However, for high spatial resolution instruments also other models may be applicable.

8.2.1 Selected BRDF kernels

The BRDF correction scheme is based on the Ross-Thick Li-Sparse Model (RTLS), potentially enhanced by the Hot-Spot function as proposed by Maignan et al. [71]. For the correction, a formulation of the model for the Bidirectional Reflectance Factor (BRF) is used. The BRF is well suited for correction of the HDRF, as both quantities are defined as 1.0 for a 100% reflecting target at the same observation geometry, and as only the second dimension (observation direction) relative variation of the BRF is used for the correction. The generic RTLS-equation of the BRF for each pixel and spectral band is given as:

$$\rho_{BRF} = \rho_{iso} + f_{vol} K_{vol} + f_{geo} K_{geo}, \tag{8.2}$$

where ρ_{iso} is the isotropic reflectance defined at nadir for both illumination and observation angle. The kernel factors f_{vol} and f_{geo} are weighting coefficients for the respective kernels. They depend on the ground coverage BRDF, whereas the kernels are fixed functions which define a fully bi-directional eflectance property. The kernels have been selected according to the findings of BRDF literature [140] For the volume scattering, the Ross-Thick kernel is modified to include the hot-spot extension by Maignan, i.e.

$$K_{vol} = \frac{4}{3\pi} \frac{1}{\cos\theta_i + \cos\theta_r} \left[\left(\frac{\pi}{2} - \zeta \right) \cos\zeta + \sin\zeta \right] - \frac{1}{3}, \tag{8.3}$$

where $\zeta = \arccos(\cos\theta_i \cos\theta_r + \sin\theta_i \sin\theta_r \cos\phi)$.

The angle θ_i is the incident solar zenith angle, θ_r is the observation zenith angle, and ϕ is the relative azimuth angle $\phi = \phi_i - \phi_r$ (i.e., the difference between incidence and observation azimuth). The extension of this volumetric kernel by Maignan is given as:

$$K_{vol} = \left(K_{vol} + \frac{1}{3}\right)\left(1 + \frac{1}{1 + \zeta/1.5^o}\right). \tag{8.4}$$

The reciprocal Li-Sparse kernel is used for the geometric part. It is defined as:

$$K_{geo} = \frac{1}{\pi}(t - \sin t \cos t)\left(\frac{1}{\cos\theta_i} + \frac{1}{\cos\theta_r}\right) \quad - \left(\frac{1}{\cos\theta_i} + \frac{1}{\cos\theta_r}\right) + \frac{1 + \cos\zeta}{2\cos\theta_i \cos\theta_r}, \tag{8.5}$$

where
$t = \arccos\left(\frac{\sqrt{\tan^2\theta_i + \tan^2\theta_r - 2\tan\theta_i \tan\theta_r \cos\phi + (\tan\theta_i \tan\theta_r \cos\phi)^2}}{\frac{1}{\cos\theta_i} + \frac{1}{\cos\theta_r}}\right)$.

8.2.2 BRDF cover index

A continuous BRDF cover index (BCI) function is used for characterization of the surface. It is calculated on the HDRF of four standard bands: blue at 460nm, green at 550nm, red at 670 nm, and near infrared at 840nm. This reduced selection of spectral bands makes the index applicable for most current optical remote sensing systems. The BCI function characterizes the image based on intrinsic BRDF properties from strong forward scatterers (water) to neutral targets (asphalt) to backward scatterers (soils and vegetation types). The index implementation is using the normalized difference vegetation index (NDVI) as a first input for vegetation density quantification due to its known relation to the leave area index (LAI), which has a significant influence on the BRDF [69].

The NDVI is increased in equation (8.6) by a value of up to 0.5 using the fact that dense agricultural vegetation shows higher green reflectance than dense forests; i.e., the NDVI is increased by C_{forest} for dense forests having a green reflectance in a range below 0.07 (reflectance units). In a further step, the BCI is decreased for soils by C_{soils} using the effect that soils show a relatively low blue at-sensor radiance. A last adaption C_{water} is made for water such that clear water areas are always set to a minimum value:

$$BCI = (NDVI + C_{forest} - C_{soils} - C_{water}) > -1.2. \tag{8.6}$$

Note: the ">" -sign denotes a maximum operator between the left and the right side of the term.

The three correction functions in Equation 8.6 are given as follows, first for forests using the absolute HDRF value in the green ρ_{green}:

$$C_{forest} = \frac{0.5}{0.04 \cdot 0.2} \cdot \left([0.07 - \rho_{green}]_{0.00}^{0.04}\right) \cdot \left([NDVI - 0.55]_{0.00}^{0.20}\right). \tag{8.7}$$

The upper and lower values at the square brackets indicate a truncation at these values. The upper values could be adapted for better representation of biome types. For surface covers having a BCI below 0.1 (i.e., mostly soils), a reduction factor is found from the relation between blue and red HDRF as:

$$C_{soils} = \frac{\rho_{blue}}{\rho_{red}}\left([1 - 10 \cdot (NDVI + C_{forest})]_{0.00}^{1.00}\right). \tag{8.8}$$

This factor accounts for the variability of non-vegetated areas in the visible. Finally, a summand to account for water is added, starting with $BCI_{soil} = NDVI + C_{forest} - C_{soils}$. It takes into account the relatively higher reflectance of water in the green spectral band in relation to the blue for discrimination to other surface targets such as shadows and dark asphalt:

$$C_{water} = \left(\left(\frac{\rho_{green}}{2\rho_{blue}} - 0.8\right) > 0\right) \cdot \left(-3\left((BCI_{soil} + 0.5) < 0\right)\right). \tag{8.9}$$

The range of the final BCI function is defined between values of -1.20 and 1.50. The BCI-index calculated in each image pixel can then be used for BRDF model calibration and subsequently for image correction.

8.2.3 BRDF model calibration

For the calibration of the model, the BCI is divided into a number of 4-6 discrete classes. The evaluation has shown that increasing the number of classes often leads to worse fitting results and less stable BRDF correction whereas keeping the number of classes small is more stable. A second outcome was that it is hardly feasible to define generic class limits for any kind of data acquisition and sensor. The calibration follows the scheme shown in Figure 8.2.

Differences in limits can be attributed to the fact that the higher resolution images allows for a more accurate and statistically more relevant calibration of the model whereas for lower resolution, the number of classes should be reduced. The classes can be denominated as: water, artificial materials, soils, sparse vegetation, grassland, and forests. For each of the classes, the optimum kernel weights are calculated and stored for each image of a campaign. All weights are then averaged while bad fitting classes (with relative errors greater than 10%) are excluded from averaging. No BRDF correction is applied for classes without any fitting parameters (i.e. if less than 3 bands out of 4 within the class could be calibrated). The averaged model is stored for later application to the imagery.

8.2.4 BRDF image correction

Finally, the derived BRDF model calibration data are to be applied to the image data. For application on the imagery, the BCI has to be calculated from each image and is used to get a continuous correction function.
The image processing procedure consists of the following steps (compare Figure 8.3):

- calculate the BCI from image,
- calculate the scene-specific angular kernels subsets,
- interpolate the calibration data from BCI levels to a continuous BRDF model,
- calculate an anisotropy map by scaling the kernels using the BCI, the scan angles (observation zenith and azimuth angle), and the interpolated BRDF model, and
- apply the anisotropy map on a per-pixel basis.

The anisotropy factor is derived as relation of the directional model for each pixel to the same model averaged over all angles (i.e., to a good approximation of the spectral albedo BHR).

$$ANIF = \frac{\rho_{iso} + f_{geo}K_{geo,\theta_i,\theta_r,\phi} + f_{vol}K_{vol,\theta_i,\theta_r,\phi}}{\rho_{iso} + f_{geo}\overline{K_{geo}} + f_{vol}\overline{K_{vol}}} \approx \frac{\rho_{BRF}}{\rho_{BHR}}. \tag{8.10}$$

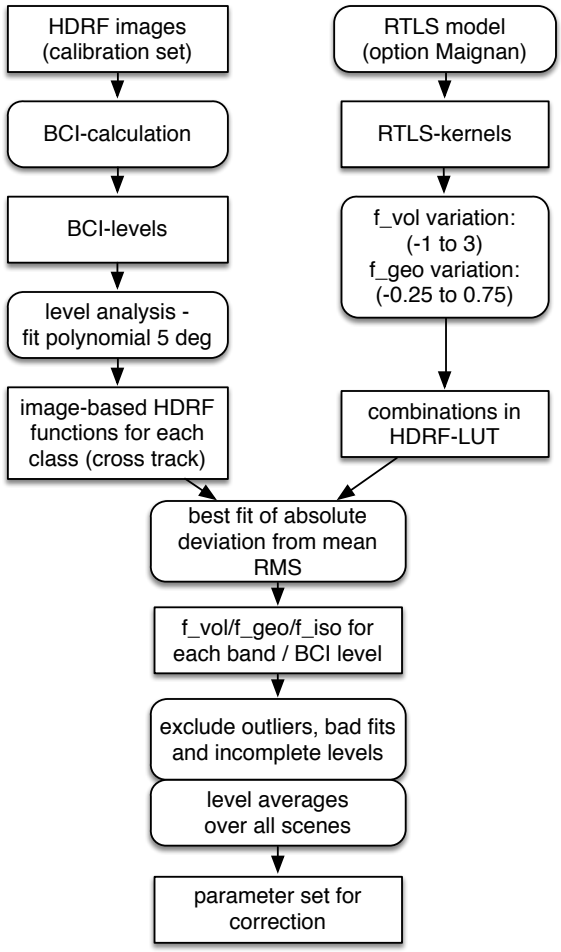

Figure 8.2: *BRDF model calibration scheme*

The bihemispherical reflectance is described by the two hemispherical averages $\overline{K_{geo}}$ and $\overline{K_{vol}}$ weighted by the respective factors and added to the constant isotropic reflectance ρ_{iso}. Alternatively, the anisotropy with respect to nadir BRF would be an option as done in earlier BRDF research [110]. This option is currently not supported in BREFCOR, as the BHR is the more generic spectral albedo definition for surface object characterization.
The corrected bihemispherical reflectance is finally calculated as $\rho_{BHR} = \frac{\rho_{HDRF}}{ANIF}$, where ρ_{HDRF} is the bottom of atmosphere (directional) reflectance after standard ATCOR atmospheric compensation, as described above.

8.3 Mosaicking

Mosaicking is another topic related to BRDF effects. ATCOR contains a GUI tool to mosaic a number of georectified scenes in an efficient way, see the ATCOR User Guide [104, 105].

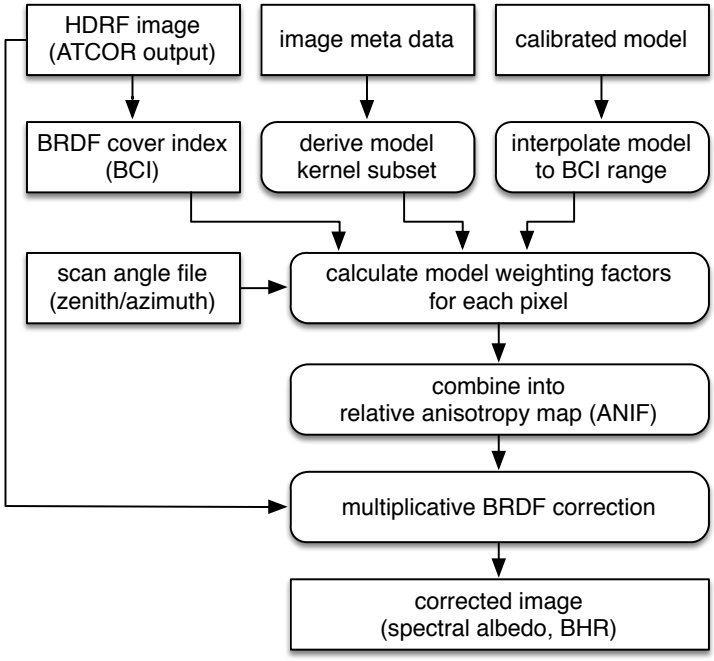

Figure 8.3: *Image correction scheme.*

Chapter 9

Hyperspectral Image Filtering

For hyperspectral imagery different spectral filters or polishing algorithms are provided to remove small spectral spikes. The best method depends on the image data and sensor-specific noise level of the scene [117]

9.1 Spectral Polishing: Statistical Filter

Inputs:

Input file name A hyperspectral image cube, usually the output of atmospheric correction ∗_atm.bsq

Sensor Spectral Response Defines the first band of the sensor response ∗rsp. This field may be left empty - in that case, the wavelength information from the ENVI header is used if the wavelengths tag is properly given. if no wavelength reference is there, a spectrally equidistant succession of the spetral bands is assumed.
Note: the Savitzky-Golay filter is not wavelength-aware and uses always the assumption of equidistant, constantly increasing bands.

Number of polishing bands on each side Adjacent bands to be used for calculation on each side of the target band; e.g. factor 3 uses 7 bands for polishing (3 on each side plus central band).

Smoothing Factor smoothing applied stand alone or in combination with the derivative filter:
0: no smoothing
1: slight smoothing (filter: 1/4/1)
2: moderate smoothing (filter: 1/2/1)
3: standard smoothing (filter: 1/1/1)
4 and more: standard smoothing with moving average

Polishing Filter Type Four options are available for statistical spectral polishing: *Derivative Filter:* all spectral bands of the given window size are taken into account to calculate derivative used to reconstruct the value of the center band.
Neighbour Derivative: all spectral bands except for the center itself are taken into account to calculate derivative used to reconstruct the value of the center band.
Lowpass Filter: Only the smoothing is performed, no derivatives are calculated.
Savitzky-Golay: Filter to perform a numerical polinomial fit of 4th degree through the selected total window size.

Output:
A cube containing the spectrally filtered copy of the original image data cube is generated.

9.2 Pushbroom Polishing / Destriping

This routine treats each detector pixel of a pushbroom imaging spectrometer separately and derives gain and optional offset values in comparison to its direct neighbors. The routine may be used for both, spectral polishing of residual gain/offset errors and for destriping of pushbroom imagery.

Inputs:

Input file name A hyperspectral image cube, usually the output of atmospheric correction *_atm.bsq

Interpolation Distance Number of pixels from center pixel, i.e., a factor of 2 uses 2 pixels on each side for calculation of residual gains. The distance should be in a range of the width of visible striping artefacts.

Polishing Filter Type Three options are available for pushbroom spectral polishing: *Spectral:* Polishing is done in spectral dimension only; one adjacent band on each spectral side is taken for residual calculation.
Spatial: Only the spatial filter is applied; use this option for destriping of imagery.
2D Filter: Do both dimensions (spatial/spectral) simultaneously the filter size only applies to the spatial dimension, however..

Type of Correction Function For each detector pixel, correction parameters are generated:
Gain and Offset: Calculate average residual gain and offset for each pixel and apply them as correction function.
Gain Only: Constrain the residual gain to an offset of 0; this is the typical situation.

Output:
A cube containing the spectrally filtered copy of the original image data cube is created. As a side output, a gain file is written (name: _gain.bsq'), containing the following three layers: 1: offset of linear recalibration offset function
2: gain of linear recalibration offset function
3: gain of linear recalibration offset function if function is constrained to zero offset
such that the corrected spectral band is: $L_{polish} = L_{ori} - [L_{offs} + gain * L_{ori,smooth}$

9.3 Flat Field Polishing

This routine is to remove spectral artifacts from atmospherically corrected imaging spectroscopy data. Average residual gains and offsets are calculated by comparison of assumed flat field data values to the measured values for each spectral band to find a gain correction factor. The flat field is searched automatically within an image as the spectrally least variable part of the image.

Inputs:
Input file name (usually output of atmospheric correction _atm.bsq), can be any kind of image. Type of Correction Function:

- Gain and Offset: calculate average residual gain and offset for each pixel and apply them as correction function
- Gain only: constrain the residual gain to an offset of 0; this is the typical situation.

Output:
A cube containing the spectrally filtered copy of the original image data cube is created.

Chapter 10

Temperature and emissivity retrieval

Land and sea surface temperature are important parameters in the climate system influencing the surface energy balance, air temperature, ana evapoartion. Other remote sensing application fields are the mapping of high temperature events (volcanos, wildfires), urban heat islands, analysis of soil moisture, and the differentiation of rocks, soil, and vegetation. Airborne thermal instruments have been operating since the early 1970s [138]. Later, the spaceborne Landsat and ASTER missions collected thermal images available to a large community of researchers. This chapter describes the basic concepts and algorithms to evaluate thermal infrared data.

For remote sensing of the earth's surface only the 3 - 5 μm (Mid-IR = MIR) and 8 - 14 μm (Thermal IR = TIR) spectral regions offer atmospheric windows with a sufficiently high transmittance, see Figure 10.1. The plot is calculated with the MODTRAN5 code for a vertical path from space to sea level, using a mid-latitude summer atmosphere (water vapor column W=2.91 cm) and a rural aerosol (visibility 23 km). Very strong atmospheric absorption region are around 4.3 μm (CO_2), from 5 - 8 μm (mainly water vapor), and beyond 14 μm (CO_2 and water vapor). Around 9.3 μm ozone absorption has an influence for spaceborne missions.

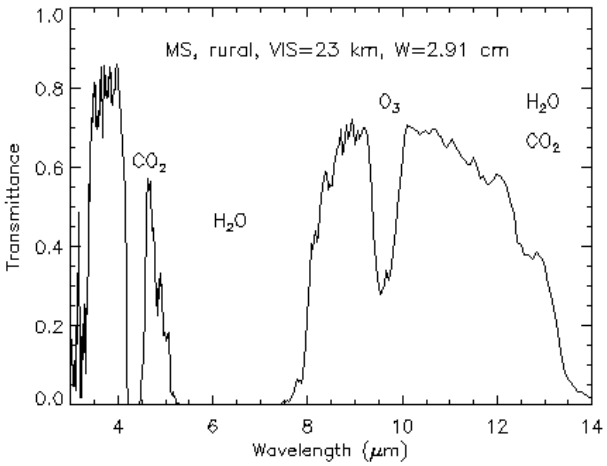

Figure 10.1: *Atmospheric transmittance 3 - 14 μm.*

For daytime data acquisition the MIR radiance at the sensor consists of reflected solar radiation and emitted thermal radiation, see Figure 10.2. It presents the reflected solar radiance (without

atmosphere) for surface reflectances of $\rho = 0.01, 0.1, 1.0$ on a double logarithmic scale, and the emitted earth radiation for a 300 K blackbody. The sun is modeled as a 5800 K blackbody at a distance of 1 astronomical unit, i.e. $150 * 10^6$ km,, i.e. its blackbody radiation on the earth is decreased by the factor $(0.7/150 * 10^6)^2 = 2.17 * 10^{-5}$, where the sun radius is approximately $0.7 * 10^6$ km. In the MIR region solar and emitted radiation have to be taken into account, while the solar influence can be neglected in the TIR region, as it is two or more orders of magnitude smaller.

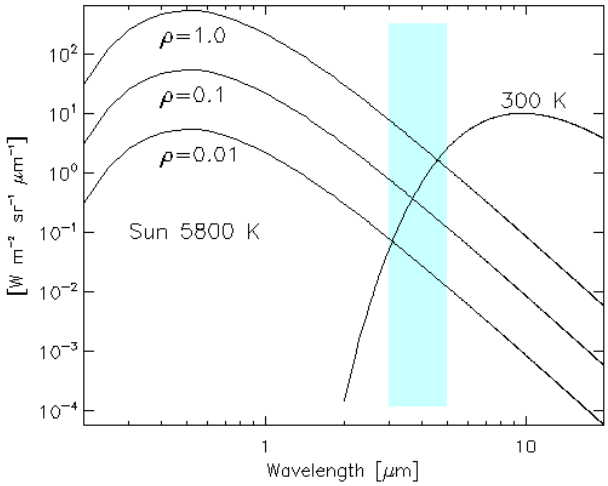

Figure 10.2: *Reflected solar and emitted thermal radiance.*

According to Planck's equation the emitted blackbody spectral radiance L depends on wavelength λ and temperature T,

$$L_{bb}(\lambda, T) = \frac{2\ h\ c^2}{\lambda^5}\ \frac{1}{exp(h\ c/\lambda\ k_B\ T) - 1} \tag{10.1}$$

where h is Planck's constant, c the speed of light, and k_B the Boltzmann constant. For natural bodies with emissivity $\varepsilon(\lambda)$ the emitted spectral radiance is

$$L(\lambda, \varepsilon, T) = \varepsilon(\lambda)\ L_{bb}(\lambda, T) \tag{10.2}$$

The following discussion is restricted to the TIR region (8 - 14 μm), i.e. the solar influence can be neglected. Then the radiative transfer equation can be written as

$$L(\lambda) = L_p(\lambda) + \tau(\lambda)\ \varepsilon(\lambda)\ L_{bb}(\lambda, T) + \tau(\lambda)\ \ (1 - \varepsilon(\lambda))\ \ F(\lambda)/\pi \tag{10.3}$$

where L, L_p, F are TOA or at-sensor radiance, path radiance, and thermal downwelling flux on the ground, respectively, and ε, τ are the surface emissivity and ground-to-sensor atmospheric transmittance, compare Figure 10.3. Except for the emissivity and L_{bb}, all quantities of equation 10.3 depend on atmospheric parameters, especially on the water vapor column. The adjacency effect can usually be neglected, as the aerosol scattering efficiency strongly decreases with wavelength. Multiplying both sides of eq. 10.3 with the channel spectral response function $R(\lambda)$ and integrating over the bandpass yields (k = band number) :

$$L(k) = L_p(k) + \tau(k)\ \varepsilon(k)\ L_{bb}(k, T) + \tau(k)\ \ (1 - \varepsilon(k))\ \ F(k)/\pi \tag{10.4}$$

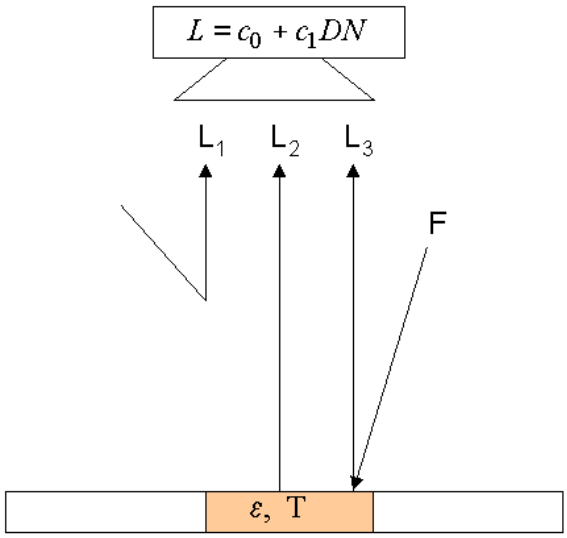

Figure 10.3: *Sketch of thermal radiation components.*

If we define the effective surface radiance L_s as

$$L_s(k,T) = \varepsilon(k)\ L_{bb}(k,T) \tag{10.5}$$

we obtain

$$L_s(k,T) = \frac{L(k) - L_p(k)}{\tau(k)}\ -\ (1-\varepsilon(k)) \cdot F(k)/\pi \tag{10.6}$$

and the atmospheric correction provides the quantities $L_p,\ \tau,\ F$. In case of a blackbody, i.e. $\varepsilon(k) = 1$, we get

$$L_s(k,T) = \frac{L(k) - L_p(k)}{\tau(k)} \tag{10.7}$$

The blackbody radiance / temperature relationship is obtained from Planck's law and the channel spectral response function $R(\lambda)$. It is calculated as ($c_1,\ c_2$ = radiation constants):

$$L = \frac{\int_{\lambda_1}^{\lambda_2} \frac{c_1}{\lambda^5} \frac{1}{exp(c_2/\lambda T)-1}\ R(\lambda)\ d\lambda}{\int_{\lambda_1}^{\lambda_2} R(\lambda)\ d\lambda} \tag{10.8}$$

The relationship $L = f(T)$ can be accurately approximated by

$$L = \frac{k_1}{exp(k_2/T) - 1} \tag{10.9}$$

where the coefficients $k_1,\ k_2$ depend on $R(\lambda)$ and they are calculated for a certain temperature interval, e.g., (250 - 350 K). Then, $T = f^{-1}(L)$ is calculated as:

$$T = \frac{k_2}{ln\left((k_1/L) + 1\right)} \tag{10.10}$$

In this chapter we discuss several methods of temperature and temperature / emissivity retrieval implemented in ATCOR. These are suitable to process single-band thermal, two-band, multispectral

and hyperspectral thermal data. The interested reader is referred to a review article on land surface temperature and emissivity estimation [25] for an overview of thermal retrieval methods. Special algorithms were developed for the processing of hyperspectral thermal data, i.e., In-scene Atmospheric Compensation (ISAC, [145]), Autonomous Atmospheric Compensation (AAC, [41]), and ARTEMIS [14], the first of which is also supported in ATCOR.

- Reference channel method [57]
- Split-window method [76]
- Normalized emissivity method NEM [38, 85]
- Temperature / emissivity separation TES [39]
- In-scene atmospheric compensation ISAC [145]
- Split-window covariance-variance ratio SWCVR [62]

10.1 Reference channel

The simplest way to calculate the kinetic temperature is a knowledge or a close estimate of the emissivity in band k. Then we can use $\varepsilon(k)$ and equations 10.5, 10.6 to solve for the blackbody radiance $L_{bb}(k,T) = L_s(k,T)/\varepsilon(k)$ and equation 10.10 to obtain the corresponding kinetic temperature T. This approach can be used for homogeneous scenes with little variation of the emissivity or with an emissivity map derived from other instruments [131]. The method is usually applied to single-band thermal data (Landsat-4,-5,-7).

10.2 Split-window for Landsat-8 TIRS

The split-window technique was originally developed to estimate sea surface temperature from space using two thermal bands around 11 μm and 12 μm [76]. The blackbody temperature in both bands is slightly different because of a difference in atmospheric water vapor absorption, and a linear relationship can be used to calculate the surface temperature. In ATCOR this method is applied to data of the Landsat-8 TIRS sensor. This instrument records data in two thermal channels (B10, B11) with center wavelengths near 10.9, 12.1 μm, respectively. The pixel size of the data is resampled to 30 m to match the pixel size of the OLI data. The employed split-window equation for the approximate calculation of the surface temperature T_s is

$$T_s = T_{bb10} + 2\,(T_{bb10} - T_{bb11}) + 1 + T_{offset} \tag{10.11}$$

where T_{bb10}, T_{bb11} are the blackbody temperatures of B10, B11, respectively, and T_{offset} is an optional user-specified offset which is 0 if not specified. The equation (with $T_{offset} = 0$) holds for a surface emissivity of 0.98 in both TIRS bands, which is typical for vegetation. Figure 10.4 shows the corresponding surface temperature error for the mid-latitude summer (MS) and US standard atmospheres with the ground at sea level and 0.5 km above sea level. The sea level air temperatures for the MS and US atmospheres are 294 K and 288 K, respectively. The three curves correspond to surface temperatures 10 K below and above air temperature and same as air temperature. The shaded areas indicate a typical range of humidity (water vapor) conditions. The surface temperature error in the shaded regions is smaller than 0.5 K (US) and 1 K (MS). For the MS atmosphere and water vapor columns ranging from 0.5 - 2.5 cm the error is also smaller than 0.5 K.

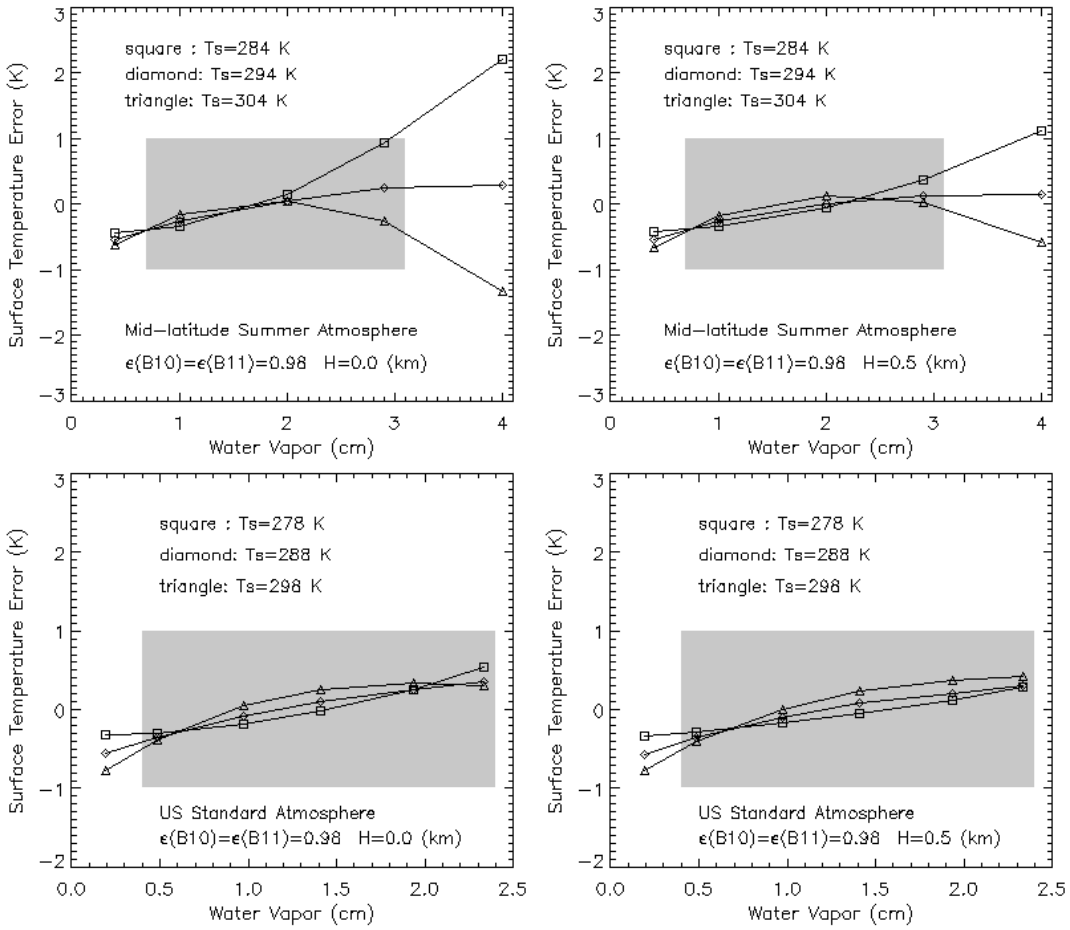

Figure 10.4: *Surface temperature error depending on water vapor column (emissivity=0.98).*

Figure 10.5 shows the corresponding surface temperature error for the same atmospheric conditions, but with the spectral emissivity of water. A temperature offset $T_{offset} = -1$ has to be specified to obtain temperature retrieval errors smaller than 0.5 K. The reason is that the spectral emissivity of water (see Fig. 10.6) is not constant in the thermal spectral region.
The last case presents the surface temperature error for a constant emissivity of 0.95 in the spectral region of B10 and B11, typical for asphalt, see Fig. 10.7. Here, a temperature offset of 2 K in equation 10.11 is required to keep errors smaller than 1 K in most cases in the shaded areas. Higher errors are encountered for H=0 (sea level) if the surface temperature is 10 K below the air temperature.

10.3 Normalized emissivity method NEM and ANEM

The method requires multispectral thermal bands. First, all channels k are assigned a constant emissivity, e.g., $\varepsilon(k) = 0.99$, $(k = 1, ..., n)$. Then a loop over all bands k is executed to calculate the blackbody temperature for each pixel $T_{bb}(x, y, k)$. Then the pixel (blackbody) temperature is defined as the the maximum temperature of all bands

$$T_{max}(x, y) = max\{T_{bb}(x, y, k)\} \quad (k = 1, ..., n) \tag{10.12}$$

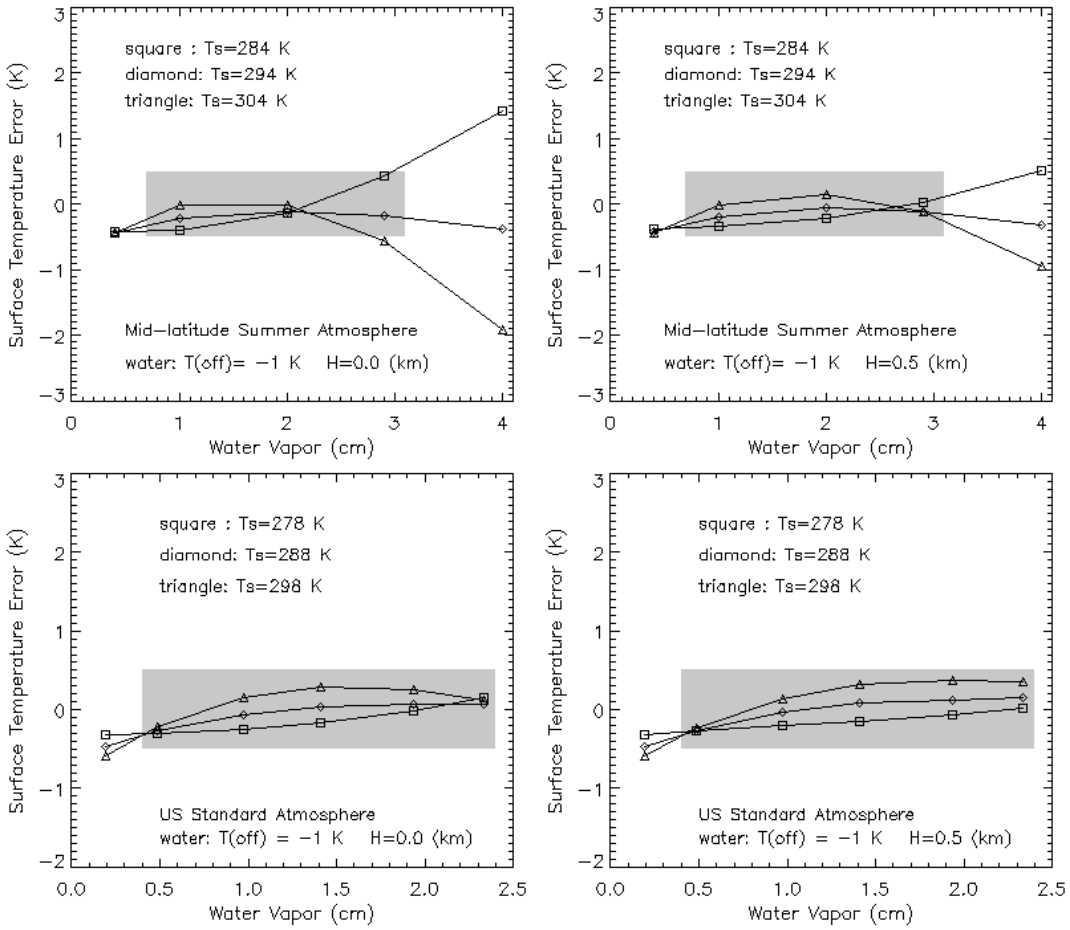

Figure 10.5: *Surface temperature error depending on water vapor column (water surface).*

If a realistic emissivity is chosen, then the blackbody temperature T_{max} is close to the kinetic surface temperature. The last step is the calculation of the emissivity map for each channel $\varepsilon(x, y, j)$. Omitting the spatial coordinates and solving equation 10.4 for $\varepsilon(k)$ we get

$$\varepsilon(k) = \frac{\{L(k) - L_p(k)\}/\tau(k) - F(k)/\pi}{L_{bb}(T_{max}) - F(k)/\pi} \tag{10.13}$$

In the adjusted NEM (ANEM [19]) the assigned emissivity is surface cover dependent. If we have coregistered VNIR and thermal band imagery, we define four surface cover classes in ATCOR (water, vegetation, soil/dry vegetation, sand/asphalt) based on the following criteria:

- vegetation: $\rho_{nir}/\rho_{red} > 2$ and $\rho_{nir} > 0.20$.
- soil/dry vegetation: $\rho_{nir}/\rho_{red} \geq 1.4$ and $\rho_{nir}/\rho_{red} < 2.0$ and $\rho_{red} > 0.09$.
- sand/asphalt : $\rho_{nir}/\rho_{red} < 1.4$ and $\rho_{red} > 0.09$.

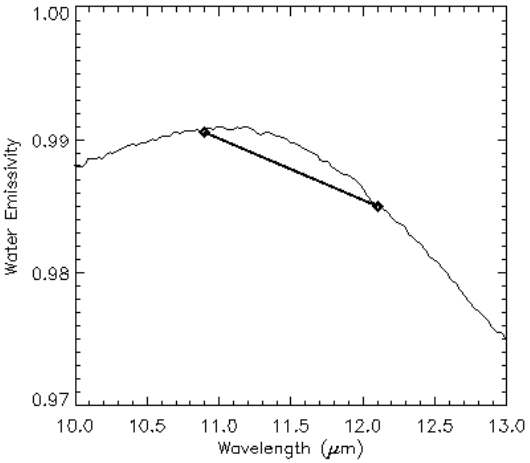

Figure 10.6: *Spectral emissivity of water. Symbols mark the TIRS channel center wavelengths.*

- water : $\rho_{nir} < 0.05$ and $\rho_{1.6\mu m} < 0.03$.

To each class i the user can assign an emissivity $\varepsilon(i,j)$ for a selected maximum emissivity channel j. Usually, the channel j is defined in the 10.5 - 12 μm region, because the spectral emissivity of most surfaces peaks in this region. In case of night data acquisition with purely thermal channels there is only one common emissivity assignment, e.g. $\varepsilon(j) = 0.98$. Once the emissivity map is defined, the remaining NEM steps are executed.
The ANEM method can provide rather accurate emissivity spectra and surface temperatures if the specified maximum channel emissivities are close to reality.

10.4 Temperature / emissivity separation TES

The ASTER TES algorithm is available for sensors with at least 5 channels in the thermal interval (λ_x, λ_y) with $\lambda_x - FWHM_x/2 \geq 8.08\ \mu m$ and $\lambda_y + FWHM_y/2 \leq 13.0\ \mu m$ to exclude channels in strong absorption regions. The TES algorithm implemented in ATCOR consists of 3 major parts [39]:

- the NEM algorithm described above.
- the ratio module:
  It calculates relative emissivities β_i (channel i) by ratioing the NEM emissivity values ε_i to their average:

$$\beta_i = \frac{n\ \varepsilon_i}{\sum_{i=1}^{i=n} \varepsilon_i} \qquad (i = 1, n) \tag{10.14}$$

  Here n is the number of channels in the allowed thermal interval.
- maximum minimum distance (MMD module) :
  The maximum and minimum values of the relative emissivities (β spectrum) are calculated to find the spectral contrast:

$$MMD = max(\beta) - min(\beta) \tag{10.15}$$

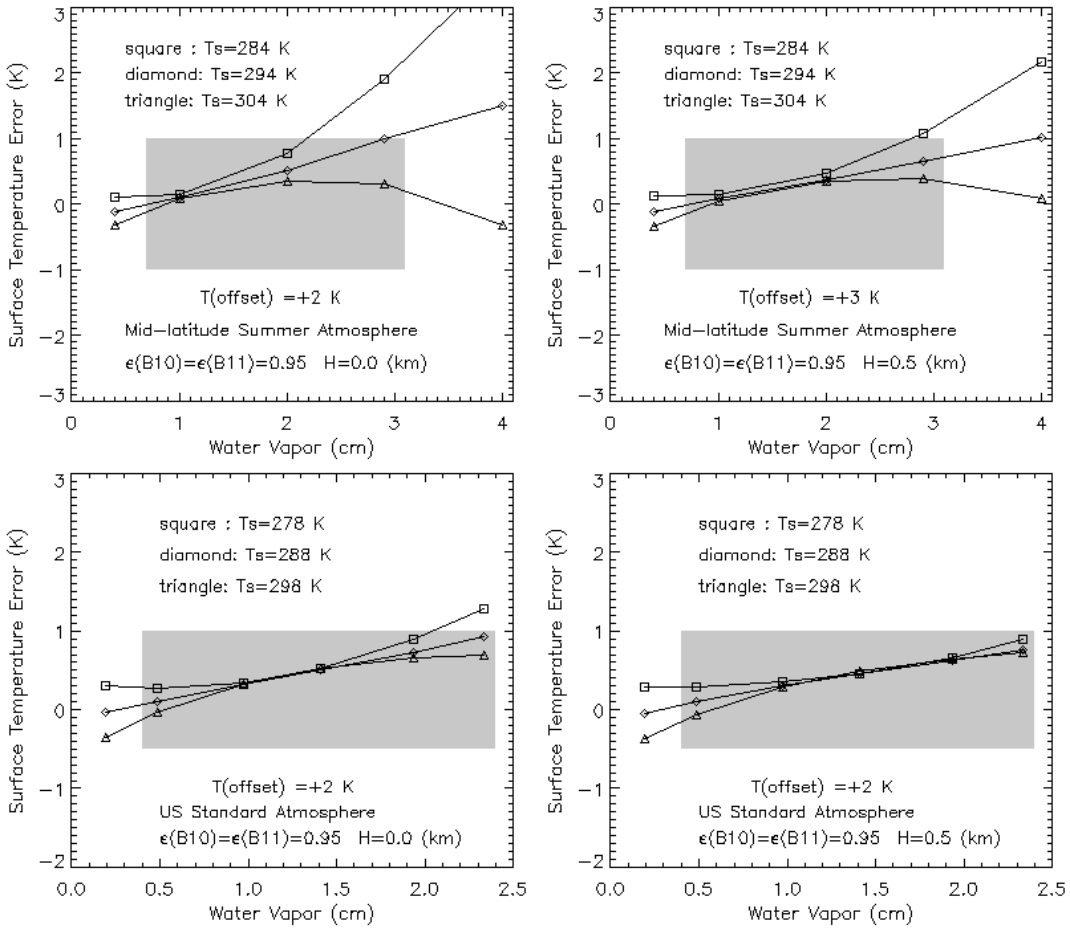

Figure 10.7: *Surface temperature error depending on water vapor column (emissivity=0.95).*

Then an empirical relationship is used to predict the actual emissivities ε_i from the MMD employing a regression with laboratory or field emissivity spectra:

$$\varepsilon_{min} = a + b\ MMD^c \tag{10.16}$$

For small values $MMD < 0.03$ (e.g. water, vegetation) the value ε_{min} is set to 0.983. The 3 parameters (a, b, c) of the regression can be specified by the user, the default values are taken from the original ASTER algorithm [39], i.e., a=0.994, b=-0.687, c=0.737 . The final step calculates the actual emissivities using the β spectrum and ε_{min}:

$$\varepsilon_i = \beta_i \frac{\varepsilon_{min}}{min(\beta)} \qquad (i = 1, n) \tag{10.17}$$

10.5 In-scene atmospheric compensation ISAC

The ISAC method requires at at least 5 thermal channels, but works best for hyperspectral thermal data. A detailed description is given by Young et al. [145]. The method does not require ancillary

meteorological data or atmospheric modeling. It neglects the downwelling thermal flux and employs the equation (channel i)

$$L(i) = L_p + \tau(i)\ \varepsilon(i)\ L_{bb}(T) = L_p(i) + \tau(i)\ L_{surface}(i) \tag{10.18}$$

This approximation is justified for pixels with a high emissivity close to 1, i.e. "blackbody" pixels. First, the highest brightness temperature T_{max}^{sensor} for each pixel in each channel is computed based on the at-sensor radiance L converted into brightness temperature. In the current implementation, only channels in the spectral region 8 - 13 μm are employed for the maximum brightness temperature search, because the spectral regions $\lambda < 8\ \mu m$ and $\lambda > 13\ \mu m$ are strongly affected by atmospheric water vapor absorption. Next, a reference channel is defined where most pixels with maximum brightness temperature occur. Only those blackbody pixels are retained which have the maximum brightness temperature in this reference channel ("most hits" method). For these selected blackbody pixels the scatterplot of measured at-sensor radiance L versus blackbody radiance corresponding to $L_{bb}(T_{max}^{sensor})$ is computed for each channel, see Figure 10.8.

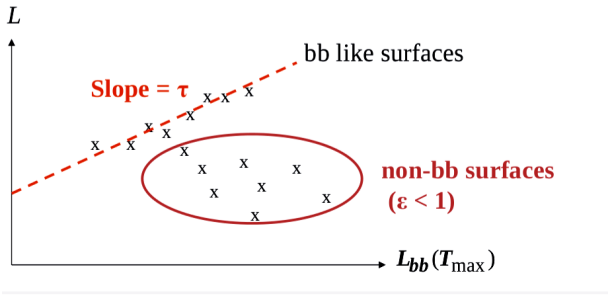

Figure 10.8: *ISAC scatter plot.*

This means the surface radiance of eq. 10.18 is approximated as $L_{surface} = L_{bb}(T_{max}^{sensor})$. The final step is a least squares regression of the scatterplot data $L(i)$ versus $L_{surface}(i)$, yielding the intercept (path radiance $L_p(i)$) and slope (transmittance $\tau(i)$) of eq. 10.18. The emissivity spectrum is then calculated as

$$\varepsilon(i) = \frac{L(i) - L_p(i)}{\tau(i)\ L_{bb}(T_{max})} \tag{10.19}$$

Care has to be taken to apply the regression only to the points near the top edge of all cluster points, but allow some margin, so the fitting line is allowed to sink by an amount of the sensor noise equivalent spectral radiance (NESR). The quality of the regression is significantly increased by allowing only those pixels in the scatterplot that had their maximum temperatures in the reference channel.

Limitations of the method:

- A uniform atmosphere is required, as path radiance and transmittance in equation 10.18 are assumed constant. This also implies that the topography should be fairly flat.
- The scene must contain near-blackbody surfaces (vegetation, water).
- The obtained intercept is not the physical path radiance, and the slope not the physical atmospheric transmittance. Both quantities may be negative in some channels, therefore

they are referred to as unscaled path radiance $L_p^{(u)}$ and unscaled transmittance $\tau^{(u)}$. They might be rescaled to proper atmospheric path radiance and transmittance spectra, e.g. using a radiative transfer code.

- The ISAC method requires an adequate spread in surface temperatures in the scene, and surface temperatures higher than the atmospheric radiation temperature. So, results for night-time imagery will likely be degraded.

The compensated unscaled surface radiance spectrum is calculated as

$$L_{surface}^{(u)}(\lambda) = \frac{L(\lambda) - L_p^{(u)}(\lambda)}{\tau^{(u)}(\lambda)} \tag{10.20}$$

and the unscaled ISAC surface emissivity can be obtained with

$$\varepsilon_{isac}(\lambda) = L_{surface}^{(u)}(\lambda) \ / \ L_{BB}(\lambda, T_{ref}) \tag{10.21}$$

where T_{ref} is the brightness temperature image in the reference channel. The compensated surface radiance spectrum $L_{surface}^{(u)}(\lambda)$ can be converted into the equivalent compensated brightness temperature spectrum where most of the atmospheric absorption features are removed. Both the compensated surface radiance and compensated brightness temperature are spectrally consistent with the data and represent the best estimate for the spectral shape. The emissivity spectrum $\varepsilon_{isac}(\lambda)$ may exceed the value 1 in certain channels if the maximum brightness temperature of a pixel does not occur in the selected reference channel. However, a common reference channel is needed in this method to obtain a consistent pixel-independent spectrum of unscaled path radiance $L_p^{(u)}$ and transmittance $\tau^{(u)}$.

10.6 Split-window covariance-variance ratio SWCVR

The method derives the water vapor map from thermal band imagery [62, 68, 55]. The water vapor content W can be retrieved as a function of the ratio $R_{j,i}$ of transmittances τ_i, τ_j in two thermal bands i and j:

$$W = a + b \ R_{j,i} \tag{10.22}$$

with

$$R_{j,i} = \frac{\varepsilon_j \ \tau_j}{\varepsilon_i \ \tau_i} = \frac{\sum_{k=1}^{N} (T_{i,k} - \bar{T}_i) \ (T_{j,k} - \bar{T}_j)}{\sum_{k=1}^{N} (T_{i,k} - \bar{T}_i)^2} \tag{10.23}$$

where N is the number of pixels in a moving window box centered at pixel k, $\bar{T}_i$ is the average brightness temperature in this box, and ε is the land surface emissivity. Equation 10.23 is the ratio of covariance to variance responsible for the abbreviation SWCVR. The two selected channels should be in the 10.5 - 12.5 μm region, where the emissivity of most land surfaces changes only slightly, yielding an emissivity ratio $\varepsilon_j/\varepsilon_i$ close to 1 yielding $R_{j,i} = \tau_j/\tau_i$. Then the parameters "a" and "b" in eq. 10.22 can be calculated from a regression of channel transmittances versus water vapor content using the pre-calculated LUTs. The moving averaging window box is selected at 100 m × 100 m in ATCOR.. The method requires moderate to high temperature contrasts in the moving window, otherwise results are not reliable. Therefore, it is preferable to retrieve the water vapor map from channels in the solar reflective region if possible.

10.7 Spectral calibration of hyperspectral thermal imagery

The spectral calibration in the thermal region using atmospheric absorption features can be conducted in a similar way as for the solar region. A spectral mis-calibration will cause spikes and dips in the surface emissivity spectrum. An appropriate shift of the center wavelengths of the channels will remove these artifacts. This is performed by an optimization procedure that minimizes the deviation between the surface emissivity spectrum and the corresponding smoothed spectrum. However, in the thermal region one also has to account for the unknown surface temperature. Therefore, the merit function also has to be evaluated for a range of surface temperatures T_k and the calculated emissivity depends on the assumed temperature :

$$\varepsilon(i, T_k) = \frac{L(i) - L_p(i) - F(i)/\pi}{L_{bb}(i, T_k) \cdot \tau(i) - F(i)/\pi} \tag{10.24}$$

Here the index i indicates the channel, L is the measured at-sensor radiance, L_p the path radiance, L_{bb} the blackbody radiance, and F the downwelling thermal flux multiplied with the ground-to-sensor transmittance $\tau(i)$. The merit function to be minimized as a function of the wavelength shift δ is :

$$\chi^2(\delta) = \sum_{k=1}^{m} \sum_{i=1}^{n} \{\varepsilon(i, T_k, \delta) - \bar{\varepsilon}(i, T_k, \delta)\}^2 \longrightarrow Min \; ! \tag{10.25}$$

The moving average of the emissivity is performed over 5 channels. In the present version, only channels in the 8.5 - 13.5 μm region are taken into account to avoid strong atmospheric absorption regions. Since MODTRAN look-up tables are used, the resulting wavelength shift also depends on the accuracy of these LUTs. The default temperature range is 280 - 310 K, but the user can specify it with the keyword *trange, e.g. trange=[270,320]*. The temperature increment is fixed at 1 K.

Input to the spectral calibration is the thermal scene (ENVI band sequential format) in the original geometry (i.e. not geocoded). The program will select 10 pixels from 10 image lines in the image center (nadir), calculate the wavelength shift, and the mean and standard deviation. Additionally, there is an optional keyword *box* where the averaging over a specified box of pixels can be specified to reduce the influence of noise. The default is box=1 (no pixel averaging, box=3 performs an averaging over 3 x 3 pixels). A wavelength shift $< FWHM/30$ will have a negligible effect and usually does not require an update of the sensor response functions and sensor-specific atmospheric LUTs.

When starting the spectral calibration program in ATCOR (either in the GUI or batch mode 'sp_calth'), for an image named 'scene.bsq' the corresponding parameter file 'scene.inn' must already be available, because the sensor name and atmospheric LUTs are taken from this file.
Note: this 'scene.inn' file contains the (sea level) water vapor column in its name, e.g. the string 'wv10' in 'h02000_wv10.tem'. The 'wv10' might not be the correct water vapor column, and for instance the 'wv04' or 'wv29' could be more realistic. However, this mainly influences the depth of the atmospheric absorption spectrum, it has a small influence on the wavelength shift calculated during the spectral calibration.

Another module provides the capability of radiometric calibration for hyperspectra thermal band imagery ('thermal_cal') if the scene contains water bodies. An updated radiometric calibration gain $c_1(i)$ per channel i is calculated by fitting the scene emissivity to the theoretical spectral water emissivity curve, assuming the radiometric offset is zero for all bands.

Chapter 11

Cirrus removal

On the first glance, images contaminated by cirrus appear similar to hazy scenes discussed in the previous section. However, haze usually occurs in the lower troposphere (0-3 km) while cirrus clouds exist in the upper troposphere and lower stratosphere (8 - 16 km). The effect of boundary layer haze can be observed in the visible region, but seldom in longer wavelength channels > 850 nm. However, cirrus also affects the NIR and SWIR spectral regions. Thin cirrus clouds are difficult to detect with broad-band multispectral satellite sensors in the atmospheric window regions, especially over land, because land scenes are spatially inhomogeneous and this type of cloud is partially transparent. On the other hand, water vapor dominates in the lower troposphere and usually 90% or more of the atmospheric water vapor column is located in the 0 - 5 km altitude layer. Therefore, if a narrow spectral band is selected in a spectral region of very strong water vapor absorption, e.g., around 1.38 μm or 1.88 μm, the ground reflected signal will be totally absorbed, but the scattered cirrus signal will be received at a satellite sensor or a sensor in a high-altitude aircraft (e.g., 20 km AVIRIS scenes).

So a narrow channel at 1.38 μm is able to detect cirrus clouds, and if a correlation of the cirrus signal at this wavelength and other wavelengths in the VNIR and SWIR region can be found, then the cirrus contribution can be removed from the radiance signal to obtain a cirrus-corrected scene. The basic ideas of cirrus correction were presented in several papers ([34], [35], [37], [102]). The algorithm differs for water and land pixels. For water, a scatterplot of the 1.38 μm versus the 1.24 μm channel is used, for land the band-correlation is determined from a scatterplot of the 1.38 μm versus a red channel (around 0.66 μm). To obtain a high sensitivity, only vegetation pixels are taken because they have a low reflectance in the red spectral region, so the cirrus contribution is easily traced. The scatterplot is computed in terms of the apparent (TOA or at-sensor) reflectance of $\rho_{1.38}$ versus ρ_{red} where the apparent reflectance is defined as:

$$\rho^* = \frac{\pi \; L \; d^2}{E_s \; cos\theta_s} \tag{11.1}$$

where L is the recorded radiance signal, d the Earth-Sun distance (Astronomical Units), E_s the extraterrestrial solar irradiance for the selected band, and θ_s is the solar zenith angle.

11.1 Standard cirrus removal

Following reference [34] the cirrus removal method can be described by the following set of equations:

$$\rho^*(\lambda) = \rho_c(\lambda) \; + \; \frac{T_c(\lambda) \; \rho(\lambda)}{1 \; - s_c(\lambda) \; \rho(\lambda)} \tag{11.2}$$

Here, ρ_c is the reflectance of the cirrus cloud, T_c the two-way transmittance (direct plus diffuse) through the cloud, ρ the reflectance of the *"virtual"* surface (land or water surface including all effects of molecular and aerosol scattering below the cirrus), and s_c is the cloud base reflectance of upward radiation. Eq. 11.2 can be simplified, because of $s_c\ \rho << 1$, yielding

$$\rho^*(\lambda) = \rho_c(\lambda)\ +\ T_c(\lambda)\ \rho(\lambda) \tag{11.3}$$

With the assumption that the cirrus reflectance $\rho_c(\lambda)$ is linearly related to the cirrus reflectance at 1.38 μm in the 0.4 - 1.0 μm spectrum (small variation of single scattering properties of ice crystals, and single scattering albedo close to 1) we obtain

$$\rho^*(\lambda) = \rho_c(1.38\mu m)\ /\ \gamma \qquad 0.4 < \lambda < 1.0\ \mu m \tag{11.4}$$

where γ is an empirical parameter that can be derived from the scene scatterplot of $\rho_{1.38}$ versus ρ_{red} (land) or $\rho_{1.24}$ (water). It depends on the scene content, cirrus cloud height, and solar and viewing angles [35, 102]. Substituting eq. 11.4 into eq. 11.3 yields

$$T_c(\lambda)\ \rho(\lambda) = \rho^*(\lambda)\ -\ \rho_c(1.38\mu m)\ /\ \gamma \tag{11.5}$$

Neglecting the cirrus transmittance T_c (i.e., setting $T_c = 1$), we obtain the *"cirrus path radiance corrected"* apparent reflectance image (index 'cc'):

$$\rho^*_{cc}(\lambda) = \rho^*(\lambda)\ -\ \rho_c(1.38\mu m)\ /\ \gamma \tag{11.6}$$

As the cirrus is almost on top of the atmosphere we have $\rho_c(1.38\mu m) = \rho^*_c(1.38\mu m)$ and the apparent cirrus reflectance can be calculated with eq. 11.1.

For the water vapor band of Sentinel-2 or similar sensors we obtain [102]

$$\rho^*_{cc}(\lambda) = \rho^*(\lambda)\ /\ T_{945}\ -\ \rho_c(1.38\mu m)\ /\ \gamma \tag{11.7}$$

where T_{945} is the two-way (sun-cirrus-sensor) transmittance If a water vapor map is available and the water vapor column is less than a threshold (default W=0.8 cm), the cirrus removal is switched off to avoid a misinterpretation of bright surfaces in the 1.38 μm channel as cirrus.

Note
The calculation of gamma with the scatterplot of the TOA reflectance of the red/cirrus bands is the standard method. The drawback is that the slope is not always well defined. Therefore, a numerically more stable method is used: the value of γ is calculated iteratively in the typical range (0.6 to 1.0) with an increment of 0.05. We define a cirrus class with $\rho^*_c(1.38) > 0.02$ (or $\rho^*_c(1.38) > 0.014$ if less than 10,000 pixels in this class), and a non-cirrus class with $\rho^*_c(1.38) < 0.008$, or $\rho^*_c(1.38) < 0.010$ or $\rho^*_c(1.38) < 0.011$ if not enough pixels. Then the mean value of the DN of 3 bands (around 440, 480, 550 nm) is computed for the cirrus-free areas $DN_{free}(i)$, i=1, 2, 3. It is also computed for the areas in the cirrus class as a function of γ_j, i.e. after cirrus removal $DN_{decirrus}(\gamma_j, i)$ with equation (11.6). Finally, the value of γ_j is selected which minimizes the difference $\Delta(\gamma_j)$:

$$\Delta(\gamma_j) = Min\ \{\ \sum_{i=1}^{3} |\ DN_{free}(i) - DN_{decirrus}(\gamma_j, i)\ |\ \} \tag{11.8}$$

A similar approach is used for the SWIR bands: γ is varied in the range 1 - 2 (values are larger in the SWIR than in the VNIR), increment 0.05, until the absolute difference between the mean

of $|\rho^*(SWIR, cirrus) - \rho_c^*(1.38, cirrus)/\gamma|$ and $\rho^*(SWIR, no - cirrus)$ is less than 3%. If this criterion fails, then the former criterion $\gamma(SWIR) = 2\ \gamma(VNIR)$ is used [102].

Cirrus removal can be conducted as the first step during atmospheric correction, followed by the aerosol, water vapor, and surface reflectance retrievals. If the average water vapor column W of a scene is less than some threshold (default W=0.6 cm) then the cirrus removal algorithm is switched off, to avoid a misinterpretation of bright surfaces as cirrus in the 1.38 μm channel. Normally, atmospheric water vapor completely absorbs surface features in the 1.38 μm channel, but the channel might become partly transparent to surface features for very low water vapor values. This water vapor threshold can be set by the user, see the description of file *'preference_parameters.dat'* in the ATCOR manual.

The file *'xxx_out_hcw.bsq'* (haze, cloud, water) corresponding to a scene *'xxx.bsq'* contains five cirrus classes (thin, medium, thick, cirrus cloud, thick cirrus cloud) for visualization, see the ATCOR manual, but the cirrus removal is independent of the class labeling.

The cirrus and (boundary layer) haze removal options in the ATCOR parameter setting (*"*.inn"*) are exclusive, i.e., only one of them can be selected per ATCOR run. However, the preprocessing batch module *dehaze* or the ATCOR GUI ('ATCOR', 'Haze(HTM)+Cirrus removal') can perform a combined haze/cirrus removal [73] (without aerosol, water vapor, surface reflectance retrievals). Thereafter, the ATCOR run obviously should not use the haze/cirrus removal a second time.

11.2 Elevation-dependent cirrus removal

Beginning with the 2020 release the elevation-dependent cirrus removal is introduced in ATCOR. The standard method of the previous section assumes that the 1.38 μm channel TOA reflectance is exclusively due to cirrus clouds and the ground reflected signal component can be negelected. However, in the case of very low atmospheric water vapor columns and/or high elevations, a certain fraction of the ground reflected radiation will be included in the $\rho^*(1.38\mu m)$ TOA reflectance.

As a compromise for the numerous situations, reference [123] proposes the following second-order polynomial to estimate the ground reflected signal component, see Fig. 11.1:

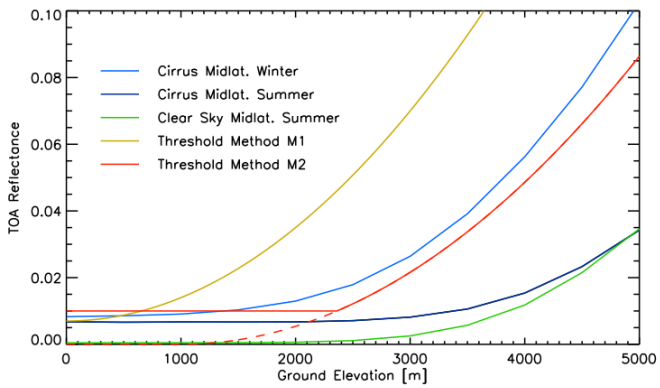

Figure 11.1: *Ground reflected cirrus component as a function of elevation.*

$$\rho^*_{gnd}(1.38) = \left(0.0054 \cdot (h-1)^2\right) > 0.01 \tag{11.9}$$

where h [km] is the pixel elevation taken from a DEM. The horizontal line in Fig. 11.1 indicates that a pixel is only labeled as cirrus if its TOA reflectance exceeds the value 0.01 (to avoid noise and very thin cirrus).
So the cirrus cloud signal applied during the cirrus removal is the 1.38 μm TOA reflectance minus the ground component:

$$\rho^*_{cirrus}(1.38) = \rho^*(1.38) - \rho^*_{gnd}(1.38) \tag{11.10}$$

According to Fig. 11.1 the standard and elevation-dependent cirrus removal differ only for elevations higher than 2.4 km.

Chapter 12

Haze and coupled haze/cirrus removal

In many cases of satellite imagery the scene contains haze and cloud areas. The optical thickness of cloud areas is so high that the ground surfaces cannot be seen, whereas in hazy regions some information from the ground is still recognizable. In ATCOR the scene is partitioned into clear, hazy, and cloud regions. Here we will treat the low altitude boundary layer (0 - 3 km) haze as opposed to high altitude cirrus. Thin boundary layer haze can be detected with broad-band multispectral instruments, while a detection of thin cirrus requires specific narrow bands around 1.38 μm or 1.88 μm, compare chapter 11. As a first approximation, haze is an additive component to the radiance signal at the sensor. It can be estimated and removed as described below. Cloud areas have to be masked to exclude them from haze areas and to enable a successful haze removal.

Two de-hazing algorithms are available in ATCOR: the HOT (Haze Optimized Transform) [146] and the HTM (Haze Thickness Map) [72]. The first approach is restricted to channels in the visible spectrum and is always executed together with the surface reflectance retrieval. It is kept for backward compatibility. Better results are usually obtained with the second method, which is run as an independent preprocessing step, i.e. without surface reflectance retrieval. It works in the spectral region from 0.4 - 2.5 μm. The reflectance retrieval has to be executed as a second step.

12.1 HOT haze removal

The HOT algorithm [146] consists of five major steps:

1. Masking of clear and hazy areas with the tasseled cap (TC) haze transformation [24].

$$TC = x_1 * BLUE + x_2 * RED \tag{12.1}$$

   where BLUE, RED, x_1, and x_2 are the blue band, red band, and weighting coefficients, respectively. The clear area pixels are taken as those pixels where TC is less than the mean value of TC.

2. Calculation of the regression between the blue and red band for clear areas ("clear line" slope angle α). If no blue band exists, but a green spectral band, then the green band is used as a substitute.

3. Haze areas are orthogonal to the "clear line", i.e., a haze optimized transform (HOT) can be defined as

$$HOT = BLUE * sin\alpha - RED * cos\alpha \tag{12.2}$$

4. Calculation of the histogram of HOT for the haze areas.

5. For bands below 800 nm the histograms are calculated for each HOT level j. The haze signal Δ to be subtracted is computed as the DN corresponding to HOT(level j) minus the DN corresponding to the 2% lower histogram threshold of the HOT(haze areas). The de-hazed new digital number is :

$$DN(new) = DN - \Delta \tag{12.3}$$

The HOT works for land pixels, therefore water areas have to be excluded.

12.2 HTM haze removal

Details of the HTM (Haze Thickness Map) algorithm with examples of processing are presented in the paper [72]. An updated description is given here, including improvements that were implemented later.
The haze removal employs a simplified method where the signal in haze affected regions consists of the haze-free scene radiance L_0 and a haze contribution H:

$$L^{sensor} = L_0 + H \tag{12.4}$$

L_0 is the sum of the (haze-free) path radiance and the surface reflected radiance. So the influence of the haze attenuation on the surface reflected radiation is not accounted for.

Assuming a linear relationship of the digital number (DN) to radiance conversion, eq. 12.4 can be written as

$$DN_i^{sensor} = DN_i(x, y) + HTM_i(x, y) \tag{12.5}$$

where (x, y) are the pixel coordinates in the scene, i is the band number, and DN_i is the DN in band i, and $HTM_i(x, y)$ is the haze thickness map in terms of DN. So the haze-free image will be obtained by subtracting $HTM_i(x, y)$ from the recorded DN_i .

Output of the dehaze algorithm is the dehazed scene and in addition a classification map (haze, cirrus, cloud, water, snow/ice, bright object, shadow) named 'scene_haze_map.bsq' if the file name of the input image is 'scene.bsq'.

12.2.1 Haze thickness map HTM

Haze thickness is usually varying over a scene, and the HTM is calculated by searching dark pixels over all of the image. A small to medium ground sampling distance (GSD = 2 - 30 m) allows the recording of dark areas from objects. The corresponding pixels have a very low DN value (small ground reflectance + path radiance), and if haze is present, the recorded DN value is also nonzero and higher than the corresponding haze-free contribution. These nonzero DN values are employed to estimate the HTM of the image. This HTM includes the thickness of haze and of the clear-scene aerosol thickness. The latter part is restored in the final step, and will be taken into account during the atmospheric correction.

The search for dark pixels is conducted with a moving local nonoverlapping window of size $w \times w$ pixels. The small window is used to increase the chance to locate dark pixels in shaded regions. The other pixels in the window are assumed to have the same haze thickness as the thickness estimated for the pixel with the minimal value. A smaller window allows a better estimation of the haze structure and a window size of $w = 3 \times GSD$ is used as default, based on the analysis of different Landsat-8, RapidEye, and Worldview-2 scenes. The selected dark pixels (of minimum value in window size w) are stored in a matrix of size (n/w, m/w) where (n, m) is the size of the original scene. This reduced matrix is median filtered (3×3 pixels) and then resized with cubic interpolation to the original image size.

The presence of large bright objects (bright agricultural fields, sand, rocks, roofs, snow, etc.) causes wrong estimates of the HTM. Therefore, these areas have to be detected and labeled as not appropriate for a HTM evaluation. Earlier versions of the dehaze method used a mean-shift segmentation [21], but faster and better results were obtained with the following apparent reflectance criteria:

$$bright = \rho^*(NIR) \geq 0.3 \quad AND \quad (\rho^*(blue) \geq T_{blue} \quad AND \quad \rho^*(red) \geq T_{red}) \tag{12.6}$$

where $\rho^*(blue)$ is the apparent blue band reflectance (around 0.48 μm) and $\rho^*(red)$ the red band (around 0.66 μm) reflectance, and

$$T_{blue} = \bar{\rho}^*(blue) + 2 \cdot STDEV(\rho^*(blue)) \tag{12.7}$$

$$T_{red} = \bar{\rho}^*(red) + 2 \cdot STDEV(\rho^*(red)) \tag{12.8}$$

If no blue band exists, then the green band is taken as a substitute. Areas labeled as 'bright object' are interpolated in the HTM, using the bilinear (fast) or triangulation (slow) method.

In multispectral data, the search of dark pixels should be performed in a band with a minimal ground reflectance and a maximal haze signal component. A spectral band in the blue region (0.37 - 0.49 μm) is most suitable for this purpose. Spectral bands in the red and near infrared exhibit higher ground reflectance for land and are not suitable.

However, the direct usage of a blue band often leads to overdehazing of this band. To overcome this problem, a new synthetic band is created by a linear extrapolation of the two shortest wavelength bands ($B_1,\ B_2$) :

$$Band_{ext}(x, y) = B_1(x, y) + (B_1(x, y) - 0.95 * B_2(x, y)) \tag{12.9}$$

The surface reflectance in the extrapolated (lower wavelength) band is less, haze thickness is higher, and the HTM can be estimated more precisely. A 3×3 pixel median filter can be applied to remove noise in the extrapolated band.

The quality of the HTM calculation is improved with the use of the extrapolated blue band instead of the sensor-specific blue band. Therefore, the extrapolated blue band is employed for the dark pixel search and the nonoverlapping window size $w = 3$:

$$HTM(x, y) = DARK\_PIXEL\_SEARCH(Band_{ext}(x, y), w) \tag{12.10}$$

Again, the selected dark pixels (within window size $w \times w$) are stored in a matrix of size (n/w , m/w), where (n, m) is the size of the original scene. The reduced matrix is median filtered (3×3

pixels) and then resized with cubic interpolation to the original image size.

It is necessary to label hazy and haze-free regions. For this purpose, a coarse spatial resolution haze mask is created to find haze-free regions. This haze mask is based on the generation of an additional $HTM(w_2)$ with a moderately large window ($GSD * 20$, $w_2 = 21$) and a thresholding of $HTM(w_2)$. This large window $HTM(w_2)$ is only used for the hazy / haze-free labeling and the following threshold T_h is used:

$$T_h = MEAN[HTM(x, y, w_2)] \; + \; h_{sigma} \; \cdot \; STDEV[HTM(x, y, w_2)] \tag{12.11}$$

Pixels are classified as haze-free if

$$HTM(x, y, w_2) < T_h \tag{12.12}$$

otherwise as haze. The default value is $h_{sigma} = 0.3$, but the user can specify this keyword parameter. With $h_{sigma} < 0.3$ more pixels are labeled as haze, with $h_{sigma} > 0.3$ less pixels.
Water bodies are labeled separately, see chapter 2.1.1, they can be included or excluded from dehazing. The haze mask does not necessarily have to be precise, because it is only used to calculate a relative haze thickness coefficient, which is robust to mislabeled outliers.

12.2.2 Haze thickness per band

The optical haze thickness is wavelength-dependent, usually decreasing with wavelength, and channels in the short-wave infrared (SWIR2: 2 - 2.5 μm) are only marginally influenced by haze. Therefore, a channel-dependent HTM_i is computed relative to the HTM using the image $Band_{ext}(x, y)$ (eq. 12.10).
First, a temporary HTM_i' is calculated for each band and the regression coefficient (k_i) of HTM_i' versus HTM_i is stored in an array (**K**). The regression coefficient is computed using the pixels labeled as haze in the haze mask. The k_i sequence should decrease with wavelength, i.e., $k_{i+1} < k_i$. A linear scaling of **K** into the range [1, s] is performed with s=[0.1, 0.15, 0.65] if the last band is [SWIR2, SWIR1, NIR], respectively (SWIR1: 1.65μm).

$$HTM_i'(x, y) = DARK\_PIXEL\_SEARCH(Band_i(x, y), w_3) \tag{12.13}$$

The nonoverlapping window size is $w_3 = 7$ (pixels).

$$k_i = SLOPE(\; HTM(x, y), \; HTM_i'(x, y) \;) \tag{12.14}$$

The final band-specific HTM is

$$HTM_i(x, y) = HTM_i'(x, y) \cdot k_i \tag{12.15}$$

12.2.3 Haze removal

A subtraction of $HTM_i(x, y)$ from the $DN_i^{sensor}(x, y)$ recovers the dehazed band:

$$DN_i(x, y) = DN_i^{sensor}(x, y) - HTM_i(x, y) \tag{12.16}$$

This subtraction removes the calculated haze influence via HTM from the scene. However, the HTM includes the effect of haze plus clear-scene aerosol, and we want to keep the clear-scene aerosol component for the subsequent atmospheric correction. Therefore, we evaluate the mean DN value of the clear areas in the original scene ($M_i^{original}$) and the corresponding mean value in the dehazed scene ($M_i^{dehazed}$) and add the difference :

$$DN_i^{final}(x, y) = DN_i(x, y) + abs(M_i^{original} - M_i^{dehazed}) \tag{12.17}$$

12.2.4 DEM case

The previous considerations are valid for a flat terrain. In case of mountainous regions there are additional problems. For example, high mountain regions (e.g. elevations > 3000 m) are seldom affected by haze. Nevertheless, the proposed dehazing algorithm may erroneously label some of these areas as hazy, because dark pixels can occur due to topographic effects and these will cause misclassifications. If a DEM file is available (in the same folder as the scene) then these high mountain areas can optionally be excluded.

Scenes are frequently contaminated by cirrus clouds, also in mountainous regions. If the image is recorded by a sensor with a cirrus band (around 1.38 μm) then thin and medium optical thickness cirrus clouds are included in the joint dehaze / decirrus algorithm, see chapter 12.2.5. However, for high mountain regions the water vapor column W is usually low. This means the cirrus band radiance is not exclusively of cirrus cloud origin, but also contains a ground reflected signal. Therefore, a water vapor sensitive channel might be an additional useful source of information. But for low water vapor columns (e.g. W < 0.4 cm) the cirrus band can contain a mixture of ground reflected and cirrus radiance.
For sensors with a cirrus band (e.g., Landsat-8/-9, Sentinel-2) an elevation-dependent cirrus removal is performed as described in reference [75].

12.2.5 Joint haze and cirrus removal

The effect of thin and medium optical thickness of cirrus clouds can also be corrected in the dehaze module, provided a narrow bandwidth cirrus channel around 1.38 μm is available, e.g., for Landsat-8 OLI and Sentinel-2.
Of course, cirrus can also be treated with the 'state-of-the-art' approach ([35, 102], compare chapter 11, but then low altitude haze is not included. The advantage of the proposed joint dehaze / decirrus approach [73] is its capability of seamlessly processing scenes containing haze in some areas and cirrus in other parts.

Basically the same steps are conducted as described in the previous sections, i.e., a preclassification, the HTM, the band-specific HTM, and the spatial interpolation over bright object areas. However, with the help of the cirrus channel is is possible to decide if a bright object area is caused by cirrus or if it is really a bright surface on the ground. Therefore, areas mislabeled as bright object (in reality cirrus cloud pixels) can be identified and re-labeled as not belonging to the 'bright object' class to keep the calculated HTM. This means the restoration is conducted with the calculated HTM and not with a spatially interpolated HTM. This is the key factor to improve the accuracy of the dehazed product.

So the 1.38 μm band TOA reflectance is employed to retain the HTM values in bright object areas due to cirrus clouds. The TOA reflectance is calculated as:

$$\rho^*(1.38\mu m) = \frac{\pi \; d^2 \; L^{sensor}}{E \; cos\theta_s}, \tag{12.18}$$

where E is the extraterrestrial solar irradiance, θ_s is the solar zenith angle, and d is the distance earth-sun (Astronomical Units). The following steps are used to include the cirrus information in the general haze proessing algorithm:

- Label bright objects (as before).

- Create the synthetic band extrapolation (eq. 12.9).
- Calculate the HTM (eq. 12.10).
- Read DEM, exclude pixels with DEM > 3000 m from cirrus mask, i.e. $\rho(TOA, 1.38\mu m, h) = 0$ for h > 3000 m.
- Remove pixels with $\rho(TOA, 1.38\mu m) > 0.015$ from the mask of 'bright objects' if they lie in this map and keep the original HTM value. If the cirrus map does not completely overlap the bright map some bright areas still exist and a spatial interpolation of the $HTM(x, y)$ is required.
- Calculate the coarse haze map (eq. 12.12) to locate haze and haze-free pixels.
- Calculate the correlation vector (eq. 12.14).
- Calculate the band-specific HTM (eq. 12.15).
- Perform the decirrus (eq. 11.6, 11.7). Convert the TOA reflectance into the corresponding DN^{decir}.
- Perform the dehazing (eq. 12.16, 12.17), result is DN^{dehaz}.
- If $DN^{decir} < 0.9\ DN^{dehaz}$ then $DN^{final} = \left(DN^{dehaz} + DN^{decir} \cdot 3\right) / 4$
  The weighted contribution of DN^{decir} and DN^{dehaz} to the DN^{final} reduces the amount of overcorrection encountered for the cirrus-only method in regions of thick cirrus clouds. The weight factors are empirical based on the evaluation of Landsat-8 and Sentinel-2 scenes.

The paper [73] presents typical examples of the improved haze/cirrus method and a comparison with methods restricted to either haze removal or cirrus removal.

12.2.6 Special HTM features

The HTM module contains a number of optional keywords, the list can be obtained by just typing 'dehaze' on the IDL command line. As an example, if the keyword *water* is set to 1, then dehazing/decirrus is also performed for water pixels. But it is switched off if overcorrection occurs. For this purpose, atmospheric correction is conducted (red band, water pixels) using a visibility of 40 km, i.e. AOT(550 nm) = 0.20, and if more than 30% of the water pixels have a surface reflectance < 0.01 then the dehaze over water is switched off. Some other features are:

- The preclassification excludes clouds, snow/ice, and bright pixels from being labeled as haze.
- The accuracy of the dehaze map to classify water pixels is improved if DEM data (slope) is available. If the file name of the scene is 'scene.bsq' or 'scene.tif', then the elevation and slope files should be 'scene_ele.bsq' and 'scene_slp.bsq'. Other file names are also accepted, if they are specified in the 'scene.inn'. Water pixels are first classified with spectral criteria, in addition the DEM slope must be smaller than 3°.
- Sentinel-2 cube of the 10m data: the cirrus information of the 20m/60m data is used.
- Sentinel-2 cube of the 10m data: the DEM slope map of the 20m slope (resampled to 10m) is used.

12.2.7 HTM for hyperspectral imagery

The HTM method was originally developed for multispectral data. Later improvements also support hyperspectral imagery. In this case 12 reference wavelengths are defined (0.424, 0.440, 0.480, 0.560, 0.660, 0.740, 0.850, 1.000, 1.090, 1.640, 2.200, 2.400 μm), and the band-specific HTM is calculated for the nearest hyperspectral center wavelength. If a channel near 0.424 μm is available, but rather noisy, then the keyword b440 = 1 can be set in program *dehaze* to use the 440 nm band for the haze thickness calculation. HTM maps for the other channels are obtained with interpolation or extrapolation, which is sufficient, because the band-dependent HTM maps change slowly with wavelength.

Chapter 13

Removal of shadow effects

13.1 Matched filter

Remotely sensed optical imagery of the Earth's surface is often contaminated with cloud and cloud shadow areas. Surface information under cloud covered regions cannot be retrieved with optical sensors, because the signal contains no radiation component being reflected from the ground. In shadow areas, however, the ground-reflected solar radiance is always a small non-zero signal, because the total radiation signal at the sensor contains a direct(beam) and a diffuse (reflected skylight) component. Even if the direct solar beam is completely blocked in shadow regions, the reflected diffuse flux will remain. Therefore, an estimate of the fraction of direct solar irradiance for a fully or partially shadowed pixel can be the basis of a compensation process called de-shadowing or shadow removal. Reference [96] describes a method based on the matched filter technique to eliminate shadow areas cast by clouds or buildings.

The proposed de-shadowing technique works for multispectral and hyperspectral imagery over land acquired by satellite / airborne sensors. The method requires a channel in the visible and at least one spectral band in the near-infrared (0.8-1 μm) region, but performs much better if bands in the short-wave infrared region (around 1.6 and 2.2 μm) are available as well. A fully automatic shadow removal algorithm has been implemented. However, the method involves some scene-dependent thresholds that might have to be optimized during an interactive session. In addition, if shadow areas are concentrated in a certain part of the scene, say in the lower right quarter, the performance of the algorithm improves by working on a smaller subset of the scene.

The method starts with a calculation of the surface reflectance image cube $\rho_i = \rho(\lambda_i)$, where three spectral bands around $\lambda_i = 0.85$, 1.6, and 2.2 μm are selected. These bands from the near and shortwave infrared region are very sensitive to cloud shadow effects, because the direct part of the downwelling solar radiation flux at the ground level is typically 80% or more of the total downwelling flux. Channels in the blue-to-red region (0.4-0.7 μm) are not used for the detection of shadow regions because they receive a much larger diffuse radiation component,making them less sensitive to partial shadow effects.

The surface reflectance $\rho(\lambda_i)$ with bands near $\lambda_i = 0.85,\ 1.6,\ 2.2\ \mu m$ is first computed with the assumption of full solar illumination, excluding water and clouds Then the covariance matrix $C(\rho)$ is calculated, where ρ is the surface reflectance vector of the previously selected three bands. The

matched filter is a vector tuned to a certain target reflectance spectrum ρ_t to be detected

$$V_{mf} = \frac{C^{-1}(\rho_t - \bar{\rho})}{(\rho_t - \bar{\rho})^T C^{-1}(\rho_t - \bar{\rho})} \tag{13.1}$$

where $\bar{\rho}$ is the scene-average spectrum, without the water/cloud pixels. Selecting $\rho_t = 0$ for a shadow target yields a special simplified form of the matched filter, where the 'sh' index symbolizes shadow:

$$V_{sh} = -\frac{C^{-1}\bar{\rho}}{\bar{\rho}^T C^{-1}\bar{\rho}} \tag{13.2}$$

The shadow matched filter vector is then applied to the non-water/non-cloud part of the scene and yields the still un-normalized values ϕ that are a relative measure of the fractional direct illumination, also called *unscaled shadow function* here:

$$\Phi(x, y) = V_{sh}^T(\rho(x, y) - \bar{\rho}) \tag{13.3}$$

The matched filter calculates a minimum RMS shadow target abundance for the entire (non-water/non-cloud) scene. Therefore, the values of Φ are positive and negative numbers. The arbitrary, image-depending range of Φ has to be rescaled to the physical range from 0 to 1, where 0 indicates no direct illumination (full shadow), and 1 means full direct illumination. The histogram of Φ is used to rescale the image data. Fig. 13.1 shows a schematic sketch of such a histogram with a smaller peak (at Φ_2) representing the shadow pixels and the main peak (at Φ_{max}) representing the majority of the fully illuminated areas. The statistical assumption is used that full direct solar illumination is already obtained for pixels with $\Phi(x, y) = \Phi_{max}$. Then the values Φ are linearly mapped from the unscaled (Φ_{min}, Φ_{max}) interval onto the physically scaled (0,1) interval, where the *scaled shadow function* is named Φ^*:

$$\Phi^* = \frac{\Phi - \Phi_{min}}{\Phi_{max} - \Phi_{min}} \qquad if \quad \Phi \leq \Phi_{max} \tag{13.4}$$

$$\Phi = 1 \qquad if \quad \Phi > \Phi_{max} \tag{13.5}$$

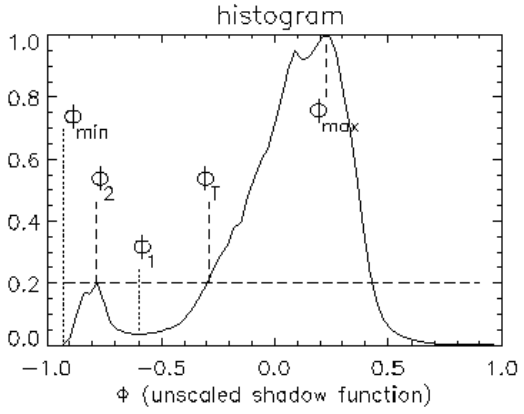

Figure 13.1: *Normalized histogram of unscaled shadow function.*

The smallest value of the scaled shadow function is $\Phi^*_{min} = 0$, which means no direct illumination. However, to avoid overcorrection and to cope with scenes containing merely partial shadow areas,

it is advisable to set Φ^*_{min} at a small positive value. This value of Φ^*_{min}, i.e., the minimum fractional direct illumination (deepest shadow in a scene, typically ranging between 0.05 and 0.10) is scene-dependent. Therefore, it can be defined the user during an interactive GUI session.

In principle, the de-shadowing could now be performed with the physically scaled function Φ^*, which represents the fraction of the direct illumination for each pixel in the ρ vector,i.e., the complete scene without cloud and water pixels. However, since the matched filter is not a perfect shadow transformation, it is much better to restrict its application to the potential, most-likely shadow areas. This is an important processing step to reduce the number of mis-classifications or false-alarms. If omitted, it will cause strange 'shadow' pixels scattered all over the image. Therefore, the proposed method tries to find the core shadow areas in a scene, and subsequently expands the core regions to obtain the final mask that includes a smooth shadow/clear transition. The physically scaled shadow function Φ^* is then applied only to the pixels in the final mask.

The histogram of the unscaled shadow function Φ can be employed to separate regions of low values of Φ from the moderate-to-high values, compare Fig. 13.1. A threshold Φ_T can be set in the vicinity of the local histogram minimum (Φ_1) and the core shadow mask is defined by those pixels with $\Phi(x, y) < \Phi_T$. As always with thresholding, some arbitrariness is involved in the final choice, and the user can tune it in the interactive session. Once the core shadow mask has been defined, it is expanded to include the surrounding shadow / clear transition zone of 100 m width. De-shadowing with the scaled shadow function Φ^* is then exclusively applied to the pixels in this final mask. The means the direct solar flux on the ground E_{dir} is multiplied with the pixel-dependent $\Phi^*(x, y)$, reducing the direct solar term, thus increasing the brightness of a shadow pixel, since E_{dir} $\Phi^*(x, y)$ is in the denominator of the reflectance equation.

$$\rho_i(x, y) = \frac{\pi(d^2\{c_0(i) + c_1(i)DN_i(x, y)\} - L_{p,i})}{\tau_i\{E_{dir,i}\Phi^*(x, y) + E_{dif,i}\}} \tag{13.6}$$

Fig. 13.2 contains the flow chart of the MF de-shadowing and Fig. 13.3 shows an example of de-shadowing a subset of an airborne HyMap scene acquired near Chinchon, Spain, July 12, 2003.

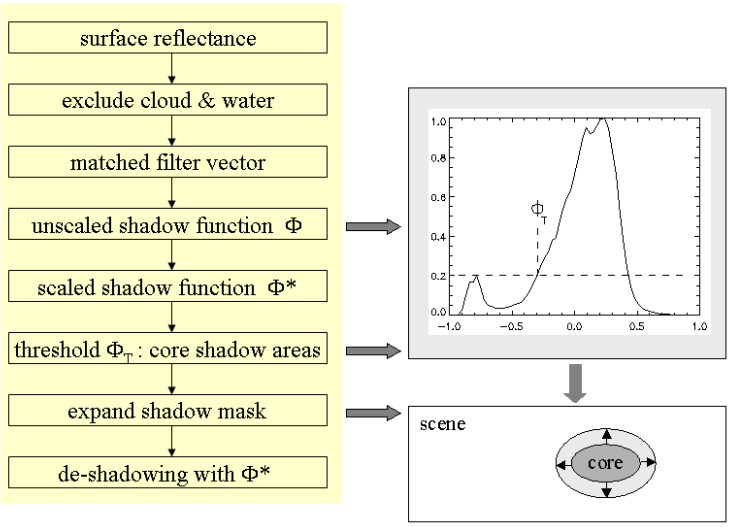

Figure 13.2: *Flow chart of the 'Matched Filter' de-shadowing.*

The matched filter algorithm works best in the interactive mode, because three parameters have to be optimized, see the corresponding GUI in the ATCOR User Guide [104, 105]. In addition, it is often necessary to work on a smaller subset image, because the histogram peak Φ_2 of the shadow pixels (see Fig. 13.1) may not show in a large scene with a small percentage of shadow pixels.

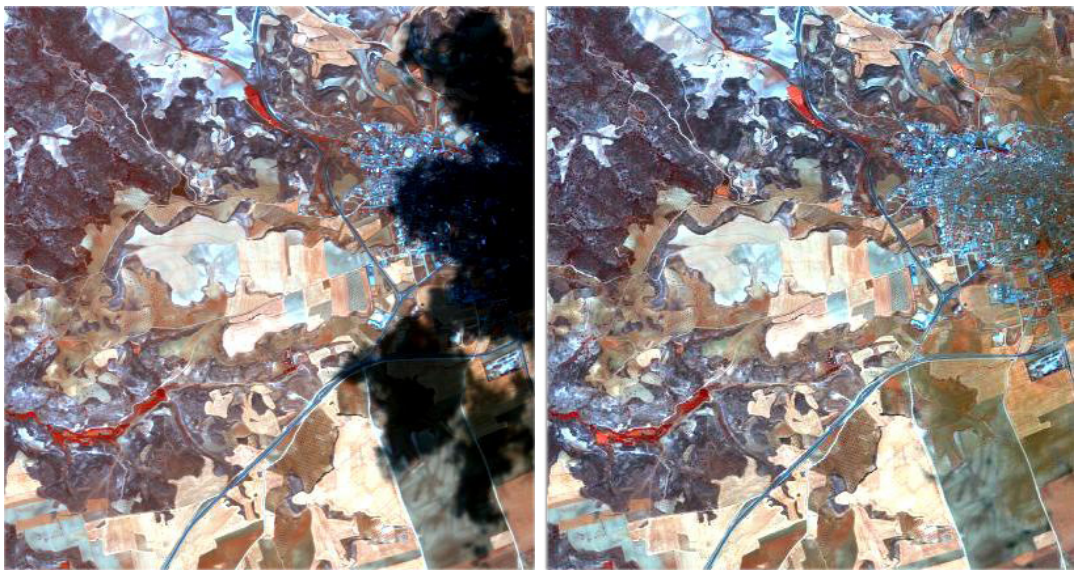

Figure 13.3: *Left: HyMap scene (RGB = 878/646/462 nm), right: after matched filtering.*

13.2 Illumination approach (high spatial resolution)

For high resolution imagery, the correction of cast shadows and illumination on the basis of a surface model does not lead to useful results as the surface representation with respect to the radiometry is never accurate enough. Severe over- and under-correction artifacts are observed due to these inaccuracies in the resulting images.

The detection and correction of cast shadows has been widely studied, specifically for space borne high resolution instruments [3, 125]. An index-based method for cast shadow detection has been implemented in ATCOR [121]. It produces a continuous shadow field and relies on the fact that all areas in cast shadows are illuminated by diffuse irradiance only. The diffuse illumination is caused by scattering and thus exhibits very specific spectral characteristics if compared to the direct irradiance. Specifically, the signal in the blue spectral band is significantly higher in cast shadow areas than in directly illuminated areas. For the shadow quantification, the brightness in the NIR spectral band is first calculated using the solar illumination. Secondly, two blue indices have been defined as the band ratios green/blue and red/blue, respectively. These three measures are combined such that a value equivalent to the illumination between 0 and 1 is created (0 being a cast shadow area), see an example in Fig. 13.4..

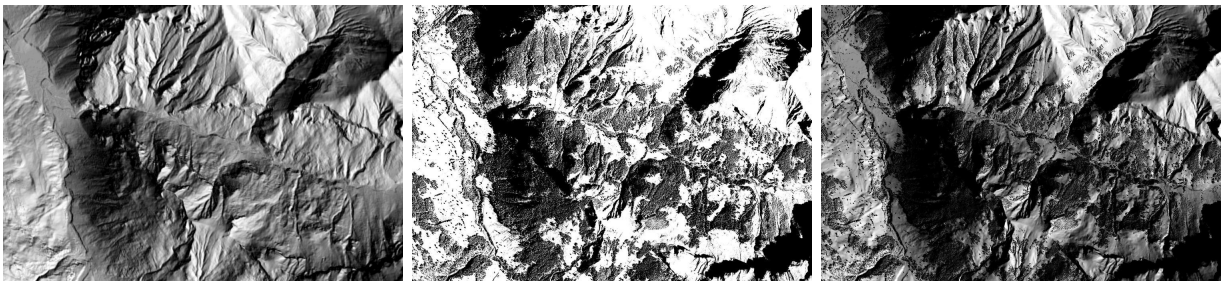

Figure 13.4: *Combination of illumination map (left) with cast shadow fraction (middle) into continuous illumination field (right).*

13.2.1 Shadows over land

The shadow fraction f_{sh} parameter is now calculated from this red-to-blue spectral feature. The respective apparent reflectance values are used as input. They are simply named ρ_b, ρ_g, ρ_r, and ρ_n for the blue, green, red, and NIR spectral bands, respectively. In a first step, the ratio between the red and the blue spectral band is calculated. This index increases with the portion of direct illumination: low index values show shadow areas whereas high values are directly illuminated pixels. The blue apparent reflectance is corrected to account for the influence of chlorophyll absorption, using the positive difference in apparent reflectance between NIR and red $(\rho_n - \rho_r)_{>0}$. Setting the minimum of this correction factor to zero inhibits its unintended application to non-vegetated pixels.

$$i_{sh} = \frac{\rho_r + k_n \cdot (\rho_n - \rho_r)_{>0}}{\rho_b}. \tag{13.7}$$

The empirical factor k_n is used to weight the vegetation correction factor. It is derived by minimizing the variation of i_{sh} of eq. 13.7 depending on surface cover types, using the spectra of

the above-mentioned simulated data set. An optimal value of $k_n = 0.1$ has been found from this analysis.
When calculating the index from eq. 13.7 for various aerosol amounts, a systematic decrease of the index value with increasing aerosol amounts is observed. This can be accounted for by using dark object signatures in the blue, which are mainly ruled by aerosol scattering. The dark signature $\rho_{b,dark}$ for the blue band is found from the image by using the average apparent reflectance of the darkest pixels in the image from 0.1% of all image pixels (this percentile is increased to 1% for small images). Relating these dark object signatures, an aerosol-amount-dependent trend can be found and applied to the index as a normalization function such that the shading index for land surfaces may be written as:

$$i_{lsh} = \frac{\rho_r + k_n \cdot (\rho_n - \rho_r)_{>0}}{\rho_b} \cdot \frac{1}{a \cdot e^{b \cdot \rho_{b,dark}}}. \tag{13.8}$$

The parameters a and b from the correction function are found by an exponential fit between $\rho_{b,dark}$ and the raw index i_{sh} on all spectra of the simulated data set, using three sensor altitudes (2km, 5km, and satellite level). Values of $a = 1.58$ and $b = -0.04$ have been found leading to the lowest variation of i_{lsh} with respect to the visibility. The relative deviation from the mean of the index derived from the full set of reference spectra as described above with the full variation of visibilities could be reduced from 32% to 14% by applying this correction. Applying eq. 13.8 with optimized correction parameters to the simulated data leads to a more stable average index.

13.2.2 Shadows over water

The above index is applicable for most land situations, but it can not be used to derive shadows over water bodies. Specific methods have to be developed to find shaded areas over water in order to exclude false alarms in water. Using the red-blue ratio does not allow for a successful shadow detection over water. The blue appearance of water reflectances is interfering with the aerosol signatures in this wavelength range and needs to be accounted for. It has been found that an extrapolation of the signatures in the green-red bands towards the blue spectral range is a good alternative to find a shadow-sensitive index for water bodies. A corresponding index is calculated as a relation between an extrapolated blue signature to the measured blue apparent reflectance, while both parameters are corrected by subtracting the blue dark objects signature:

$$i_{wsh,0} = \frac{\rho_{b,ext} - \rho_{b,dark,ext}}{\rho_b - \rho_{b,dark,ext}}, \tag{13.9}$$

where

$$\rho_{b,ext} = \rho_g - \frac{\rho_r - \rho_g}{\lambda_r - \lambda_g} \cdot (\lambda_g - \lambda_b). \tag{13.10}$$

The dark object signature for the blue band can not be taken from the blue band directly as the natural blue reflectance of water may be quite high. Therefore, this signature $\rho_{b,dark,ext}$ is estimated as a weighted combination between the blue dark signature and the red dark signature as:

$$\rho_{b,dark,ext} = 0.8 \cdot \rho_{r,dark} + 0.2 \cdot \rho_{b,dark} \tag{13.11}$$

It has been found that the index depends mainly on flight altitude rather than on aerosol optical thickness, which may be explained by the relation between atmospheric path radiance and diffuse ground irradiance which changes with altitude. An exponential decrease of the index value with

flight altitude h has been derived from the simulated data set which can be used for a height-dependent index equation as:

$$i_{wsh} = \frac{i_{wsh,0}}{a \cdot e^{-bh}}. \tag{13.12}$$

The values of the exponential function are derived from the simulated data as $a = 1.18$ and $b = -0.4\ km^{-1}$. The flight altitude h is given in km.

13.2.3 Shadow index combination

The indices can be combined based on a land/water mask. The water mask is derived by a classification rule which uses the following threshold values:
$[(\rho_n < (\rho_{nir,dark} + 1\%)$ AND $(\rho_r - \rho_b < -3\%)$ AND $(\rho_n - \rho_r < 3\%)]$
OR $[\ (2 \cdot \rho_g > (\rho_r + \rho_n) + 4\%)$ AND $(\rho_n < 7\%)]$.
Using a transition range of 1% for each reflectance threshold, a smooth weighting factor w between water ($w = 0$) and land surfaces ($w = 1$) is derived. Offsets are applied to both indices to place them in a range between 0 and 1 such that $i'_{lsh} = (i_{lsh} - 0.3) > 0 < 1$ and $i'_{wsh} = (i_{wsh} - 0.6) > 0$. The two re-scaled indices are then combined into one layer for later use in image analysis:

$$i_{sh} = w \cdot i'_{lsh} + (1 - w) i'_{wsh}. \tag{13.13}$$

The parameter i_{sh} is finally scaled to a shadow fraction f_{sh} between 0 (full cast shadow) and 1 (no cast shadow) using a lower limit for full cast shadow areas and an upper limit for full illumination. It has been found that the lower limit of i_{sh} has to be set to values between 0.3 and 0.55. This threshold depends on the instrument spectral response, the radiometric calibration accuracy of the instrument, and also on the average flight altitude.
In desert areas where no water is expected, the detection of shadows on water is not useful and may lead to erroneous results. Therefore, a simplified mode without the second index is applied in such situations by setting the parameter w to one. A sample of the whole cast shadow detection process is illustrated in Figure 13.5. The indices for land and water are calculated and then combined into one fractional shadow value using the water mask. Application of a final threshold leads to the cast shadow mask.

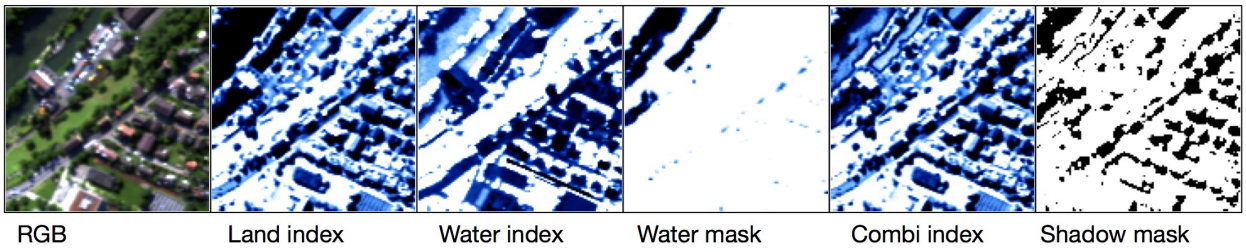

Figure 13.5: *Derivation of cast shadow mask from original image by calculating land index, water index, water mask, a combination of both and applying a threshold of 0.33 to the output. The indices (in blue) are linearly scaled between 0.2 and 0.6 in this sample.*

For topographic correction in the ATCOR software, the direct illumination on an image pixel is scaled by the cosine of the local solar incidence angle $cos(\beta)$ which is typically derived from digital elevation data. As the image derived shadow fraction f_{sh} is also related to the direct illumination,

it can be combined with the incidence angle in an illumination factor f_{ilu} as the smaller value of both factors per image pixel:

$$f_{ilu} = \min\left[f_{sh}; \cos(\beta)\right]. \tag{13.14}$$

This fractional illumination factor may now be used for correction of illumination effects in the atmospheric compensation routine, for cast shadow correction, but also for aerosol detection as described hereafter.

13.2.4 Skyview factor estimate

The skyview factor V_{sky} describes the relative amount of the unobstructed sky hemisphere. This factor is highly variable on small scales, e.g., in vicinity of forest borders. The skyview factor is approximated from the cast shadow fraction such that all areas in complete cast shadows get a reduced skyview factor as:

$$V_{sky} = (1 - \frac{\theta_s}{180°} + f_{shad}\frac{\theta_s}{180°}) \cdot 100\% < V_{sky,geom}, \tag{13.15}$$

where θ_s is the solar zenith angle and the geometrical skyview factor $V_{sky,geom}$ had been calculated based solely on the digital terrain model.

13.2.5 Application in ATCOR workflow

In ATCOR, the local illumination angle φ is first calculated on the basis of the terrain model using an efficient vector algebra. The topographically and shadow corrected reflectance ρ_{topo} is then retrieved from the atmospherically corrected ground leaving excitance (M_g, derived from first order atmospheric compensation) using the atmospherically transmitted direct irradiance $E_{dir,t}$, the diffuse illumination field $E_{dif,t}$, the terrain illumination E_{ter}, and the shadow fraction f_{shad}, as:

$$\rho_{topo} = \frac{M_g}{f_{shad}\ E_{dir,t}cos(\varphi) + \overline{\rho_0}\ E_{dif,t} + E_{dif,t}\ ((1-\tau_s)V_{sky} + \tau_s\ f_{shad}\frac{cos(\varphi)}{/}cos(\theta_s)}, \tag{13.16}$$

The local illumination factor $cos(\varphi)$ is now enhanced by the cast shadow fraction, such that shaded areas are corrected accounting for direct and circumsolar irradiance, see an example in Fig. 13.6. After cast shadow correction, the border pixels of the shadows are often under/overcorrected, which is visible as black or bright borders in the cast shadow areas. A filter has to be applied to remove this artifact (compare Fig. 13.7). A simple approach to this problem is an interpolation of all border pixels. However, a considerable data loss may be the result of such a process. Thus a more sophisticated approach is required. As the border pixels are usually isolated, a filter approach has been used which compares the pixel brightness $\overline{\rho_{i,j}}$ to the brightness of its direct neighbors $\overline{\rho_{prox}}$ in a 3x3 or 5x5 box, respectively. The brightness of the shadow border pixel is then adjusted by the relative brightness difference of the whole spectrum such that:

$$\rho_{filt,i,j} = \rho_{i,j}\frac{\overline{\rho_{prox}}}{\overline{\rho_{i,j}}}. \tag{13.17}$$

This method proved to successfully remove shadow borders for high resolution imagery and an urban environment. However, for terrain shadows on a larger scale, the border pixels are not such clearly isolated and often can not be corrected using this method, or only after increasing the size of the border pixel filter significantly.
The updated processing leads to improved terrain correction as displayed in Fig.13.6. Advantages of this method are:

Figure 13.6: *Effect of combined topographic / cast shadow correction: left: original RGB image; right: corrected image (data source: Leica ADS, central Switzerland 2008, courtesy of swisstopo).*

- terrain and forest cast shadows are corrected,
- water and cast shadows are discerned (in most cases),
- operational usability has been proven on large ADS data sets, and
- a consistent physically based method is available for photogrammetry and imaging spectroscopy applications.

Figure 13.7: *Left to right: original scene, cast shadow correction, and shadow border removal for building shadows.*

Chapter 14

Miscellaneous

This chapter treats several diverse topics that are not easily in line with the other chapters. The first topic is the spectral calibration of hyperspectral imagery using spectral absorption regions of atmospheric gases. The next one presents the radiometric calibration. The third topic is value added products that can be derived after atmospheric compensation.

14.1 Spectral calibration using atmospheric absorption regions

Surface reflectance spectra retrieved from narrow-band hyperspectral imagery often contain spikes and dips in spectral absorption regions of atmospheric gases (e.g., oxygen absorption around 760 nm, water vapor absorption around 940 nm). These effects are most likely caused by a spectral miscalibration. In this case, an appropiate shift of the center wavelengths of the channels will remove or at least reduce the spikes. This is performed by an optimization procedure that minimizes the deviation between the surface reflectance spectrum and the corresponding smoothed spectrum. The merit function to be minimized is

$$\chi^2(\delta) = \sum_{i=1}^{n} \{\rho_i^{surf}(\delta) - \rho_i^{smooth}\}^2 \tag{14.1}$$

where $\rho_i^{surf}(\delta)$ is the surface reflectance in channel i calculated for a spectral shift δ, ρ_i^{smooth} is the smoothed (low pass filtered) reflectance, and n is the number of bands in each spectrometer of a hyperspectral instrument. So the spectral shift is calculated independently for each spectrometer. In the currently implemented version, the channel bandwidth is not changed and the laboratory values are assumed valid. More details of the method are described in [42]. A spectral re-calibration should precede any radiometric recalibration. The ATCOR User Guide [104, 105] contains the respective GUI and explains how to handle this module.

14.2 Radiometric calibration using ground reference targets

Radiometric calibration using ground reference targets can be performed for broad-band multispectral as well as narrow-band hyperspectral imagery. This approach is also named 'vicarious calibration' or 'inflight calibration'. The surface reflectance of uniform targets is measured with a field spectro-radiometer, and the targets should have a sufficiently large size compared to the sensor footprint (at least 7 times larger). In addition, the main atmospheric parameters (aerosol

content, water vapor) are usually measured simultaneously with the satellite/airborne overflight [128, 111, 91]
In the simplest case, when the offset is zero ($c_0 = 0$), a single target is sufficient to determine the calibration coefficient c_1 relating the Digital Number DN to the at-sensor radiance L_1:

$$L_1 = c_1 DN_1^* = L_{path} + \tau \rho_1 E_g / \pi \tag{14.2}$$

L_{path} , τ, and E_g are taken from the appropriate LUT's of the atmospheric database, ρ_1 is the measured ground reflectance of target 1, and the channel or band index is omitted for brevity.
DN_1^* is the digital number of the target, averaged over the target area and already corrected for the adjacency effect. Solving for c_1 yields:

$$c_1 = \frac{L_1}{DN_1^*} = \frac{L_{path} + \tau \rho_1 E_g / \pi}{DN_1^*} \tag{14.3}$$

Remark: a bright target should be used here, because for a dark target any error in the ground reflectance data will have a large impact on the accuracy of c_1.

In case of two targets a bright and a dark one should be selected to get a reliable calibration and solve for the two unknowns c_0 and c_1.
In cases where n > 2 targets are available the calibration coefficients can be calculated with a least squares fit applied to a linear regression equation. This is done by the "cal_regress" program of ATCOR, compare the corresponding section in the User Guide [104, 105].

14.3 Value Added Products

As a "by-product" of atmospheric correction a number of useful quantities can readily be calculated. The first group of value added products in ATCOR include vegetation indices (based on surface reflectance instead of at-sensor radiance), simple parametrizations of the leaf area index, and wavelength-integrated reflectance (albedo). The second group comprises quantities relevant for surface energy balance investigations which are a useful supplement for studies in landscape ecology and related fields, e.g., as input for regional modeling of evapotranspiration. These include global radiation on the ground, absorbed solar radiation, net radiation, and heat fluxes. Emphasis is put on simple models based on the reflectance / temperature cube derived during the atmospheric correction. No additional data (with the exception of air temperature) is taken into account. All value added products are written to a file with up to 11 bands. The file structure is band sequential. If the input file name is "example.bsq", the output reflectance file name is "example_atm.bsq", and the value added file name is "example_atm_flx.bsq", the 'flx' indicating the most important part of the calculation, i.e., the radiation and heat fluxes.

14.3.1 LAI, FPAR, Albedo

Many vegetation indices have been introduced in the literature. Only two are presented here, because these are often used for simple parametrizations of the leaf area index (LAI), the fraction of absorbed photosynthetically active radiation (FPAR), and surface energy fluxes ([6, 17]. The normalized difference vegetation index (NDVI) is defined as

$$NDVI = \frac{\rho_{850} - \rho_{650}}{\rho_{850} + \rho_{650}} \tag{14.4}$$

where ρ_{650} and ρ_{850} are surface reflectance values in the red (650 nm) and NIR (850 nm) region, respectively. The soil-adjusted vegetation index (SAVI) is defined as [49, 6] with L = 0.5 :

$$SAVI = \frac{(\rho_{850} - \rho_{650}) * 1.5}{(\rho_{850} + \rho_{650} + 0.5)} \tag{14.5}$$

The leaf area index (LAI) can often be approximated with an empirical three-parameter relationship employing a vegetation index (VI=SAVI or VI=NDVI)

$$VI = a_0 - a_1 \; exp(-a_2 \; LAI) \tag{14.6}$$

Solving for LAI we obtain

$$LAI = -\frac{1}{a_2} \; ln(\frac{a_0 - VI}{a_1}) \tag{14.7}$$

Sample sets of parameters are a_0=0.82, a_1=0.78, a_2=0.6 (cotton with varied soil types), a_0=0.68, a_1=0.50, a_2=0.55 (corn), and a_0=0.72, a_1=0.61, a_2=0.65 (soybean) with VI=SAVI [17]
Note: Since it is difficult to take into account the parameters for different fields and different seasons it is suggested to use a fixed set of these three parameters for multitemporal studies. Then, the absolute values of LAI may not be correct, but the seasonal trend can be captured.

Plants absorb solar radiation mainly in the 0.4 - 0.7 μm region, also called PAR region (photosynthetically active radiation, ASRAR 1989). The absorbed photosynthetically active radiation is called APAR, and the fraction of absorbed photosynthetically active radiation is abbreviated as FPAR. These terms are associated with the green phytomass and crop productivity. A three-parameter model can be employed to approxiate APAR and FPAR [4, 5, 141, 142].

$$FPAR = C[1 - A \; exp(-B \; LAI)] \tag{14.8}$$

Typical values are C=1, A=1, B=0.4. Again, since it is difficult to account for the crop- and seasonal dependence of these parameters, a constant set may be used for multitemporal datasets to get the typical FPAR course as a function of time.

The wavelength-integrated surface reflectance (in a strict sense the *hemispherical - directional reflectance*) weighted with the global flux on the ground E_g is used as a substitute for the surface albedo (*bi-hemispherical reflectance*). It is calculated as :

$$a = \frac{\int_{0.3\mu m}^{2.5\mu m} \rho(\lambda) E_g(\lambda) d\lambda}{\int_{0.3\mu m}^{2.5\mu m} E_g(\lambda) d\lambda} \tag{14.9}$$

Since most satellite sensors cover only part of the 0.3 - 2.5 μm region the following assumptions are being made for extrapolation. Extrapolation for the 0.30-0.40 μm region:

- $\rho_{0.3-0.4\mu m} = 0.8 \; \rho_{0.45-0.50\mu m}$, if blue a band (0.45-0.50 μm) exists.
- $\rho_{0.3-0.4\mu m} = 0.8 \; \rho_{0.52-0.58\mu m}$, green band, no blue band available.

Extrapolation for the 0.40-0.45 μm region:

- $\rho_{0.4-0.45\mu m} = 0.9 \; \rho_{0.45-0.50\mu m}$, if a blue band (0.45-0.50 μm) exists.

- $\rho_{0.4-0.52\mu m} = 0.9\ \rho_{0.52-0.58\mu m}$, green band, no blue band available.

The reflectance reduction factors in the blue part of the spectrum account for the decrease of surface reflection for most land covers (soils, vegetation). The extrapolation to longer wavelengths is computed as:

- If a 1.6 μm band exists
  - $\rho_{2.0-2.5\mu m} = 0.5\ \rho_{1.6\mu m}$, if $\rho_{850}/\rho_{650} > 3$ (vegetation)
  - $\rho_{2.0-2.5\mu m} = \ \rho_{1.6\mu m}$, else
- If no bands at 1.6 μm and 2.2 μm are available the contribution for these regions is estimated as :
  - $\rho_{1.5-1.8\mu m} = 0.50\ \rho_{0.85\mu m}$, if $\rho_{850}/\rho_{650} > 3$ (vegetation)
  - $\rho_{2.0-2.5\mu m} = 0.25\ \rho_{0.85\mu m}$, if $\rho_{850}/\rho_{650} > 3$
  - $\rho_{1.5-1.8\mu m} = \rho_{0.85\mu m}$, (else)
  - $\rho_{2.0-2.5\mu m} = \rho_{0.85\mu m}$, (else)

At least three bands in the green, red, and near-infrared are required to derive the albedo product. Wavelength gap regions are supplemented with interpolation. The contribution of the 2.5 - 3.0 μm spectral region can be neglected, since the atmosphere is almost completely opaque and absorbs all solar radiation. The output "_flx" file contains the channels SAVI, LAI, FPAR, and albedo coded as 16 bit integer with the following scale factors:

- SAVI: range 0-1000, scale factor 1000, e.g., scaled SAVI=500 corresponds to SAVI=0.5 .
- LAI : range 0-10,000, scale factor 1000, e.g., scaled LAI=5000 corresponds to LAI=5.0 .
- FPAR: range 0-1000, scale factor 1000, e.g., scaled FPAR=500 corresponds to FPAR=0.5 .
- Albedo: range 0-1000, scale factor 10, e.g., scaled albedo=500 corresponds to albedo=50% .

The next section presents a simplified treatment of the radiation and heat fluxes in the energy balance.

14.3.2 Surface energy balance

Surface energy balance is an essential part of climatology. The energy balance equation applicable to most land surfaces can be written as [5]:

$$R_n = G\ +\ H\ +\ LE \tag{14.10}$$

where, R_n is the net radiant energy absorbed by the surface. The net energy is dissipated by conduction into the ground (G), convection to the atmosphere (H) and available as latent heat of evaporation (LE). The amount of energy employed in photosynthesis in case of vegetated surfaces is usually small compared to the other terms. Therefore, it is neglected here.
The terms on the right hand side of equation (14.10) are called heat fluxes. The soil or ground heat flux (G) typically ranges from 10% to 50% of net radiation. Convection to the atmosphere is called sensible heat flux (H). It may warm or cool the surface depending on whether the air is warmer or cooler than the surface. The energy available to evaporate water from the surface (LE) is usually

obtained as the residual to balance the net radiation with the dissipation terms. Net radiation is expressed as the sum of three radiation components:

$$R_n = R_{solar} \; + \; R_{atm} \; - \; R_{surface} \tag{14.11}$$

where R_{solar} is the absorbed shortwave solar radiation (0.3 - 3 μm, or 0.3 - 2.5 μm), R_{atm} is the longwave radiation (3 - 14 μm) emitted from the atmosphere toward the surface, and $R_{surface}$ is the longwave radiation emitted from the surface into the atmosphere. Downwelling radiation is counted with a positive sign, the upwelling thermal surface radiation has a negative sign. The absorbed solar radiation can be calculated as :

$$R_{solar} = \int_{0.3\mu m}^{2.5\mu m} \{1 - \rho(\lambda)\} \; E_g(\lambda) \; d\lambda \tag{14.12}$$

where $\rho(\lambda)$ is the ground reflectance, $1-\rho(\lambda)$ is the absorbed fraction of radiation, and $E_g(\lambda)$ is the global radiation (direct and diffuse solar flux) on the ground. The numerical calculation of equation (14.12) is based on the same assumptions regarding the extrapolation of bands and interpolation of gap regions as discussed in chapter 14.3.1 dealing with the surface albedo. If the satellite imagery contains no thermal band(s) from which a map of ground temperature can be derived, then R_{solar} is the only surface energy component that can be evaluated. In case of flat terrain with spatially varying visibility conditions or rugged terrain imagery, a map of the global radiation is included as an additional value added channel.

$$E_g = \int_{0.3\mu m}^{2.5\mu m} E_g(\lambda) \; d\lambda \tag{14.13}$$

For flat terrain imagery with constant atmospheric conditions the global radiation is a scalar quantity and its value can be found in the "*log" file accompanying each output reflectance file. For rugged terrain imagery, the global radiation accounts for the slope/aspect orientation of a DEM surface element.

With thermal bands a ground temperature or at least a ground brightness temperature image can be derived. Then the emitted surface radiation is calculated as

$$R_{surface} = \epsilon_s \; \sigma \; T_s^4 \tag{14.14}$$

where ϵ_s is the surface emissivity, $\sigma = 5.669 \times 10^{-8} \; Wm^{-2}K^{-4}$ is the Stefan-Boltzmann constant, and T_s is the kinetic surface temperature. For sensors with a single thermal band such as Landsat TM an assumption has to be make about the surface emissivity to obtain the surface temperature. Usually, ϵ_s is selected in the range 0.95 - 1, and the corresponding temperature is a brightness temperature. A choice of $\epsilon_s = 0.97$ or $\epsilon_s = 0.98$ is often used for spectral bands in the 10 - 12 μm region. It introduces an acceptable small temperature error of about 1-2°C for surfaces in the emissivity range 0.95 - 1. Examples are vegetated or partially vegetated fields ($\epsilon = 0.96 - 0.99$), agricultural soil ($\epsilon = 0.95 - 0.97$), water ($\epsilon = 0.98$), and asphalt / concrete ($\epsilon = 0.95 - 0.96$). Emissivities of various surfaces are documented in the literature [13, 144, 133, 109].

The atmospheric longwave radiation R_{atm} emitted from the atmosphere toward the ground can be written as

$$R_{atm} = \epsilon_a \; \sigma \; T_a^4 \tag{14.15}$$

where ϵ_a is the air emissivity, and T_a is the air temperature at screen height (2 m above ground), sometimes 50 m above ground are recommended. For cloud-free conditions, Brutsaert's equation [12] can be used to predict the effective air emissivity :

$$\epsilon_a = 1.24 \{\frac{p_{wv}}{T_a}\}^{1/7} \tag{14.16}$$

Here, p_{wv} is the water vapor partial pressure (millibars = hPa), and T_a is the air temperature (K). Figure 14.1 shows p_{wv} as a function of air temperature for relative humidities of 20 - 100%. The partial pressure is computed as :

$$p_{wv} = RH\ e_s\ /\ 100 \tag{14.17}$$

where RH is the relative humidity in per cent, and e_s is the water vapor partial pressure in saturated air (Murray 1967) :

$$e_s(T_a) = e_{s0}\ exp\{\frac{a(T_a - 273.16)}{T_a - b}\} \tag{14.18}$$

The constants are $a = 17.26939$, $b = 35.86$, and $e_{s0} = e_s(273.16K) = 6.1078\ hPa$. An alternative to equation (14.16) is the following approximation (Idso and Jackson 1969 [51]) which does not explicitly include the water vapor and holds for average humidity conditions, compare Figure 14.2.

$$\epsilon_a = 1 - 0.261\ exp\{-7.77 \times 10^{-4}\ (273 - T_a)^2\} \tag{14.19}$$

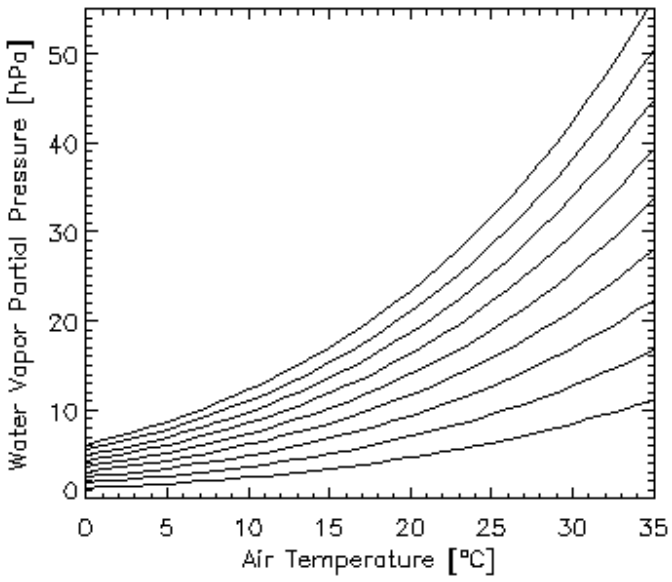

Figure 14.1: *Water vapor partial pressure as a function of air temperature and humidity. Relative humidities are 20% to 100% with a 10% increment, bottom to top curves, respectively (eq. 14.17).*

The calculation of the heat fluxes G, H, and LE on the right hand side of equation 14.10 requires different models for vegetated and man-made surfaces. For vegetated or partially vegetated surfaces, we employ a simple parametrization with the SAVI and scaled NDVI indices ([17, 15] :

$$G = 0.4\ R_n\ (SAVI_m - SAVI)/SAVI_m \tag{14.20}$$

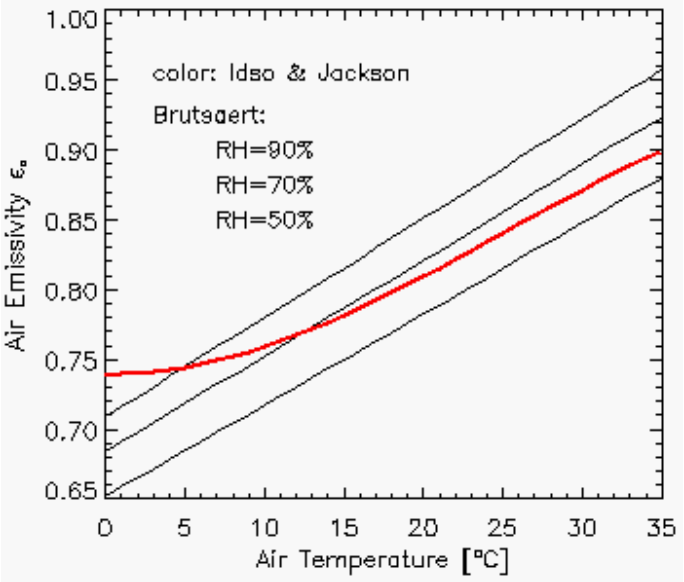

Figure 14.2: *Air emissivity after Brutsaert (eq. 14.16) and Idso/Jackson (eq. 14.19).*

where $SAVI_m = 0.814$ represents full vegetation cover. The sensible heat flux is computed as :

$$H = B\ (T_s - T_a)^n \tag{14.21}$$

$$B = 286\ (0.0109 + 0.051\ NDVI^*) \tag{14.22}$$

$$n = 1.067 - 0.372\ NDVI^* \tag{14.23}$$

$$NDVI^* = \frac{\rho_{850} - \rho_{650}}{0.75 * (\rho_{850} - \rho_{650})} \tag{14.24}$$

Equation (14.21) corresponds to equation (1a) of Carlson et al. (1995) [15], because G is neglected there, and so $R_n - G$ represents the energy left for evapotranspiration. The factor 286 in equation (14.22) converts the unit (cm/day) into (Wm^{-2}). $NDVI^*$ is the scaled NDVI ranging between 0 and 1, and truncated at 1 if necessary. Equation (14.24) corresponds to equation (3) of Carlson et al. (1995) with $NDVI_0 = 0$ (bare soil) and $NDVI_s = 0.75$ (full vegetation cover). The latent heat flux LE is computed as the residual:

$$LE = R_n\ -\ G\ -\ H \tag{14.25}$$

A different heat flux model is employed for urban areas with man-made surfaces (asphalt, concrete, roofs, etc.). These are defined here with the reflectance criteria

$$\rho_{650} \geq 0.10 \quad and \quad \rho_{850} \geq 0.10 \quad and \quad \rho_{650} > \rho_{850} * 0.7 \tag{14.26}$$

representing low vegetation indices with $NDVI < 0.176$. This simple spectral definition is not unambiguous, it might also apply to soils. For urban areas the latent heat is usually very small, and the fluxes G and H dominate. Therefore, the terms G, LE, and H are approximated by the following three equations (Parlow 1998):

$$G = 0.4\ R_n \tag{14.27}$$

$$LE = 0.15\ (R_n - G) \tag{14.28}$$

$$H = R_n\ -\ G -\ LE \tag{14.29}$$

For low vegetation indices ($SAVI < 0.1$) the ground heat flux G from equation (14.20), i.e., the vegetation model, agrees well with G from equation (14.27), i.e., the urban model. However, major differences exist for the LE and H terms, see table 14.1. Parameters for this table are: $E_g = 800$, $R_n = 600$, $R_{atm} + R_{surface} = -100\ Wm^{-2}$, $T_s = 30°C$, and $T_a = 20°C$. The (veg) and (urb) indicate the heat fluxes derived from the vegetation and urban model, respectively. For the urban surfaces (asphalt, concrete) the G(veg), H(veg) and LE(veg) values are given in brackets for comparison, but the corresponding "urban" heat fluxes are valid because the "urban" criterion (equations 14.26, $\rho_{650} \geq 0.10$, $\rho_{850} \geq 0.10$, and $\rho_{650} > \rho_{850} * 0.7$) applies. The last row repeats the concrete case for $R_{solar} = 800 * (1 - 0.36) = 512, R_n = R_{solar} + R_{atm} + R_{surface} = 512 - 100 = 412\ Wm^{-2}$, a realistic reduced R_n value (compared to the asphalt where $E_g = 800, R_{solar} = 800 * (1 - 0.12) = 700, R_n = 700 - 100 = 600\ Wm^{-2}$).

surface	ρ_{650}	ρ_{850}	NDVI	G(veg)	H(veg)	LE(veg)	G(urb)	H(urb)	LE(urb)
full veget.	0.05	0.40	0.78	77	87	435	-	-	-
partial veget.	0.10	0.20	0.33	185	76	338	-	-	-
dark asphalt	0.11	0.13	0.09	(228)	(50)	(322)	240	306	54
bright concrete	0.35	0.40	0.07	(222)	(48)	(330)	240	306	54
bright concrete (*)	0.35	0.40	0.07	-	-	-	164	210	37

Table 14.1: *Heat fluxes for the vegetation and urban model. All fluxes in [Wm^{-2}].*

All radiation and heat fluxes are calculated in units of Wm^{-2}. They represent instantaneous flux values. For applications, where daily (24 h) LE values are required the following equation can be used for unit conversion:

$$LE\ [\frac{cm}{day}] = \frac{1}{286}\ LE\ [Wm^{-2}] \tag{14.30}$$

The latent heat flux LE is frequently called evapotranspiration (ET). Although LE and ET are used interchangeably the unit (cm/day) or (mm/day) is mostly employed for ET. For water surfaces the distribution of net radiation into G, LE, and H is difficult to determine, because it depends on several other parameters. Therefore, G and H are set to zero here, and so LE equals R_n.

Spatial maps (files) of air temperature and air emissivity can also be included in the processing. Usually, isolated point-like measurements of air temperature are available from meteorological stations. These have to be interpolated to generate a spatial map coregistered to the image prior to applying the ATCOR model. Data in the file containing the air temperature must have the Celsius unit, data of the air emissivity file must range between 0 and 1. Future improvements to the ATCOR model will include an air temperature map derived from the image ("triangle" or "trapezoidal" method employing the thermal band surface temperature and NDVI, [15, 79]

In case of mountainous terrain, the air temperature $T_a(z_0)$ and water vapor partial pressure $p_{wv}(z_0)$ at a reference elevation z_0 have to be specified. The height dependence of air temperature is then obtained with linear extrapolation employing a user-specified adiabatic temperature gradient $\partial T/\partial z$:

$$T_a(z) = T_a(z_0)\ +\ \frac{\partial T}{\partial z}(z_0 - z) \tag{14.31}$$

where $\partial T/\partial z$ is typically in the range 0.65 - 0.9 (Celsius / 100 m). The water vapor partial pressure is extrapolated exponentially according to

$$p_{wv}(z) = p_{wv}(z_0)\ 10^{-(z-z_0)/z_s} \tag{14.32}$$

where z_s is the water vapor scale height (default 6.3 km). The list of all output channels of the value added *"*_flx.bsq"* file of ATCOR is :

1. Soil adjusted vegetation index (SAVI), scaled with factor 1000,
2. Leaf area index (LAI), scaled with 1000,
3. Fraction of photosynthetically active radiation FPAR, scaled with 1000,
4. Surface albedo (integrated reflectance from 0.3-2.5 μm), per cent * 10,
5. Absorbed solar radiation flux R_{solar} $[Wm^{-2}]$,
6. Global radiation E_g $[Wm^{-2}]$, omitted for constant visibility in flat terrain because it is a scalar which is put into the *"*log"* file .
   The next channels are only available in case of at least one thermal band:
7. Thermal air-surface flux difference $R_{therm} = R_{atm} - R_{surface}$ $[Wm^{-2}]$,
8. Ground heat flux G $[Wm^{-2}]$,
9. Sensible heat flux H $[Wm^{-2}]$,
10. Latent heat LE $[Wm^{-2}]$,
11. Net radiation R_n $[Wm^{-2}]$.

Bibliography

[1] Ackerman, S. A., Strabala, K. I., Menzel, W. P., Frey, R. A., Moeller, C. C., and Gumley, L. E., "Discriminating clear sky from clouds with MODIS", *J. Geophys. Res.*, Vol. 103, D24, 32,141-32,157 (1998).

[2] Adler-Golden, S.M., Matthew, M. W., Anderson, G. P., Felde, G. W., and Gardner, J. A., 2002, An algorithm for de-shadowing spectral imagery, *Proc. 11th JPL Airborne Earth Science Workshop, 5-8 March 2002*, JPL-Publication 03-04, Pasadena, U.S.A.

[3] Asner, G., "Canopy shadow in IKONOS satellite observations of tropical forests and savannas" *Remote Sensing of Environment*, Vol. 87, 521-533 (2003).

[4] Asrar, G., Fuchs, M., Kanemasu, E. T., and Hatfield, J. L., "Estimating absorbed photosynthetically active radiation and leaf area index from spectral reflectance in wheat", Agron. J., Vol. 76, 300-306, (1984).

[5] Asrar, G. "Theory and Applications of Optical Remote Sensing", J. Wiley, New York, (1989).

[6] Baret, F., and Guyot, G., 1991, "Potentials and limits of vegetation indices for LAI and APAR assessment", Remote Sensing of Environment, Vol. 35, 161-173, (1991).

[7] Berk, A., Bernstein, L.S., Anderson, G.P., Acharya, P.K., Robertson, D.C., Chetwynd, J.H., and Adler-Golden, S.M., "MODTRAN cloud and multiple scattering upgrades with application to AVIRIS", *Remote Sensing of Environment*, Vol. 65, 367-375 (1998).

[8] Berk, A., Anderson, G.P., Acharya, P.K., and Shettle, E.P., "MODTRAN5.2.0.0 User's Manual", Spectral Sciences Inc., Burlington MA, Air Force Research Laboratory, Hanscom MA (2008).

[9] Berk, A., Anderson, G.P., Acharya, P.K., "MODTRAN5.3.2 User's Manual", Spectral Sciences Inc., Burlington MA, Air Force Research Laboratory, Hanscom MA (2013).

[10] Berk, A., Hawes, F., v.d.Bosch, J., and Anderson, G.P., "MODTRAN5.4.0 User's Manual", Spectral Sciences Inc., Burlington MA, Air Force Research Laboratory, Hanscom MA (2016).

[11] F.-M. Breon, F. M. and Vermote, E., "Correction of MODIS surface reflectance time series for BRDF effects", *Remote Sens. Environ.*, Vol. 125, 1-9 (2012).

[12] Brutsaert, W., "On a derivable formula for long-wave radiation from clear skies", Water Resources Research, Vol. 11, 742-744, (1975).

[13] Buettner, K. J. K., and Kern, C. D., "The determination of infrared emissivities of terrestrial surfaces, Journal of Geophysical Research, Vol. 70, 1329-1337, (1965).

[14] Borel, C., "Error analysis for a temperature and emissivity retrieval algorithm for hyperspectral imaging data" *Int. J Remote Sensing*, Vol. 29, 5029-5045 (2008).

[15] Carlson, T. N., Capehart, W. J., and Gillies, R. R., "A new look at the simplified method for remote sensing of daily evapotranspiration", Remote Sensing of Environment, Vol. 54, 161-167, (1995).

[16] Chander, G., Markham, B. L., and Helder, D. L., "Summary of current radiometric calibration coefficients for Landsat MSS, TM, ETM+, and EO-1 ALI sensors", *Remote Sens. Environm.*, Vol. 113, 893-903 (2009).

[17] Choudhury, B. J., "Synergism of multispectral satellite observation for estimating regional land surface evaporation", Remote Sensing of Environment, Vol. 49, 264-274, (1994).

[18] Choudhury, B. J., Ahmed, N. U., Idso, S. B., Reginato, R. J., and Daughtry, C. S. T., "Relations between evaporation coefficients and vegetation indices studied by model simulations", Remote Sensing of Environment, Vol. 50, 1-17, (1994).

[19] Coll, C., Caselles, V., Rubio, E., Sospreda, F., and Valor, E., "Temperature and emissivity separation from calibrated data of the Digital Airborne Imaging Spectrometer", Remote Sens. Environm., Vol. 76, 250-259, (2001).

[20] Coll, C., Richter, R., Sobrino, J. A., Nerry, F., Caselles, V., Jimenez, J. C., Labed-Nachbrand, J., Rubio, E., Soria, G., and Valor, E., "A comparison of methods for surface temperature and emissivity estimation", In *Digital Airborne Spectrometer Experiment*, ESA- SP-499 p. 217-223, Nordwijk, Netherlands (2001).

[21] Comanicio, D., and Meer, P., "Mean shift: a robust approach toward feature space analysis", *IEEE Trans. Pattern Anal. Mach. Intell.*, Vol. 24, 603-619 (2002).

[22] C. Conese, C., Gilabert, A., Maselli, P., and Bottai, L., "Topographic normalization of TM scenes through the use pf an atmospheric correction method and ditital terrain models", *Photogr. Engin. Remote Sens.*, Vol. 59, 1745-1753 (1993).

[23] Corripio, J. G., "Vectorial algebra algorithms for calculating terrain parameters from DEMs and the position of the sun for solar radiation modelling in mountainous terrain", *Int. J. Geographical Information Science*, Vol. 17, 1-23 (2003).

[24] Crist, E. P., and Cicone, R. C., "A physically-based transformation of Thematic Mapper data - the Tasseled Cap", *IEEE Trans. Geosci. Remote Sensing*, Vol. GE-22, 256-263 (1984).

[25] Dash, P., Göttsche, F.-M., Olesen, F.-S., and Fischer, H., "Land surface temperature and emissivity estimation form passive sensor data: theory and practice - current trends", *Int. J Remote Sensing*, Vol. 23, 2563-2594 (2002).

[26] Dozier,J, Bruno, J., and Downey, P., "A faster solution to the horizon problem", *Computers and Geosciences*, Vol. 7,.145-151 (1981).

[27] Dell'Endice, F., Nieke, J., Schläpfer, D., and Itten, K. I., "Scene-based method for spatial misregistration detection in hyperspectral imagery", *Applied Optics*, Vol. 46, 2803-2816 (2007).

[28] ERSDAC. "ASTER User's Guide, Part II, (Vers. 3.1)", (2001).

[29] Fontenla, J. M., Curdt, W and Haberreiter, M., Harder J., and Tian, H.,"Semiempirical Models of the Solar Atmosphere. III. Set of Non-LTE Models for Far-Ultraviolet/Extreme-Ultraviolet Irradiance Computation *The Astrophysical Journal*, 707:482-502 (2009).

[30] Fontenla, J. M., Harder, J., Livingston, W., Snow, M., and Woods, T., "High-resolution solar spectral irradiance from extreme ultraviolett to far infrared", J. Geophys. Res., Vol. 116, D20108, 31pp., (2011).

[31] Frantz, D., Haß, E., Uhl, A., Stoffels, J., and Hill, J., "Improvement of the Fmask algorithm for Sentinel-2 images: separating clouds from bright surfaces based on parallax effects", *Remote Sens. Environ.*, vol. 215, pp.471-481, (2018).

[32] Fraser, R. S., Bahethi, O.P., and Al-Abbas, A. H., "The effect of the atmosphere on classification of satellite observations to identify surface features", *Remote Sens. Environm.*, Vol. 6, 229-249 (1977).

[33] B.-C. Gao and A. F. H. Goetz, "Column atmospheric water vapor and vegetation liquid water retrievals from airborne imaging spectrometer data", *J. Geophys. Research* Vol. 95, D4, pp.3549-3564, (1990).

[34] Gao, B.-C., Kaufman, Y.J., Han, W., and Wiscombe, W.J., "Correction of thin cirrus path radiances in the 0.4 - 1.9 μm spectral region using the sensitive 1.375 μm cirrus detecting channel", *J. Geophys. Res.*, Vol. 103, D24, 32,169-32,176 (1998).

[35] Gao, B.-C., Yang, P., Han, W., Li, R.-R., and Wiscombe, W.J., "An algorithm using visible and 1.38 μm channels to retrieve cirrus cloud reflectances from aircraft and satellite data", *IEEE Trans. Geosci. Remote Sens.*, Vol. 40, 1659-1668 (2002).

[36] Gao, B.-C., Kaufman, Y. J., Tanre, D., and Li, R. R., "Distinguishing tropospheric aerosols from thin cirrus clouds for improved aerosol retrievals using the ratio of $1.38-\mu m$ and $1.24-\mu m$ channels", *Geophys. Res. Letters*, Vol. 29, No. 18, 1890, 36-1 to 36-4 (2002).

[37] Gao, B.-C., Meyer, K., and Yang, P., "A new concept on remote sensing of cirrus optical depth and effective ice particle size using strong water vapor absorption channels near 1.38 and 1.88 μm", *IEEE Trans. Geosci. Remote Sens.*, Vol. 42, 1891-1899 (2004).

[38] Gillespie, A. R., "Lithologic mapping of silicate rocks using TIMS", *In Proc. TIMS Data User's Workshop*, JPL Publ. 83-38 (Pasadena, CA), pp. 29-44 (1986).

[39] Gillespie, A., et al., "A temperature and emissivity separation algorithm for Advanced Spaceborne Thermal Emission and Reflection Radiometer (ASTER) images", *IEEE Trans. Geosc. Remote Sensing*, Vol. 36, 1113-1126 (1998).

[40] Gu, D., and Gillespie, A., "Topographic normalization of Landsat TM images of forest based on subpixel sun - canopy - sensor geometry", *Remote Sensing of Environment*, Vol. 64, 166-175 (1998).

[41] Gu, D., Gillesspie, A. R., Kahle, A. B., and Palluconi, F. D., "Autonomous atmospheric compensation (AAC) of high resolution hyperspectral thermal infrared remote-sensing imgery", *IEEE TGRS.*, Vol. 38, 2557-2570 (2000).

[42] Guanter, L., Richter, R., and Moreno, J., "Spectral calibration of hyperspectral imagery using atmospheric absorption features", *Applied Optics*, Vol. 45, 2360-2370 (2006).

[43] Guanter, L., Richter, R., Kaufmann, H., "On the application of the MODTRAN4 atmospheric radiative transfer code to optical remote sensing", *Int. J. Remote Sensing*, Vol. 30, 1407-1424 (2009).

[44] Hagolle, O.; Huc, M.; Pascual, D.; Dedieu, G. "A multi-temporal and multi-spectral method to estimate aerosol optical thickness over land, for the atmospheric correction of FormoSat-2, LandSat, VENS and Sentinel-2 images". *Remote Sensing*, 7, 2668-2691 (2015).

[45] Hay, J. E., and McKay, D. C., "Estimating solar irradiance on inclined surfaces: a review and assessment of methodologies", *Int. J. Solar Energy*, Vol. 3, 203-240 (1985).

[46] Holben, B. N. and Justice, C. O., "The topographic effect on spectral response from nadir-pointing sensors", *Photogr. Engin. Remote Sens.*, Vol. 46, 1191-1200 (1980).

[47] Holben, B.; Eck, T.; Slutsker, I.; Tanre, D.; Buis, J.; Setzer, A.; Vermote, E.; Reagan, J.; Kaufman, Y.; Nakajima, T., "AERONET - A federated instrument network and data archive for aerosol characterization." *Remote Sens. Environ.* 66, 1-16 (1998).

[48] Hu B., Lucht W., Li X., and Strahler A.H., "Validation of kernel-driven semiempirical models for the surface bidirectional reflectance distribution function of land surfaces," *Remote Sens. Environ.*, vol. 62, no. 3, pp. 201-214, 1997.

[49] Huete, A. R., "A soil adjusted vegetation index (SAVI)", Remote Sensing of Environment, Vol. 25, 295-309, (1988).

[50] Hueni, A., Schläpfer, D., Jehle, M., and Schaepman, M., "Impacts of dichroic prism coatings on radiometry of the airborne imaging spectrometer APEX", Applied Optics, Vol. 53, 5344-5352 (2014).

[51] Idso, S. B., and Jackson, R. D., "Thermal radiation from the atmosphere", J. Geophysical Research, Vol. 74, 5397-5403, (1969).

[52] Irish, R., Barker, J. L., Goward, S. N., and Arvidson, T., "Characterization of the Landsat-7 ETM + Automated Cloud-Cover Assessment (ACCA) algorithm", *Photogrammetric Engineering and Remote Sensing,*, Vol. 72, 1179–1188 (2006).

[53] Isaacs, R. G., Wang, W-C., Worsham, R. D., and Goldberg, S., "Multiple scattering LOWTRAN and FASCODE models", *Applied Optics*, Vol. 26, 1272-1281, (1987).

[54] Yi, C. Y., "Haze reduction from the visible bands of Landsat TM and ETM+ images over a shallow water reef environment", *Remote Sens. Environm.*, Vol. 112, 1773-1783 (2008).

[55] Jimenez-Munoz, J. C., and Sobrino, J. A., "Atmospheric water vapour content retrieval from visible and thermal data in the framework of the DAISEX campaign", *Int. J. Remote Sensing*, Vol. 26, 3163-3180 (2005).

[56] Justice, C. O., Wharton, S. W., and Holben, B. N., "Application of digital terrain data to quantify and reduce the topographic effect on Landsat data", *Int. J. Remote Sens.*, Vol. 2, 213-230 (1981).

[57] Kahle, A. B., et al., "Middle infrared multispectral aircraft scanner data analysis for geological applications", *Applied Optics*, Vol. 19, 2279-2290 (1980).

[58] Kamstrup, N., and Hansen, L. B., "Improved calibration of Landsat-5 TM applicable for high-latitude and dark areas", *Int. J. Remote Sensing*, Vol. 24, 5345-5365 (2003).

[59] Kaufman, Y. J., "The atmospheric effect on the separability of field classes measured from satellites", *Remote Sens. Environ.*, Vol. 18, 21-34 (1985).

[60] Kaufman, Y. J., and Sendra, C., "Algorithm for automatic atmospheric corrections to visible and near-IR satellite imagery", *Int. J. Remote Sensing*, Vol. 9, 1357-1381 (1988).

[61] Kaufman, Y. J., et al. "The MODIS 2.1 μm channel - correlation with visible reflectance for use in remote sensing of aerosol", *IEEE Transactions on Geoscience and Remote Sensing*, Vol. 35, 1286-1298 (1997).

[62] Kleespies, T. J., and McMillin, L. M., "Retrieval of precipitable water from observations in the split window over varying surface temperature", *J. Applied Meteorology*, Vol. 29, 851-862 (1990).

[63] Kobayashi, S., and Sanga-Ngoie, K., "The integrated radiometric correction of optical remote sensing imageries" *Int. J. Remote Sensing*, Vol. 29, 5957-5985 (2008).

[64] Kobayashi, S., and Sanga-Ngoie, K., "A comparative study of radiometric correction methods for optical remote sensing imagery: the IRC vs. other image-based C-correction methods", *Int. J. Remote Sensing*, Vol. 30, 285-314 (2009).

[65] Krause, K., "Radiance conversion of QuickBird data", Technical note RS_TN_radiometric_radiance_4002, http://www.digitalglobe.com, Digital Globe, 1900 Pike Road, Longmont, CO 80501, USA (2003).

[66] Kriebel, K. T., "Measured spectral bidirectional reflection properties of four vegetated surfaces", *Applied Optics*, Vol. 17, 253-259 (1978).

[67] Levy, R.C. et al., "Algorithm for remote sensing of tropospheric aerosol over dark targets from MODIS: collections 005 and 051, Revision 2; Feb 2009" (2009).

[68] Li. Z. L., et al., "A new appooach for retrieving precipitable water from ATSR2 split-window channel data over land area", *Int. J. Remote Sensing*, Vol. 24, 3163-3180 (2003).

[69] Luo. Y., "Surface bidirectional reflectance and albedo properties derived using a land cover-based approach with Moderate Resolution Imaging Spectroradiometer observations", *J. Geophys. Res.*, vol. 110, no. 1, p. D01106, (2005).

[70] Liang, S., Falla-Adl, H., Kalluri, S., Jaja, J., Kaufman, Y. J., and Townshend, J. R. G., "An operational atmospheric correction algorithm for Landsat Thematic Mapper imagery over the land", *J. Geophys. Res.*, Vol. 102, D14, 17,173-17,186 (1997).

[71] Maignan F., Breon F. M. , and Lacaze R. , "Bidirectional reflectance of Earth targets: evaluation of analytical models using a large set of spaceborne measurements with emphasis on the Hot Spot", *Remote Sens. Environ.*, Vol. 90, No. 2, 210-220 (2004).

[72] Makarau, A., Richter, R., Müller, R., and Reinartz, P., "Haze detection and removal in remotely sensed multispectral imagery", *IEEE TGRS*, Vol. 52, 5895-5905 (2014).

[73] Makarau, A., Richter, R., Schläpfer, D, and Reinartz, P., "Combined haze and cirrus removal for multispectral imagery", *IEEE GRSL*, Vol. 13, 379-383 (2016).

[74] A. Makarau, R. Richter, D. Schläpfer, and P. Reinartz, "APDA Water Vapor Retrieval Validation for Sentinel-2 Imagery," vol. 14, no. 2, pp. 227–231, (2017).

[75] Schläpfer, D., Richter, R., and Reinartz, P., "Elevation-dependent removal of cirrus clouds in satellite imagery", *Remote Sensing*, 2020, 12, 494, doi:10.3390/rs12030494 .

[76] McMillin, L. M., "Estimation of sea surface temperature from two infrared window measurements with different absorption", *J. Geophys. Res.* Vol. 80, 5113-5117 (1975).

[77] Minnaert, M., "The reciprocity principle in lunar photometry", *Astrophys. J.*, Vol. 93, 403-410 (1941).

[78] Mouroulis, P., Green, R. O., and Chrien, T. G., "Design of pushbroom imaging spectrometers for optimum recovery of spectroscopic and spatial information", *Applied Optics*, Vol. 39, 2210-2220 (2000).

[79] Moran, M. S., Clarke, T. R., Inoue, Y., and Vidal, A., "Estimating crop water deficit using the relation between surface-air temperature and spectral vegetation index", Remote Sensing of Environment, Vol. 49, 246-263 (1994).

[80] Murray, F. W., "On the computation of saturation vapor pressure", J. Applied Meteorology, Vol. 6, 203-204, (1967).

[81] Nicodemus, F. E., "Reflectance nomenclature and directional reflectance and emissivity", *Applied Optics*, Vol. 9, 1474-1475 (1970).

[82] Nicodemus, F. E., Richmond, J. C., Hsia, J. J., Ginsberg, I. W., and Limperis, T., "Geometrical considerations and nomenclature for reflectance", Washington, DC, USA, U.S. Department of Commerce, National Bureau of Standards, (1977).

[83] Parlow, E., "Net radiation of urban areas", Proc. 17th EARSeL Symposium on Future Trends in Remote Sensing, Lyngby, Denmark, 17-19 June 1997, pp. 221-226, Balkema, Rotterdam (1998).

[84] Proy, C., Tanre, D., and Deschamps, P. Y., "Evaluation of topographic effects in remotely sensed data", *Remote Sens. Environ.*, Vol. 30, 21-32 (1989).

[85] Realmuto, V. J., "Separating the effects of temperature and emissivity: emissivity spectrum normalization", in Proc. 2nd TIMS Workshop. Pasadena, CA: Jet Propl. Lab. JPL Publication 90-55 (1990).

[86] Riano, D., Chuvieco, E., Salas, J., and Aguado, I., "Assessment of different topographic corrections in Landsat-TM data for mapping vegetation types", *IEEE Trans. Geoscience and Remote Sensing*, Vol. 41, 1056-1061 (2003).

[87] R. Richter, "A fast Atmospheric Correction algorithm applied to Landsat TM images," Int. J. of Remote Sensing, vol. 11, pp. pp. 159–166, (1990).

[88] Richter, R., "Derivation of temperature and emittance from airborne multispectral thermal infrared scanner data", *Infrared Phys. Technol.*, Vol. 35, 817-826 (1994).

[89] Richter, R., "A spatially adaptive fast atmospheric correction algorithm", *Int. J. Remote Sensing*, Vol. 17, 1201-1214 (1996).

[90] Richter, R., "Atmospheric correction of satellite data with haze removal including a haze/clear transition region", *Computers & Geosciences*, Vol. 22, 675-681 (1996).

[91] Richter, R., "On the in-flight absolute calibration of high spatial resolution spaceborne sensors using small ground targets", *Int. J. Remote Sensing*, Vol. 18, 2827-2833 (1997).

[92] Richter, R., "Correction of satellite imagery over mountainous terrain", *Applied Optics*, Vol. 37, 4004-4015 (1998).

[93] Richter, R., "Bandpass-resampling effects on the retrieval of radiance and surface reflectance", *Applied Optics*, Vol. 39, 5001-5005 (2000).

[94] Richter, R., and Coll, C., "Bandpass-resampling effects for the retrieval of surface emissivity", *Applied Optics*, Vol. 41, 3523-3529 (2002).

[95] Richter, R., and Schläpfer, D., "Geo-atmospheric processing of airborne imaging spectrometry data. Part 2: atmospheric / topographic correction.", *Int. J. Remote Sensing*, Vol. 23, 2631-2649 (2002).

[96] Richter, R., and Müller, A., "De-shadowing of satellite/airborne imagery", *Int. J. Remote Sensing*, Vol. 26, 3137-3148 (2005).

[97] Richter, R., Schläpfer, D., and Müller, A., "An automatic atmospheric correction algorithm for visible/NIR imagery", *Int. J. Remote Sensing*, Vol. 27, 2077-2085 (2005).

[98] Richter, R., Bachmann, M., Dorigo, W., Mueller, A., "Influence of the adjacency effect on ground reflectance measurements", *IEEE Geoscience Remote Sensing Letters*, Vol. 3, 565-569 (2006).

[99] Richter, R., and Schläpfer, D., "Considerations on water vapor and surface reflectance retrievals for a spaceborne imaging spectrometer", *IEEE Trans. Geoscience Remote Sensing*, Vol. 46, 1958-1966 (2008).

[100] Richter, R., Kellenberger, T., and Kaufmann, H., "Comparison of topographic correction methods", *Remote Sensing*, Vol. 1, 184-196 (2009).

[101] Richter, R., Schläpfer, D., and Müller, A., "Operational atmospheric correction for imaging spectrometers accounting the smile effect", *IEEE Trans. Geoscience Remote Sensing*, Vol. 49, 1772-1780 (2011).

[102] Richter, R., Wang, X., Bachmann, M., and Schläpfer, D., "Correction of cirrus effects in Sentinel-2 type of imagery", *Int. J. Remote Sensing*, Vol.32, 2931-2941 (2011).

[103] Richter, R., Heege, T., Kiselev, V., and Schläpfer, D., "Correction of ozone influence on TOA radiance", *Int. J. Remote Sensing*, Vol.35, 8044-8056 (2014).

[104] Richter, R., and D. Schläpfer, "Atmospheric / topographic correction for satellite imagery: ATCOR-2/3 User Guide", DLR IB 565-01/21, Wessling, Germany (2021).

[105] Richter, R., and D. Schläpfer, "Atmospheric / topographic correction for airborne imagery: ATCOR-4 User Guide", DLR IB 565-02/21, Wessling, Germany (2021).

[106] Richter, R., and D. Schläpfer, "Atmospheric and Topographic Correction (ATCOR Theoretical Background Document)", DLR IB 564-03/21, Wessling, Germany (2021).

[107] Rodger, A., and Lynch, M. J., "Determining atmospheric column water vapour in the 0.4-2.5 μm spectral region", Proceedings of the AVIRIS Workshop 2001, Pasadena, CA (2001).

[108] A. Rodger, "SODA: a new method of in-scene atmospheric water vapor estimation and post-flight spectral recalibration for hyperspectral sensors. Application to the HyMap sensor at two locations", *Remote Sens. Environ.*, vol. 115, pp.536-547, (2011).

[109] Salisbury, J. W., and D'Aria, D. M., "Emissivity of terrestrial materials in the 8-14 μm atmospheric window", *Remote Sensing of Environment*, Vol. 42, 83-106 (1992).

bibitemSandmeier1997 S. Sandmeier, S., and Itten, K. I., "A physically based model to correct atmospheric and illumination effects in optical satellite data of rugged terrain", *IEEE TGRS*, Vol. 34, 708-717 (1997).

[110] Sandmeier, S.T., and Deering, D. W. , "Structure analysis and classification of boreal forests using airborne hyperspectral BRDF data from ASAS", *Remote Sensing of Environment* vol. 69, no. 3, pp. 281-295, (1999).

[111] Santer, R., et al., "SPOT Calibration at the La Crau Test Site (France)", *Remote Sensing of Environment*, Vol. 41, 227-237 (1992).

[112] Santer, R., Ramon, D., Vidot, J., and Dilligeard, E., "A surface reflectance model for aerosol remote sensing over land", *Int. J. Remote Sensing*, Vol.28, 737-760 (2007).

[113] Schaaf, C. B., Li, X., and Strahler, A. H., "Topographic effects on bidirectional and hemispherical reflectances calculated with a geometric-optical canopy model", *IEEE TGRS*, Vol. 32, 1186-1192 (1994).

[114] Schaepman-Strub, G., Schaepman, M., Painter, T., Dangel, S., and Martonchik, J., "Reflectance quantities in optical remote sensing - definitions and case studies", *Remote Sensing of Environment*, Vol. 103, 27-42 (2006).

[115] Schläpfer, D., Borel, C. C., Keller, J., and Itten, K. I., "Atmospheric precorrected differential absorption technique to retrieve columnar water vapor", *Remote Sensing of Environment*, Vol. 65, 353-366 (1998).

[116] Schläpfer, D., and Richter, R., "Geo-atmospheric processing of airborne imaging spectrometry data. Part 1: parametric orthorectification.", *Int. J. Remote Sensing*, Vol. 23, 2609-2630 (2002).

[117] Schläpfer, D., and Richter, R., "Spectral polishing of high resolution imaging spectroscopy data", Earsel SIG-IS Workshop, Edinburgh (2011).

[118] Schläpfer, D. and R. Richter, "Evaluation of Brefcor BRDF Effects Correction for Hyspex, CASI, and APEX Imaging Spectroscopy Data",presented at IEEE Whispers, Lausanne, pp. 4, (2014).

[119] Schläpfer, D., Richter R., and Feingersh T., "Operational BRDF Effects Correction for Wide-Field-of-View Optical Scanners (BREFCOR)", *IEEE Trans. Geoscience and Remote Sensing*, vol. 53, no. 4, pp. 1855-1864, (2015).

[120] Schläpfer D. and R. Richter, "Atmospheric Correction of Imaging Spectroscopy Data Using Shadow-Based Quantification of Aerosol Scattering Effects", *EARSeL eProceedings*, vol. 16, no. 1, pp. 21-28, (2017).

[121] Schläpfer D., A. Hueni, and R. Richter, "Cast Shadow Detection to Quantify the Aerosol Optical Thickness for Atmospheric Correction of High Spatial Resolution Optical Imagery", *Remote Sensing*, vol. 10, 200, pp. 25; ; doi:10.3390/rs10020200, (2018).

[122] Schläpfer, D. "PARGE, User Guide, Version 3.4", ReSe Applications LLC, Wil, Switzerland, (2018), available at https://www.rese-apps.com, pp 301.

[123] Schläpfer D., R. Richter, and P. Reinartz, "Elevation-dependent removal of cirrus clouds in satellite imagery", *Remote Sensing*, vol. 12, 494, doi:10.3390/rs12030494 (2020).

[124] Schowengerdt, R. A., "Remote Sensing, Models and Methods for Image Processing", 3rd Edition, Elsevier (Academic Press), (2007).

[125] Shao, Y., Taff, G. N., and Walsh, S. J. , "Shadow detection and building-height estimation using IKONOS data", International Journal of Remote Sensing, 32(22), 6929-6944. doi:10.1080/01431161.2010.517226 (2011).

[126] Sirguey, P., "Simple correction of multiple reflection effects in rugged terrain", *Int. J. Remote Sensing*, Vol. 30, 1075-1081 (2009).

[127] Slater, P. N., "Remote Sensing, Optics and Optical Systems", Addison-Wesley, London (1980).

[128] Slater, P. N., "Radiometric considerations in remote sensing", *Proc. IEEE*, Vol. 73, 997-1011 (1985).

[129] Slater, P. N., et al., "Reflectance and radiance-based methods for the in-flight absolute calibration of multispectral sensors", *Remote Sensing of Environment*, Vol. 22, 11-37 (1987).

[130] Smith, J.A., Tzeu, L. L., Ranson, K. J., "The Lambertian assumption and Landsat data", *Photogr. Engin. Remote Sens.*, Vol. 46, 1183-1189 (1980).

[131] Sobrino, J. A., Jimenez-Munoz, J. C., Soria, G., Romaguera, M., Guanter, L., and Moreno, J., "Land surface emissivity retrieval from different VNIR and TIR sensors", *IEEE TGRS.*, Vol. 46, 316-327 (2008).

[132] Soenen, S., A., Peddle, D. R.,and Coburn, C. A., "SCS+C: a modified sun - canopy - sensor topographic correction in forested terrain", *IEEE Trans. Geoscience and Remote Sensing*, Vol. 43, 2148-2159 (2005).

[133] Sutherland, R. A., "Broadband and spectral emissivities (2-18 μm) of some natural soils and vegetation, *Journal of Atmospheric and Oceanic Technology*, Vol. 3, 199-202 (1986).

[134] Stamnes, K., Tsay, S. C., Wiscombe, W. J., and Jayaweera, K., "Numerically stable algorithm for discrete-ordinate-method radiative transfer in multiple scattering and emitting layered media", *Applied Optics*, Vol. 27, 2502-2509 (1988).

[135] Teillet, P. M., Guindon, B., and Goodenough, D.G., "On the slope-aspect correction of multispectral scanner data", *Canadian J. Remote Sensing*, Vol. 8, 84-106, (1982).

[136] D. R. Thompson, B.-C. Gao, R. O. Green, D. A. Roberts, P. E. Dennison, and S. R. Lundeen, "Atmospheric correction for global mapping spectroscopy: ATREM advances for the HyspIRI preparatory campaign", *Remote Sens. Environ.*, Vol, 167, pp.64-77 (2015)

[137] Thuillier, G., Herse, M., Labs, D., Foujols, T., Peetermans, W., Gillotay, D., Simon, P. C., and Mandel, H., "The solar spectral irrandiance from 200 to 2400 nm as measured by the SOLSPEC spectrometer from the ATLAS and EURECA missions", *Solar Physics*, Vol. 214, 1 - 22 (2003).

[138] Vincent, R., "Rock-type discrimination from ratioed infrared scanner images of Pisgah Crater, California", Science Vol. 175, 986-988 (1972).

[139] Vögtli, M., Schläpfer, D., Richter, R., Hueni, A., Schaepman, M., and Kneubühler, M., "About the transferability of topographic correction methods from spaceborne to airborne optical data", *IEEE JSTARS*, Vol. 14, 1348-1362 (2021).

[140] Wanner W., A. H. Strahler, B. Hu, P. Lewis, J.-P. Muller, X. Li, C. L. B. Schaaf, and M. J. Barnsle, "Global retrieval of bidirectional reflectance and albedo over land from EOS MODIS and MISR data: Theory and algorithm", J. Geophys. Res., vol. 102, no. 14, pp. 17143D17161, (1997).

[141] Wiegand, C. L., Gerbermann, A. H., Gallo, K. P., Blad, B. L., and Dusek, D., "Multisite analyses of spectral-biophysical data for corn", Remote Sensing of Environment, Vol. 33, 1-16, (1990).

[142] Wiegand, C. L., Richardson, A. J., Escobar, D. E., and Gerbermann, A. H., "Vegetation indices in crop assessments", Remote Sensing of Environment, Vol. 35, 105-119, (1991).

[143] WMO. WMO Guide to Meteorological Instruments and Methods of Observation. Technical report, WMO, Geneva, (2014).

[144] Wolfe, W. L., and Zissis, G. J., "The Infrared Handbook", Office of Naval Research, Washington, DC., (1985).

[145] Young, S. J., Johnson, B. R., and Hackwell, J. A., "An in-scene method for atmospheric compensation of thermal hyperspectral data", *J. Geophys. Research*, Vol. 107, No. D24, 4774-4793 (2002).

[146] Zhang, Y., Guindon, B., and Cihlar, J., "An image transform to characterize and compensate for spatial variations in thin cloud contamination of Landsat images", *Remote Sensing of Environment*, Vol. 82, 173-187 (2002).

[147] Zhu, Z., and Woodcock, C. E., "Object-based cloud and cloud shadow detection in Landsat imagery", *Remote Sensing of Environment*, Vol. 118, 83-94 (2012).

[148] Zhu, Z., Wang, S., and Woodcock, C. E., "Improvement and expansion of the Fmask algorithm: cloud, cloud shadow, and snow detection for Landsats 4-7, 8, and Sentinel-2 images" *Remote Sensing of Environment*, Vol. 159, 269-277 (2015).

Appendix A

Altitude Profile of Standard Atmospheres

This chapter contains the altitude profiles of ATCOR's standard atmospheres that are based on the MODTRAN code. Only the lower 5 km altitudes are shown, since this region has the largest influence on the radiative transfer results and usually comprises about 90-95% of the total water vapor column. For multispectral sensors without water vapor bands, e.g., Landsat TM or SPOT, the selection of the atmosphere should be coupled to the season of the image data acquisition. The influence of a large error in the water vapor estimate (e.g., 50%) on the reflectance retrieval is usually very small (about 1-2% reflectance at a reflectance level of 40% for Landsat TM band 4).

However, for sensors with water vapor bands (e.g., Sentinel-2, Venμs, or hyperspectral instruments) the water vapor content plays an important role. For these sensors the atmospheric database contains files with six water vapor columns (W = 0.4, 1.0, 2.0, 2.9, 4.0, 5.0 cm) for a ground at sea level. The water vapor values W decrease exponentially with elevation z (km) and a useful approximation is

$$W(z) = W(0)\ exp(-0.54\ z) \tag{A.1}$$

The six water vapor grid points are used to generate interpolated and extrapolated values for the LUTs. The corresponding file names for the rural aerosol (based on the sea level water vapor values) are *"h99000_wv04_rura.atm"*, to *"h99000_wv50_rura.atm"*. The 'h99000' indicates the symbolic height of 99000 m used for satellites, the sea level water vapor column (cm or g cm^{-2}) is scaled with with 10, and the aerosol type is included in the last part of the name.
For the airborne version of ATCOR there are corresponding files for a number of flight altitudes: 100 m, then 1000 m to 5000 m with increment 1000 m, 10,000 m, and 20,000 m. For flight levels in between, interpolation is applied.

altitude (km)	pressure (mbar)	temperature (°C)	rel. humidity (%)	abs. humidity (gm^{-3})
0	1013	26.4	7.5	1.9
1	904	20.4	7.3	1.3
2	805	14.4	7.4	0.9
3	715	10.4	4.8	0.5
4	633	3.8	3.5	0.2
5	559	-3.0	3.8	0.1

Table A.1: *Altitude profile of the dry atmosphere. Total (ground-to-space) water vapor content = 0.41 (cm or g cm^{-2}).*

altitude (km)	pressure (mbar)	temperature (°C)	rel. humidity (%)	abs. humidity (g/m^{-3})
0	1018	-1.0	77	3.5
1	897	-4.5	70	2.5
2	789	-8.0	65	1.8
3	694	-11.5	57	1.2
4	608	-17.5	50	0.7
5	531	-23.5	47	0.4

Table A.2: *Altitude profile of the midlatitude winter atmosphere. Total (ground-to-space) water vapor content = 0.85 (cm or g cm^{-2}).*

altitude (km)	pressure (mbar)	temperature (°C)	rel. humidity (%)	abs. humidity (g/m^{-3})
0	1013	10.0	56	5.2
1	902	3.0	47	2.8
2	802	-1.0	41	1.9
3	710	-5.0	40	1.4
4	628	- 9.0	40	1.0
5	554	-14.0	40	0.6

Table A.3: *Altitude profile of the fall (autumn) atmosphere. Total (ground-to-space) water vapor content = 1.14 (cm or g cm^{-2})*

altitude	pressure	temperature	rel. humidity	abs. humidity
(km	(mbar)	(°C)	(%)	(g/m^{-3})
0	1013	15.0	46	5.9
1	900	8 .5	49	4.2
2	795	2.0	52	2.9
3	701	-4.5	51	1.8
4	616	-11.0	50	1.1
5	540	-17.5	48	0.6

Table A.4: *Altitude profile of the 1976 US Standard. Total (ground-to-space) water vapor content = 1.42 (cm or g cm^{-2}).*

altitude	pressure	temperature	rel. humidity	abs. humidity
(km)	(mbar)	(°C)	(%)	(g/m^{-3})
0	1010	14.0	75	9.1
1	896	8.5	70	6.0
2	792	3.1	70	4.2
3	700	-2.3	65	2.7
4	616	-7.7	60	1.7
5	541	-13.1	53	1.0

Table A.5: *Altitude profile of the subarctic summer atmosphere. Total (ground-to-space) water vapor content = 2.08 (cm or g cm^{-2}).*

altitude	pressure	temperature	rel. humidity	abs. humidity
(km)	(mbar)	(°C)	(%)	(g/m^{-3})
0	1013	21.0	76	13.9
1	902	16.5	66	9.3
2	802	12.0	55	5.9
3	710	6.0	45	3.9
4	628	0.0	39	1.9
5	554	-6.0	31	1.0

Table A.6: *Altitude profile of the midlatitude summer atmosphere. Total (ground-to-space) water vapor content = 2.92 (cm or g cm^{-2}).*

altitude (km)	pressure (mbar)	temperature (°C)	rel. humidity (%)	abs. humidity (g/m^{-3})
0	1013	26.4	75	18.9
1	904	20.4	73	13.0
2	805	14.4	74	9.3
3	715	10.4	48	4.7
4	633	3.8	35	2.2
5	559	-3.0	38	1.5

Table A.7: *Altitude profile of the tropical atmosphere. Total (ground-to-space) water vapor content = 4.11 (cm or g cm^{-2}).*

Appendix B

Comparison of Solar Irradiance Spectra

The following two plots show the relative differences between two extraterrestrial solar irradiance sources:

- Kurucz 1997 (distributed with MODTRAN, Berk et al. 2016 [10]). The previous high-resolution (*"monochromatic"*) databases of ATCOR were calculated with this spectrum.
- Fontenla 2011 (Fontenla et al., 2009, 2011 [29, 30]). The current ATCOR release uses the improved quiet sun spectrum of Fontenla and co-workers, also referred to as "low activity sun".

As explained in the ATCOR-3 and ATCOR-4 user manuals the user can convert the database of atmospheric look-up tables from one solar irradiance source to another one, provided that the spectral range and sampling distance agrees with the template spectra in the *"sun_irradiance"* directory of ATCOR. Currently, irradiance spectra of Kurucz 1997, Kurucz 2005, and Fontenla 2011 (distributed with MODTRAN [10]), are included in the ATCOR distribution. In addition, the Thuillier 2003 irradiance spectrum [137] is also supplied.

The plots show the detailed information (line structure) contained in the Fontenla spectrum. The curves with 2.8 nm and 10 nm represent results based on a moving average of the the 0.4 nm data over 7 and 25 spectral points, respectively.

While the solar constant is known to an accuracy of about 1%, the spectral solar irradiance models show larger differences, increasing with decreasing bandwidth. Therefore, the sensor-specific folders in 'atm_lib' contain the resampled atmospheric LUTs ('*.atm'), and additionally a file '*irrad_source.txt*' documenting the name of the solar irradiance model employed for the convolution of the high-resolution atmospheric database with the channel response functions.

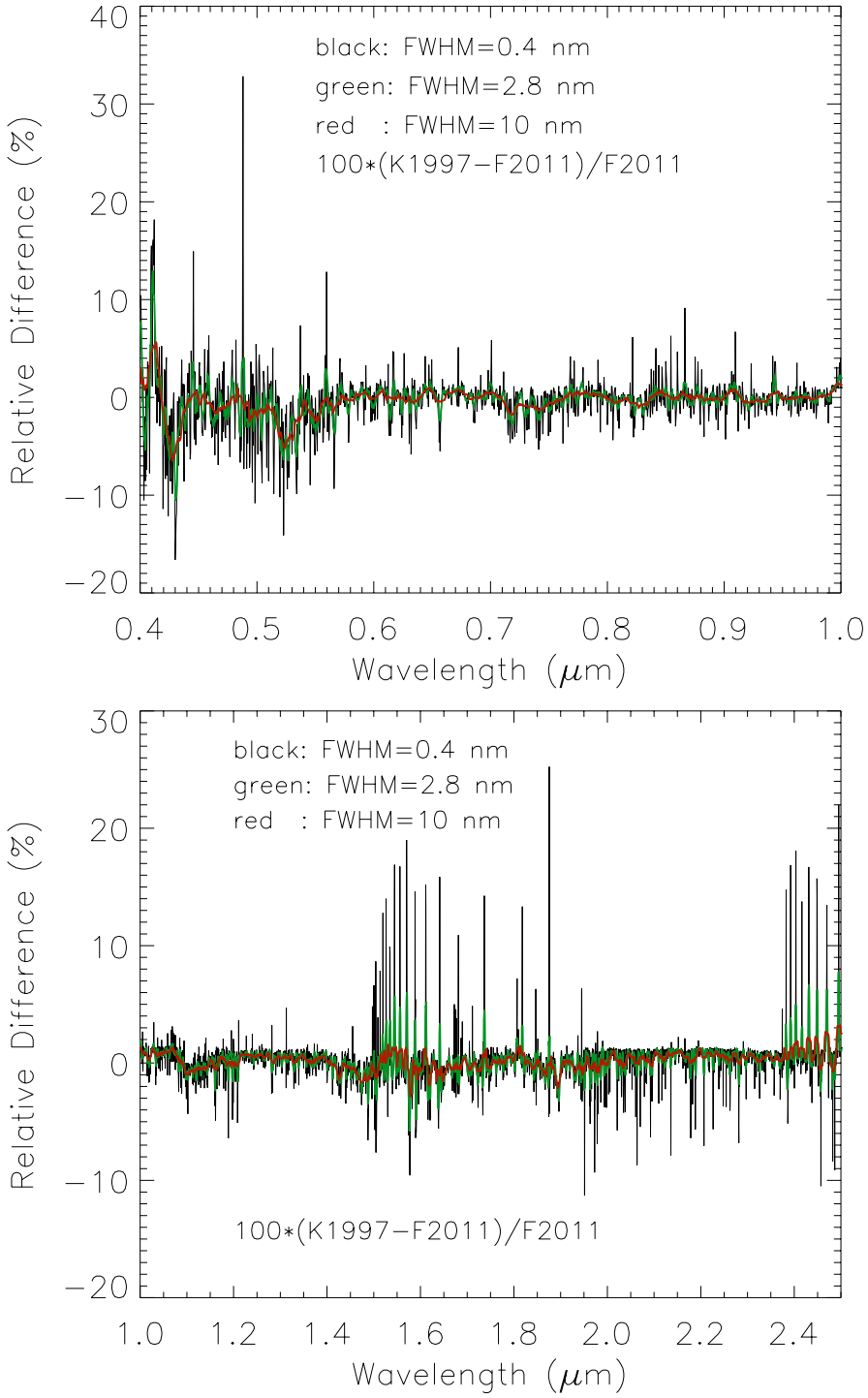
black: FWHM=0.4 nm
green: FWHM=2.8 nm
red : FWHM=10 nm
100*(K1997−F2011)/F2011
Relative Difference (%)
Wavelength (μm)
black: FWHM=0.4 nm
green: FWHM=2.8 nm
red : FWHM=10 nm
100*(K1997−F2011)/F2011
Relative Difference (%)
Wavelength (μm)

Appendix C

ATCOR Input/Output Files

The standard file format for the input image is the ENVI band-sequential format (*'bsq'*). If the input image is named *'scene.bsq'* the nomenclature for the output files is as described below, omitting the folder name.
In case of rugged terrain, the following nomenclature is preferred: Elevation file: *'xxx_ele.bsq'* (elevation in meters) , slope file *'xxx_slp.bsq'* (degrees), aspect file *'xxx_asp.bsq'*, optional skyview file: *'xxx_sky.bsq'*. The DEM file names have to be included in the input parameter file *'scene.inn'*, either using the ATCOR GUI or by editing this file.
For a number of sensors there is an import function, which reads the required data from the sensor-specific meta file and creates the input parameter file *'scene.inn'* and the radiometric calibration *'scene.cal'*. In addition, batch processing for frequently used sensors is supported, e.g.,

*'landsat8_batch,'/folder/LC08*_B1.TIF'*,

where the first band of the *'*.TIF'* files has to be specified.

C.1 Preclassification files

- *scene_out_hcw.bsq*: standard preclassification map (haze, cloud, cirrus, water, snow)
- *scene_haze_map.bsq*: classification map of module *'dehaze'*

C.2 Surface reflectance related files

- *scene_atm.bsq*: contains surface reflectance cube after atmospheric/topographic correction
- *scene_atm_ddv.bsq*: DDV map (and water)
- *scene_atm_aot.bsq*: AOT550nm (scale factor 1,000)
- *scene_atm_wv.bsq*: water vapor map (scale factor 1,000)
- *scene_ilu.bsq*: cosine (local solar zenith), scale factor 100, if rugged terrain
- *scene_atm.log*: contains input parameters and logging data

C.3 Temperature / emissivity related files

For multi-channel thermal data, the *'scene_atm.bsq'* contains the blackbody surface radiance, and surface temperature is appended as the last band. Additionally, there are different emissivity files, depending on the selected temperature /emissivity algorithm.

- *scene_at_sensor_tbb.bsq*: at-sensor BB temperature
- *scene_atm_emiss.bsq*: surface emissivity (NEM, ANEM algorithm)
- *scene_atm_tes_emiss.bsq*: surface emissivity (TES algorithm)
- *scene_atm_tes_temperature.bsq*: surface temperature (TES algorithm)
- *scene_atm_emiss_lp5.bsq*: surface emissivity with a 5-channel low pass filter (if more than 30 bands)
- *scene_atm_isac_emiss_lp5.bsq*: surface emissivity with ISAC algorithm
- *scene_atm_isac_surface_tbb.bsq*: ISAC at-surface BB temperature
- *emissivity.dat*: table of standard surface emissivities as given in ATCOR installation (see

class ID	class	default emissivity
0	not classified	emissivity = 0.990
1	clear water	emissivity = 0.991
2	dark vegetation	emissivity = 0.980
3	average vegetation	emissivity = 0.980
4	bright vegetation	emissivity = 0.980
5	yellow vegetation	emissivity = 0.980
6	mixed veget./soil	emissivity = 0.975
7	bare soil (dark)	emissivity = 0.970
8	bare soil	emissivity = 0.970
9	asphalt/man-made	emissivity = 0.955
10	sand / bare soil	emissivity = 0.970
11	bright sand / soil	emissivity = 0.970
12	dry vegetat./ soil	emissivity = 0.975
13	sparse veg. /soil	emissivity = 0.975
14	snow	emissivity = 0.980
15	cloud	emissivity = 0.980
16	turbid water	emissivity = 0.984
17	water over sand	emissivity = 0.984
18	shadow	emissivity = 0.984

Table C.1: *Standard emissivity classes as defined in ATCOR*